

**Advanced Techniques for the Estimation of Crack Shape and  
Detection of Crack Growth in Mechanical Tests**

**Thomas M Buss, BSc**

A thesis presented for the degree of  
Doctor of Philosophy



School of Mechanical, Materials and Manufacturing Engineering  
University of Nottingham  
May 8, 2022

## ABSTRACT

It is known that cracks grow in materials subject to both mechanical and thermomechanical fatigue. Work has been undertaken to investigate the shapes of cracks in two materials in low cycle fatigue (LCF) and thermomechanical fatigue (TMF) conditions utilising novel Alternating Current Potential Difference (ACPD) and beach marking methods to measure the crack length. This has been added to by the development of a novel beach marking technique which enables the user to define the position and size of marks.

Crack growth measurement work has been undertaken on two materials, 316 Stainless Steel (SS316) and Nickel Alloy RR1000 (RR1000), using a fixed frequency ACPD system. In this work a range of crack shapes and directions have been recorded but due to the fixed frequency of the Alternating Current Potential Difference (ACPD) system this could not be measured during the tests. In this both quarter-circular and non-uniform crack shapes have been present, depending on the loading and temperature exerted during the test.

An advanced ACPD technique has also been developed and tested using a range of specimen and feature geometry. In experiments where the cross-sectional area has remained the same the technique has been shown sensitive to the cross-sectional shape. The change in the response (impedance magnitude and phase) with frequency has been shown to systematically vary for the different cross-section shapes, suggesting the method is capable of discerning different cross sectional geometries. A range of crack like features have also been tested, in this the direct current (DC) response has been shown to vary as is expected due to the area of the feature. In addition to this as the frequency increases and hence the skin depth is reduced the response changes to reflect not just the feature area but the shape.

A novel fracture mechanics beach marking technique has also been devel-

oped, which enables the user to program the position and size of beach marks on a fracture surface without needing additional instrumentation. This technique has been shown to be able to produce beach marks down to  $25\mu\text{m}$ , the technique gives crack position predictions to about 2% of the experimental value.

## ACKNOWLEDGEMENTS

Many thanks to Rolls Royce for the support in supplying materials and funding to undertake this work.

Much gratitude to Jason Greaves for his work in the Wolfson Building testing and measurement facilities, enabling and helping with use of the facilities and equipment.

Thanks to Seamus Garvey, Christopher Hyde and James Rouse for their thoughts and guidance throughout.

Thanks to the Nano and Micro Scale Research Centre staff in supporting the Scanning Electron Microscope (SEM) imaging.

## CONTENTS

1. <i>Introduction</i> . . . . .	13
2. <i>Literature Review</i> . . . . .	16
2.1 Introduction . . . . .	16
2.2 Materials Behaviour . . . . .	19
2.2.1 Elasticity and Plasticity . . . . .	19
2.2.2 Creep . . . . .	21
2.2.3 Fatigue . . . . .	22
2.2.4 Dynamic Strain Ageing . . . . .	29
2.2.5 Mutli-mode Behaviour . . . . .	31
2.3 Electrical Properties . . . . .	33
2.3.1 Direct Current . . . . .	33
2.3.2 Alternating Current . . . . .	34
2.4 Materials . . . . .	35
2.4.1 High Temperature Steels . . . . .	35
2.4.2 High Temperature Nickel Alloys . . . . .	38
2.5 Crack Measurement . . . . .	40
2.5.1 Penetrants . . . . .	40
2.5.2 Surface Measurements . . . . .	41
2.5.3 Crack Opening Displacement . . . . .	41
2.5.4 Ultrasound . . . . .	43
2.5.5 Eddy Currents . . . . .	43
2.5.6 Beach Marking . . . . .	44
2.5.7 Electrical Potential Drop . . . . .	45
2.6 Summary . . . . .	50

---

3. Methodology . . . . .	51
3.1 Thermomechanical Fatigue Rig Development . . . . .	51
3.1.1 Temperature Control . . . . .	51
3.1.2 Notches and Pre-cracking . . . . .	56
3.1.3 Crack Growth Measurement . . . . .	60
3.1.4 Calculations of Crack Growth Rates . . . . .	63
3.2 Beach Marking . . . . .	69
3.2.1 Loading Trials . . . . .	70
3.2.2 Fracture Mechanics Approach . . . . .	70
3.3 Alternating Current Potential Drop Technique . . . . .	70
3.3.1 Bench Frequency Sweep Testing . . . . .	70
3.3.2 Advanced Alternating Current Potential Drop Kit De- velopment . . . . .	71
3.3.3 Troubleshooting . . . . .	85
3.4 Data Analysis . . . . .	87
3.5 Discussion . . . . .	88
4. Beach Marking . . . . .	91
4.1 Introduction . . . . .	91
4.2 Test Interruption Beach Mark Testing . . . . .	92
4.2.1 316 Stainless Steel . . . . .	92
4.2.2 RR1000 . . . . .	99
4.3 Fracture Mechanics Method . . . . .	101
4.4 Discussion . . . . .	117
4.4.1 Test Interruption Beach Mark Testing . . . . .	117
4.4.2 Fracture Mechanics Method . . . . .	125
5. Crack Growth Testing Results using Fixed Frequency Alternating Current Potential Drop . . . . .	127
5.1 Introduction . . . . .	127
5.2 Stainless Steel - 316 . . . . .	128
5.2.1 Test Conditions . . . . .	128
5.2.2 Results . . . . .	128

---

5.3	RR1000 . . . . .	131
5.3.1	Test Conditions . . . . .	131
5.3.2	Results . . . . .	132
5.4	Discussion . . . . .	136
5.4.1	Stainless Steel - 316 . . . . .	136
5.4.2	RR1000 . . . . .	138
6.	<i>Advanced Alternating Current Potential Drop Development</i> . . . .	139
6.1	Introduction . . . . .	139
6.2	Trials with Existing Equipment . . . . .	140
6.3	Advanced Alternating Current Potential Drop . . . . .	142
6.3.1	Bench Samples . . . . .	142
6.3.2	Resistivity Calculation . . . . .	150
6.4	Discussion . . . . .	152
6.4.1	Initial Trials . . . . .	152
6.4.2	Advanced Alternating Current Potential Drop . . . . .	153
7.	<i>Discussions</i> . . . . .	158
8.	<i>Conclusions</i> . . . . .	165
9.	<i>Further Work</i> . . . . .	167
	<i>Appendix</i> . . . . .	182
A.	<i>Appendix</i> . . . . .	183
A.1	CGM-7 Sweep Labview Code . . . . .	183
A.2	PXI Sweep Labview Code . . . . .	184
A.3	Bench Samples . . . . .	185
A.4	Crack Growth Rate Code . . . . .	187
A.5	Fracture Mechanics Beach Mark Code . . . . .	188

## LIST OF FIGURES

2.1	IP and OP TMF Waveforms . . . . .	18
2.2	Schematic Representation of typical Stress-Strain Curves from uni-axial tension tests . . . . .	19
2.3	Schematic Representation of typical Creep Curve . . . . .	22
2.4	Stress-Strain Loop . . . . .	26
2.5	Schematic Representation of Cyclic Softening and Hardening . . . . .	27
2.6	Schematic Representation of Ratcheting Behaviour [22] . . . . .	28
2.7	Schematic of Types of Serrations due to dynamic strain ageing (DSA) [27] . . . . .	30
2.8	Schematic of the Regime where Creep-Fatigue Interaction is Significant [32] . . . . .	32
2.9	CT Specimen with COD Gauge . . . . .	42
2.10	Direct and Alternating Current Flow . . . . .	46
2.11	Thin Skin Alternating Current Field Method (ACFM) [91] . . . . .	48
3.1	Standard TMF Specimen . . . . .	52
3.2	Crack Growth Rate TMF Specimen . . . . .	53
3.3	Thermocouple Positions . . . . .	54
3.4	Induction Coil and Thermal Calibration Specimen . . . . .	57
3.5	Typical Thermal Calibration Cycle . . . . .	58
3.6	External Cooling Arrangement . . . . .	59
3.7	Ambient Temperature Linearity Test . . . . .	63
3.8	Creep Hold Beach Marks . . . . .	64
3.9	Elevated Temperature Linearity Test 600°C . . . . .	65
3.10	Schematic Representation of a typical crack growth rate plot . . . . .	67
3.11	Schematic Representation of the cross section of corner crack . . . . .	67

---

3.12	Schematic Representation of Beach Marking . . . . .	69
3.13	TMF sample and clamping . . . . .	72
3.14	Skin Depth for various materials . . . . .	74
3.15	Fast Fourier Transform (FFT) of the signals from Fylde trials showing noise at 254kHz . . . . .	77
3.16	Schematic of Loop Sample . . . . .	79
3.17	Sample and Loop Signals . . . . .	80
3.18	Schematic of Flux Bridging . . . . .	81
3.19	Schematic of Flux Blocking . . . . .	81
3.20	Flux Bridge and Blocking test - Voltages measured on the loop wire . . . . .	82
3.21	Shielding Box . . . . .	82
3.22	Shielding Box test - Voltages measured on the loop wire . . .	83
3.23	Steel Current Supply Rods . . . . .	84
3.24	Non-sinusoidal Voltages . . . . .	85
3.25	Common Mode Distortion . . . . .	86
3.26	FFT and Manual Data Processing - Impedance - Circular Sample	88
3.27	FFT and Manual Data Processing - Phase - Circular Sample .	89
4.1	Hold Marked Surface - Back Scattered Electron . . . . .	93
4.2	Hold Mark Low Magnification - Back Scattered Electron . . .	93
4.3	Hold Mark Medium Magnification - Back Scattered Electron .	94
4.4	Hold Mark High Magnification - Back Scattered Electron . . .	94
4.5	Hold Step in Secondary and Backscattered Electron Modes . .	95
4.6	Eight Hold Marks - Optical Microscope Image . . . . .	96
4.7	Eight Hold Marks - Potential Drop Data . . . . .	96
4.8	2 Hour Holds at Mean Load - 400 °C . . . . .	97
4.9	2 Hour Holds at Mean Load - 500 °C . . . . .	98
4.10	Holds at 6.288kN Beach Marks Trials - 500°C . . . . .	98
4.11	RR1000 - Beach Mark Trial . . . . .	100
4.12	RR1000 Fracture Surface - 750°C R=0.7 . . . . .	102
4.13	RR1000 Fracture Surface - 525°C R=0.7 . . . . .	103
4.14	RR1000 Fracture Surface - Beach Mark Plan 1 . . . . .	105

---

4.15 RR1000 Comparison of edge crack length and average crack length . . . . .	107
4.16 RR1000 Fracture Surface - Beach Mark Plan 5 . . . . .	108
4.17 Beach Mark Plan 5 - Accuracy Plot . . . . .	109
4.18 RR1000 Fracture Surface - 25 $\mu$ m Marks equally spaced - Beach Mark Plan . . . . .	110
4.19 Beach Mark Plan - 25 $\mu$ m Marks - Accuracy Plot . . . . .	111
4.20 RR1000 Fracture Surface - Symmetrical - Beach Mark Plan . . . . .	111
4.21 Beach Mark Plan - Symmetrical - Accuracy Plot . . . . .	113
4.22 SS316-1 Fracture Surface - Beach Mark Plan 1 . . . . .	116
4.23 SS316-1 Fracture Surface Measurements . . . . .	116
4.24 SS316-2 Fracture Surface - Beach Mark Plan 2 . . . . .	118
4.25 SS316-2 Fracture Surface Measurements . . . . .	118
4.26 Steps in ACPD data on resumption of loading . . . . .	119
4.27 RR1000 - Fracture Surface - Low Magnification - Back Scattered Electron . . . . .	121
4.28 RR1000 - Test Area - Back Scattered and Secondary Electron Images . . . . .	121
4.29 RR1000 - R=0.7 Area - Back Scattered and Secondary Electron Images . . . . .	122
4.30 RR1000 - R=-1 Area - Back Scattered Electron Image . . . . .	122
4.31 RR1000 - Test Area 1 = Spectrum1 - R=0.7 Area = Spectrum 2 - Test Area 2 = Spectrum 3 . . . . .	123
4.32 RR1000 - Test Area 3 = Spectrum1 - R=-1 Area = Spectrum 2	124
5.1 SS316 Crack Growth Rates at Loading Frequencies 0.25 Hz and 0.012 Hz . . . . .	129
5.2 SS316 Crack Growth Rates at Loading Frequency of 0.012 Hz	130
5.3 SS316 Crack Growth Rates at 400°C . . . . .	130
5.4 SS316 Crack Growth Rates at 600°C . . . . .	131
5.5 RR1000 Crack Growth Rates . . . . .	133
5.6 RR1000 LCF 300°C . . . . .	134
5.7 RR1000 LCF 525°C . . . . .	134

---

5.8	LCF 750°C . . . . .	135
5.9	out of phase thermomechanical fatigue (OPTMF) 300-750°C .	135
5.10	in phase thermomechanical fatigue (IPTMF) 300-750°C . . . . .	136
6.1	Data from the Trials with the Matelect CGM-7 . . . . .	141
6.2	Impedance Plot - Geometry Samples . . . . .	143
6.3	Impedance Scaled for Wire Separation Plot - Geometry Samples	144
6.4	Phase Plot - Geometry Samples . . . . .	144
6.5	Samples with simulated quarter circular and tunnelled cracks .	145
6.6	Impedance vs Frequency Plot - Feature Samples . . . . .	146
6.7	Impedance vs Skin Depth Plot - Feature Samples . . . . .	147
6.8	Phase Frequency Plot - Feature Samples . . . . .	147
6.9	Phase Skin Depth Plot - Feature Samples . . . . .	148
6.10	Impedance Plot - Notch Width Samples Unscaled . . . . .	149
6.11	Impedance Plot - Notch Width Samples Scaled . . . . .	149
6.12	Phase Plot - Notch Width Samples . . . . .	150
6.13	Resistivity Calculation Plots - Geometry Samples . . . . .	151
6.14	Resistivity Calculation Plots - Featured Samples . . . . .	152

## LIST OF TABLES

4.1	Beach Mark Plan 1 . . . . .	104
4.2	Beach Mark Plan 2 . . . . .	106
4.3	Beach Mark Plan 5 . . . . .	108
4.4	Beach Mark Plan 5 - Results . . . . .	109
4.5	Beach Mark Plan - 25 $\mu$ m - Results . . . . .	112
4.6	Beach Mark Plan - Symmetrical - Results . . . . .	113
4.7	Beach Mark Plan SS316-1 . . . . .	115
4.8	Beach Mark Plan SS316-2 . . . . .	117
5.1	SS316 Crack Growth Rate Parameters . . . . .	129
5.2	RR1000 Crack Growth Rate Parameters . . . . .	133
5.3	RR1000 degree of tunnelling . . . . .	137

## 1. INTRODUCTION

Materials are subject to thermal and mechanical loading, understanding the affect of these on the materials is key to efficient design. Design optimisation is a significant market force as this saves money both in manufacture and, in the case of things such as aeroplane engines, in fuel efficiency. Therefore undertaking tests such as TMF is vital in understanding materials. Within LCF and TMF materials can crack and these can do so in a non-uniform manner, the focus of this work is to add to the ability to understand this better.

The University of Nottingham has, for many years, been undertaking LCF and TMF testing. This work had concentrated on strain controlled testing of high temperature steels and nickel alloys [1–3]. In this thesis, work has been undertaken to develop a crack growth capability, this has been based around the existing Instron 8862 load frame and associated induction heating system, which had been used extensively for many years in both LCF and TMF modes [2–5]. This uses an induction furnace for heating, and forced air cooling can be used to accelerate the cooling, passing air through the centre of hollow specimens. This rig was developed to allow crack growth rate testing, incorporating an ACPD system and the cooling system modified to work with solid instead of hollow specimens. A conventional fixed frequency ACPD system has been incorporated, validated and a range to test carried out. These tests have demonstrated the limitations of a fixed frequency system, showing a range of non-standard crack shapes, including non-circular and out of plane growth.

One way that crack front position and therefore crack shape can be recorded is beach marking, this is normally undertaken using a good amount of experience and judgment. Marks can be left by unplanned changes in

---

loading or by the user deciding on a change in loading that may give a mark on the surface. This approach has been used successfully in many studies, including in this thesis. However it would be beneficial to be able to reliably control the position and size of marks. A novel beach marking technique has been developed, this uses fracture mechanics to incrementally predict the position of the crack front at any given time and define the number of cycles needed to position marks at will. This technique reliably marks the crack's progression; however, as with all beach marking, changing between different loading conditions can affect the subsequent crack growth, in light of this a better measurement tool is needed.

A tool has been developed using alternating current (AC) at a range of frequencies to investigate crack shape. As the frequency of AC increases an ever-decreasing skin on the surface of the material carries the current, this is referred to as the skin effect. This advanced ACPD system utilises the skin effect to drive current through the sample in different paths depending on the thickness of the skin, sample geometry and the shape of any crack or feature. In a simple cylindrical conductor the current will flow in a uniform skin around the circumference of the conductor, however if the conductor has an apex or a feature in it this may not be true and the current field will be non-uniform. This will lead to a non-uniform electric field on the surface of the sample, which can be measured. In this work this technique has been developed and optimised to enable a range of frequencies to be passed in a short period, taking a snapshot of all the voltages at different frequencies. This has been shown to be sensitive to both sample cross-sectional geometry and the presence of crack like features.

This thesis details the work in the field of non-uniform crack shape monitoring, developing experimental equipment, and devising and implementing two novel techniques for recording crack shape. The test facility has been developed to test materials in LCF and TMF conditions while monitoring crack growth with ACPD, developing methods to overcome the challenges of this testing methodology. It has been demonstrated that non-uniform crack growth does occur in these tests and that conventional potential drop (PD) measurement does not have the sensitivity to probe this. A novel beach mark-

ing approach has been devised and developed to mark crack fronts and an advanced ACPD system has been developed. This unique work has started the development of the new ACPD system, proven the sensitivity and suggestions made for further implementation.

## 2. LITERATURE REVIEW

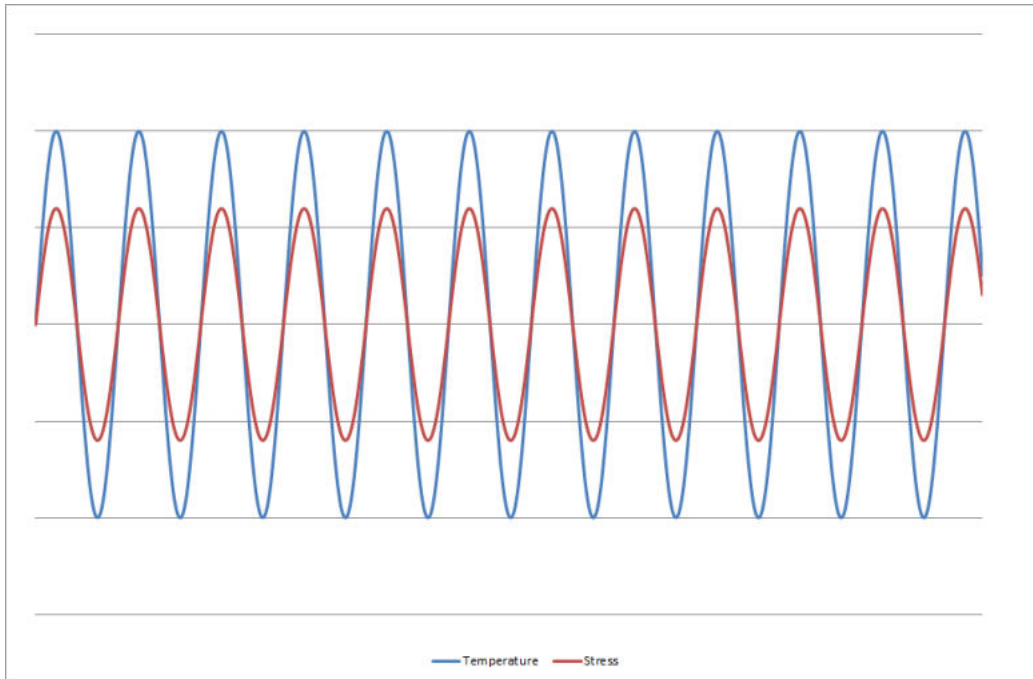
### 2.1 *Introduction*

The behaviour of materials in complex loading conditions is of significant importance, predictions of this informs decisions that impact the profit margins and more importantly the safety of critical equipment. This is most significant where monetary values are high and the result of failure impacts human life. Typical industries where these scenarios combine are areas such as aerospace and power generation, in particular nuclear power plant where a failure could have worldwide implications. Although the consequences of failure are high the benefits of running plant for longer are great, for example the current generation nuclear power plants are coming to the end of their design lives. Extension of these by another 10 to 20 years would have significant commercial effect and may even bridge the power gap until renewable forms of power generation are sufficiently developed to take over the load. These significant commercial, safety and environmental benefits drive the desire to better understand these complex systems and with better understanding there may be the opportunity to use equipment longer as with power plant or to increase service intervals on such things as aerospace jet engines. There may also be performance gains to be explored, for example increasing combustion temperatures in jet turbines increases efficiency and if the material behaviours at these elevated temperatures can be better understood performance improvements could be achieved without undue risk. Due to the high impact of these assessments they are consistently conservative and lead to underestimation of the lives of the components, for example the incident involving the United Airlines Flight 328 in February 2021 grounded 124 aircraft for many months, this was attributed to a fatigue

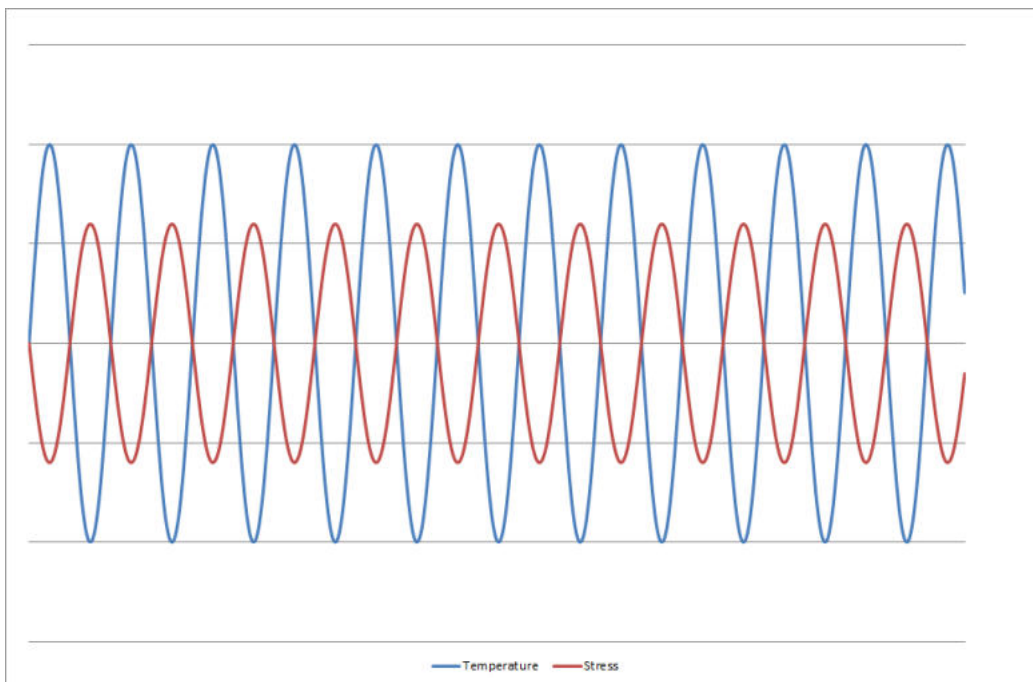
---

in the fan blades [6]. Better understanding of fatigue and crack growth behaviour would enable more accurate prediction of material and component behaviour resulting in more realistic approach to life prediction and therefore increased safety without the financial and reputational impacts.

The complex loading conditions are difficult or impossible to replicate experimentally so work focuses on more simple loading conditions, the most common being isothermal uni-axial testing, either high cycle fatigue (HCF) or LCF, where the parameters can be well defined and controlled. From these simplified tests estimations are made and often the material parameters measured from these tests can be fed into computational models. When TMF testing is undertaken it is usual to have an idealised condition, such as in phase (IP) or out of phase (OP) (fig. 2.1) and in some cases other phase angles such as 90° out of phase in either a clockwise or anticlockwise mode. The TMF testing is most relevant in the high temperature, highly loaded systems as mentioned above; in these systems there are elements of elasticity, plasticity, creep and fatigue all playing a part in the materials behaviour. These simplified tests represent only a limiting case which does not consider all the relevant phenomena encountered in real components, however they can produce material characteristics that can be fed into models. In addition to the simplified tests, more complex tests are undertaken to better understand how materials behave and the interaction of different damage modes, these can be mechanically multi-axial or more often TMF. These tests designed to simulate real world conditions can be used to help validate computational models. In these complex systems where multiple damage modes are present, non-uniform cracking occurs. In these condition the assumptions made in the models do not hold true and more work is needed to test and measure real cracks to feed into the models.



(a) IP TMF



(b) OP TMF

Fig. 2.1: IP and OP TMF Waveforms

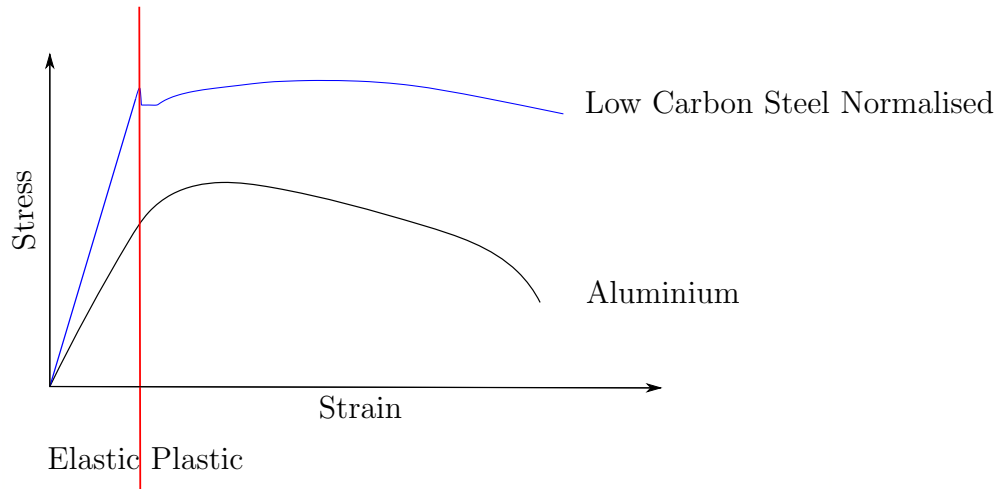


Fig. 2.2: Schematic Representation of typical Stress-Strain Curves from uni-axial tension tests

## 2.2 Materials Behaviour

### 2.2.1 Elasticity and Plasticity

All materials can undergo elastic deformation under loading, this is described by Hookes Law [7]. This can be seen in fig. 2.2 which shows two possible curves from displacement controlled uni-axial tensile tests. In this linear region (labelled 'elastic') if the applied load is removed the sample will return to the original shape travelling back down the same path as the loading. The magnitude of the deformation or strain ( $\epsilon$ ) due to the applied load or stress ( $\sigma$ ) can be described by the Young's Modulus ( $E$ ) [8]. This can be seen in eq. (2.1), in this case the Young's modulus is simply the gradient of the linear region.

$$\sigma = E\epsilon \quad (2.1)$$

At the end of the elastic region is the yield point where the strain is no longer elastic but now is plastic, and further straining is non-reversible. These two parameters, elastic modulus and yield stress ( $\sigma_y$ ), are very important as most engineering components work in the elastic range therefore their be-

---

behaviour can be predicted by their modulus below the  $\sigma_y$ . Beyond the elastic range is the plastic region, in this region the gradient of the two curves differ significantly. As materials plastically deform different mechanisms come into play and can result in a wide variety of responses. It can be seen in the case of the aluminium curve that there is an increase in the stress required to strain the sample up to a maximum and then this stress reduces. The stress increases due to work or strain hardening as the sample is stretched, in this portion of the loading the strain is uniform along the test section of the sample. In this example for a ductile material, once the ultimate tensile strength (UTS) is reached, at the top of the curve another mechanism takes over, this is local necking. Which is when one part of the sample fails and the rest of the sample remains in the form it achieved at the top of the curve, this reduction of stress is due to the reduction in cross-sectional area rather than a material change. It should be noted that here engineering strain and stress are being considered, engineering strain and stress are related to the original length and cross-sectional area of the sample, therefore the drop in stress is not a true picture of what is happening in the necked region. For this true stress would need to be considered and therefore measurements of the necked region would need to be taken, as true strain and stress related to the instantaneous length and area. This reduction in section is difficult to measure and also has little link to real world systems and design criteria unless the work is related to such processes as forming etc. where the part is to be significantly plastically deformed. The curve showing the normalised low carbon steel is included to show how different plastic straining can be, the elastic, work hardening and softening regions all have commonality with the aluminium example but it can be seen that the yielding behaviour is significantly different. In low carbon steel in this heat treatment condition there is a phenomenon called dislocation locking, this results in a higher stress being required to start the dislocations moving in the material leading to this sharp peak at the start of the yielding followed by a lower somewhat level once the dislocations are unlocked and are free to move, once this has occurred the material hardening continues. As inferred above the elastic deformation is only really affected by the applied stress whereas the plastic deformation in-

volves movement of microstructural features. If these tests are carried out at elevated temperatures there is normally a drop in  $\sigma_y$  and UTS, this is primarily due to the increased mobility of atoms in the material allowing movement more easily. This increased mobility of atoms can allow the dislocations to slide or slip along crystallographic planes with less resistance.

### 2.2.2 Creep

Creep occurs in loaded samples and components when the temperature is over a certain threshold, for metals this is typically over 0.3 of the melting point in Kelvin or 0.45 for ceramics [9]. Creep is analogous to plastic deformation in that it is none reversible and involves movement of microstructural features, it differs in that it is not only dependant on applied stress and temperature but also time. A typical creep curve can be split into three sections, Primary Creep where there is a decreasing strain rate occurring on initial loading followed by Secondary Creep with a constant strain rate and finally Tertiary Creep when approaching failure which has increasing strain rate, a schematic representation of this can be seen if fig. 2.3. In the secondary creep region, at stresses over a certain threshold, dislocation creep occurs. This mode occurs as the diffusion of atoms allows for the movement of dislocations through the microstructure, the rate of dislocation movement is determined by the rate of diffusion (linked to temperature) and the applied stress. The temperature controls the rate at which dislocations can slide along glide planes in the material. Once a dislocation meets an obstacle such as a precipitate it cannot continue to slide, at this point it needs to step to the next glide plane which is driven by the applied stress. Therefore it can be seen that the temperature and applied stress respectively determine the rate at which the dislocations glide and step, thus controlling the rate of creep strain accumulation. At stresses below this threshold diffusion creep occurs, this is at a much lower rate and does not involve dislocation sliding and stepping. In this mode the atoms diffuse through the grains allowing elongation in the loading direction. During the secondary creep voids form, often at grain boundaries which are perpendicular to the loading direction, these grow and eventually start to

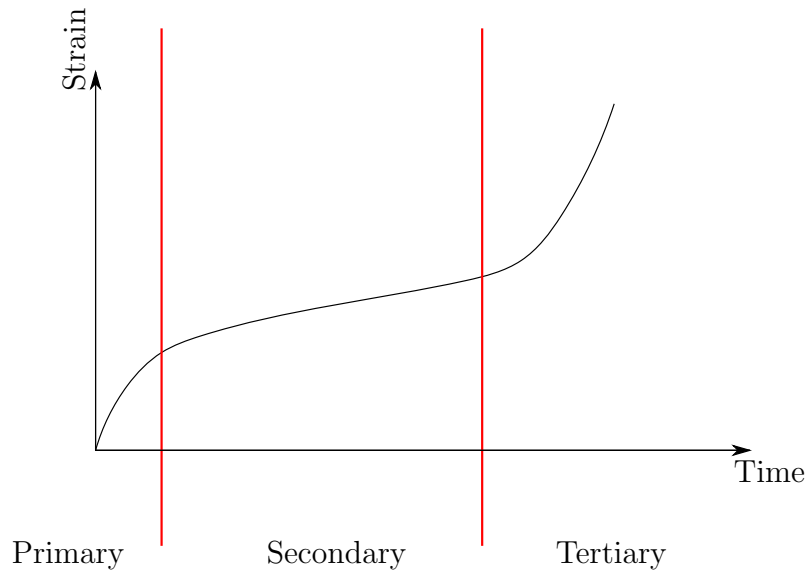


Fig. 2.3: Schematic Representation of typical Creep Curve

coalesce. The resulting void regions increase the stress on the remaining material in the grain boundary. As the effective stress increases, the creep rate accelerates and the voids join to form microscopic cracks. These microscopic cracking continues to grow and become macroscopic cracking which can be observed in the tertiary creep regime.

### 2.2.3 Fatigue

Mechanical fatigue is the repeated and reversed loading on a component, material or structure. This can take many forms in active service; it can be symmetric reversed loading in such cases as rotation axles which are subject to rotational bending moments, other parts can have either mean tensile or mean compressive loadings. This ratio ( $R$ ) of the minimum and maximum loads are often described by an  $R$ -ratio, which is the ratio between the minimum and maximum loads and can be between  $-\infty$  and almost 1, -1 being fully reversed, see eq. (2.2).

$$R = Load(max)/Load(min) \quad (2.2)$$

Fatigue was first noticed in the early 1800s with the advent of extensive mechanisation [10]. This new motion exposed materials to repeat cyclic loading. Also there was no understanding of the effect of geometry which can lead to stress raising features. This led to many unexplained failures.

Albert published some very early work, in 1837, on failures of chains in mines at sub failure loads and devised a mechanism to the test chains and decided that the chains needed to be replaced. Hemp ropes were the immediate alternative but these were expensive, so he designed a wire rope [10]. Some advanced ideas were considered by Rankine suggesting that the geometry of a body could affect its life (stress raisers) and that how it was cast and machined could contribute to its life [11].

The term ‘Fatigue’ appears to have been first used by Braithwaite [10,12] in work looking at a wide variety of machinery, including shafts, axles, cranes, levers and even brewery equipment [10]. Wohler did extensive work in the field of railway axles including the development of test apparatus and methods [10]. This included rotating bend apparatus, deflection measurement device and types of notched test. Wohler also came to many important and true conclusions, such as, the stress amplitude was of high importance as well as mean stress and the concept that an item could either be considered to have a limited or unlimited life. He concluded that if an item has an unlimited life then the designer could consider the two limiting factors, maximum service stress and maximum stress amplitude although for a limited life other factors had to be considered such as number of significant cycles which could limit life [10].

At the start of the 20th century a more analytical approach started to be developed. Griffith noted that a scratched (imperfect) glass had a failure load which was only in the region of one tenth of the theoretical value based on the atomic bonding. It was also noted that the strength of a freshly prepared fibre was closer to this theoretical value and diminished with time. This was due to flaws developing on the surface which acted as crack initiation points. He came up with his theory of brittle fracture based on the energy required to generate the new surface [13]. This work was not highly regarded until the 1950s as it appeared to have little use on normal engineering materials which

---

would exhibit plasticity as it only considered brittle fracture. This theory was taken and adapted by Irwin to take account of local plasticity in front of the crack tip [14]. This work by Griffith, Irwin and later Paris has formed the back bone of fracture mechanics [13–15]. The next main development of note is the concept of the J-integral developed by Rice in 1968 [16], the idea of a path independent variable which takes account of the elastic and the plastic field around the crack tip.

Post World War Two there was a great increase in civil aviation which brought on the next wave of fatigue related disasters. One of the most notable was the catastrophic failures of two Comet aircraft. These aircraft were one of the first jet powered civil aircraft and flew at about twice the altitude of propeller driven civil aircraft of the time. These ascents and descents to and from high altitude resulted in the repeated pressurisation and de-pressurisation of the fuselage leading to fatigue cracks growing from the corners of the windows. Unfortunately the design of the fuselage did not have the capacity to resist a catastrophic failure once these cracks grew to a critical size, once this size was reached the crack propagated rapidly through the fuselage resulting in two fatal accidents [17].

In more recent times there has been continued work in fracture mechanics and an increased interest in the modelling of systems to try to gain more accurate predictions of fatigue life. It would be most beneficial to be able to understand crack growth and from this data develop models to get reliable estimates of the life span of components. This can then either be used to optimise designs or increase confidence in the predictions of the working life of plant in such fields as nuclear power generation. An example of this sort of prediction work has been the development of a procedure (named R5) to estimate creep-fatigue life in structural components in nuclear reactors [18–20].

In the laboratory, fatigue testing can be performed, these tend to be conducted in more aggressive conditions than the service conditions due to limitations of time and equipment. This can be achieved by larger amplitudes or a significant increase in the frequency of the loading. Testing can either be in stress or strain control [21].

---

LCF is often carried out in strain control, this is most representative of heavily loaded parts and gives good control when the material is deforming plastically. As the material is deforming plastically the loading and unloading curves are different, hysteresis is observed. If the strain is fully reversed a stable hysteresis loop is often formed, see fig. 2.4. In this testing mode (strain control) the strain is fully reversed but the stress may not be, this is material specific and loading dependant. It is often seen that the material response changes during the tests so the minimum and maximum stresses change throughout the test see fig. 2.5. Often in an LCF test there can be an initial hardening or softening period, where the stress amplitude increases or decreases with each cycle. This can be followed by a stable region where there is little change in the minimum and maximum stress. Finally there tends to be a final softening before failure which can typically be attributed to cracking. If the waveform is not fully reversed then ratcheting can be observed as in fig. 2.6, this means that the load exerted on the material can quickly increase as it is cycled and tends to lead to very short lives. In strain controlled testing the rate of loading can be limited by the frequency response of the extensometer which may be only in the region of 1 Hz.

Typically HCF is performed in stress control as this is more representative of a part that is only experiencing an elastic load and this can allow higher cycle rates as extensometry is not required. In this style of testing there is generally no plasticity, this means that the loading and unloading paths are linear. Also if the mean load is not zero no ratcheting is observed. HCF testing is often performed with an R-ratio which is not -1, quite often an R-ratio of 0.1 is used thus keeping the part on test under a tensile load, this can make the fixturing used to hold the part on test more simple so the ratio of 0.1 is often favoured.

Materials and components can also undergo thermal cycling. This in itself can induce damage in the material but also if the component is restrained the expansion and contraction of the material can then induce a mechanical load. External mechanical loads can also be applied to parts, in the simplest case this can either work to decrease or increase the magnitudes of the thermal loads. This can be studied in TMF where we have both thermal

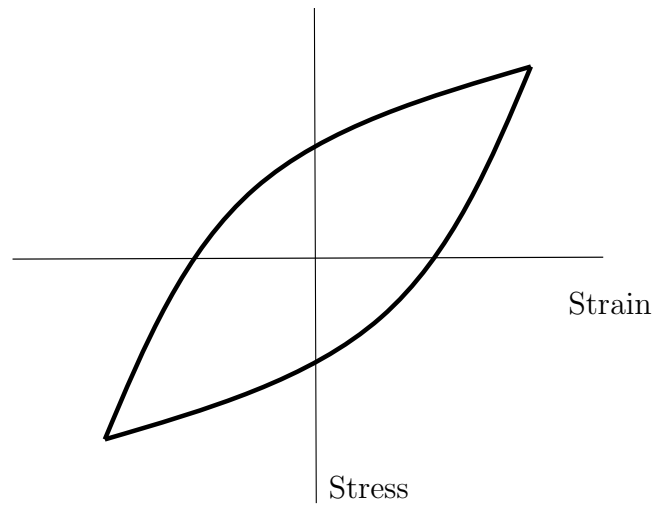


Fig. 2.4: Stress-Strain Loop

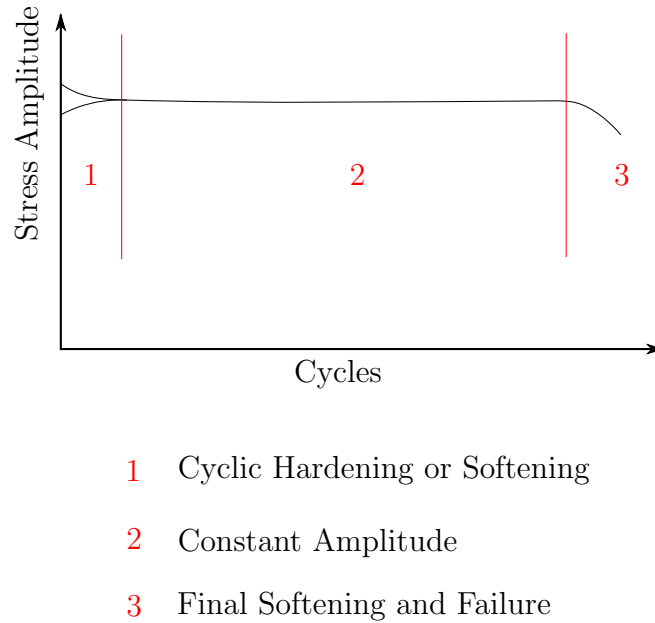


Fig. 2.5: Schematic Representation of Cyclic Softening and Hardening

and mechanical fatigue. Of course there are an infinite number of loading configurations but the most common in the lab environment is that the mechanical loading is either IP or OP with the thermal cycling, some schematic representations of these waveforms can be seen in fig. 2.1.

There are many similarities between LCF and TMF. The majority of TMF testing is undertaken in strain control and similar changes in material, softening or hardening etc. can often be observed. However the stress-strain loops can be different as the material changes stiffness or deforms plastically in a different manner due to temperature changes. If running an OP waveform the stress strain loop is normally asymmetric becoming more elastic at lower temperatures. In the most simple cases the IP testing tends to give shorter lives due to the maximum tensile load being at the highest temperature when the material will be at its weakest and creep can be significant at low cycle rates [2]. This is not the only contributing factor, mechanisms such as surface oxide cracking can lead to OPTMF giving shorter lives [23,24]. So it can be seen that TMF is very complex and many experimental tests are

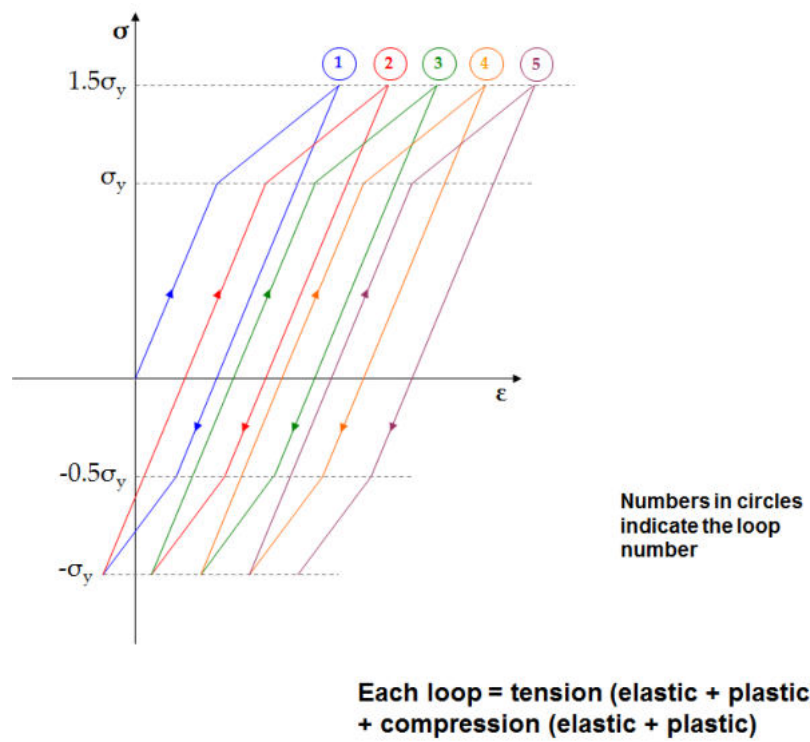


Fig. 2.6: Schematic Representation of Ratcheting Behaviour [22]

required to understand the fatigue properties in these conditions. Some work has been done to try to simulate real world systems in ‘complex fatigue’ [25] where the waveforms can deviate from the simple IP and OP scenarios to simulate the loading seen in jet engine components during a flight. These sorts of tests can lead to significantly different loadings than are typically considered although this leads to a great number of possible loading regimes which may be impractical.

#### 2.2.4 Dynamic Strain Ageing

DSA was first studied in detail in 1923 by Portiven and Le Chatelier [26], in this work the serrations in the stress strain curve for aluminium alloys was studied, this became known as the Portiven-Le Chatelier effect (PLC). DSA also is manifested in another form; in a tensile test a Lüders front can be generated, this is a region of high strain which travels along the length of the specimen between the plastically un-deformed region and a plastically deformed region.

The serrated yielding in DSA can be classified in to a number of types (A to E), a schematic showing these types can be found in fig. 2.7. Types A to C and E are seen in constant displacement rate tensile testing whereas type D is seen in load controlled testing. All the modes are associated with the formation or release of dislocation of shear bands and the propagation of these through the sample. This leads to a strong dependence of this on temperature and loading rate. The rate of accumulation of damage and reordering within the material need to be in the correct balance to allow DSA to occur. This means that there is a strong link to loading rate, which affects the rate of accumulation of damage and the temperature which effects diffusion rates thus the rate of reordering in the material. It has also been shown that small compositional changes [28] as well as grain size [27] can affect the presence and type of DSA observed. This sensitivity to compositional changes is also relevant when considering environmental effect, for example it has been shown that the ingress of hydrogen and related hydrogen embrittlement in steel affects the DSA response [29]. DSA has been reported in a range of

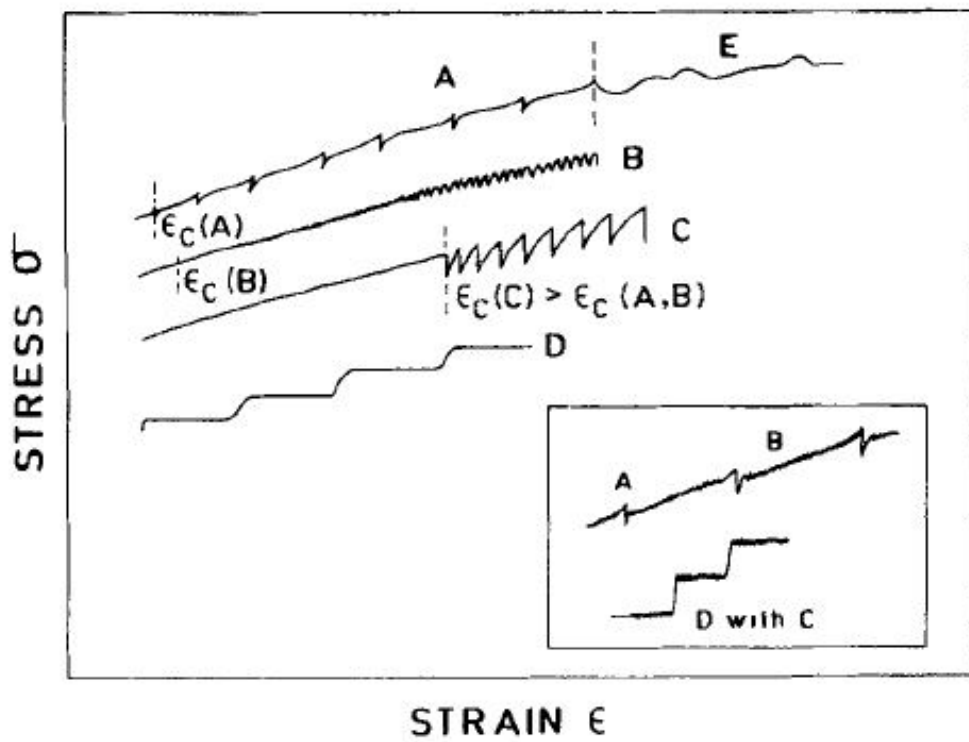


Fig. 2.7: Schematic of Types of Serrations due to DSA [27]

---

material type including aluminium alloys, steels [30], inconel and other more exotic alloys [31].

### 2.2.5 Mutli-mode Behaviour

In the previous sub-sections different material deformation behaviours have been described, this however is not the whole story. In many real world environments parts and structures may experience more than one mode, for example a loaded component of non-uniform geometry may undergo plastic deformation in specific regions when other regions are remaining elastic, this may lead to work hardening and then the increased yield stress in the plastically deformed region thus this area can sustain higher load and remain elastic. This may lead to redistribution of loading again changing the stress field.

In many high temperature environments such as jet engines fatigue and creep may well happen at the same time, and the damage mechanisms can interact. Depending on loading frequencies and temperatures these may have various effects and may change the subsequent life of components. fig. 2.8 (courtesy of Yan et al) [32] shows the region in a strain vs cycles (SN) plot where this may be significant, it can be seen that it is in the middle region where neither creep or fatigue dominate. In the laboratory this can be explored using LCF and TMF testing, and can be seen in different cracking modes, typically creep can lead to more intergranular cracking due to the accumulation of damage at grain boundaries. This is often seen in IPTMF and higher temperature LCF due to the high temperatures and high stresses combining to encourage creep. Whereas OPTMF and lower temperature LCF can be more dominated by fatigue. IP and OP can be considered as the most simple TMF conditions but work has been done to demonstrate that other phase angles are significant and whether this phase relationship is clockwise or anticlockwise can also play a role [33].

Environmental effects have also been shown to play a role, it has been shown that oxidation can make a significant contribution, this can occur preferentially at grain boundaries in such materials as nickel alloys and chrome

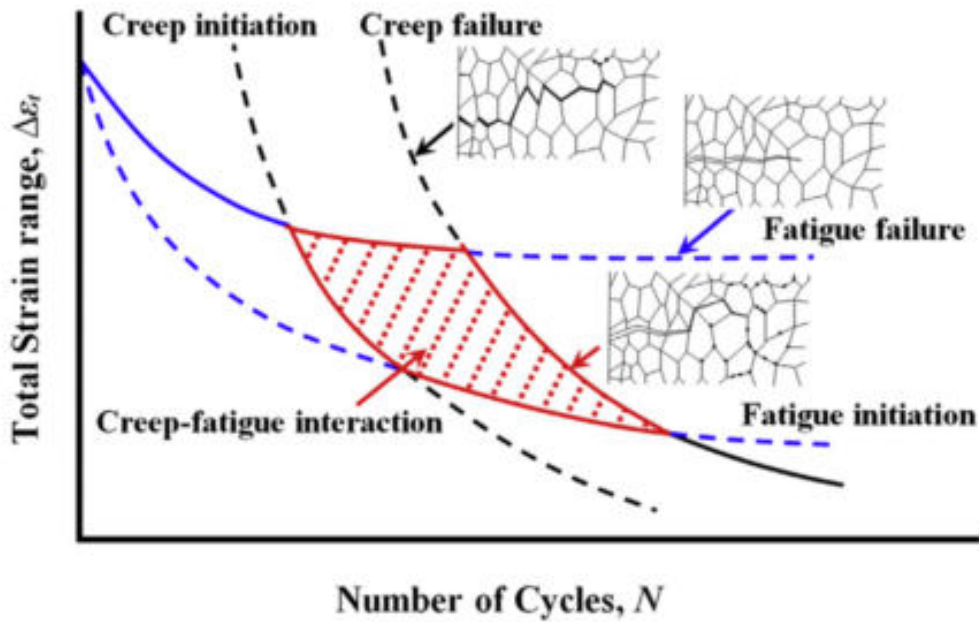


Fig. 2.8: Schematic of the Regime where Creep-Fatigue Interaction is Significant [32]

steels [34]. This oxidation at grain boundaries can combine with creep damage thus having a significant effect on component life, however it should be noted that creep damage occurs throughout the thickness of the materials whereas oxidation can only contribute near the surface as the oxygen has to diffuse through the material. Surface oxidation can also play a role in crack growth, a surface oxide film which may have formed in an unloaded case can crack on tensile loading and this crack can propagate into the base metal [35,36] and in other work it has been shown that a stable oxide film can protect the sample from the environment [37]. Some work has also been carried out to understand the effect of other environments such as those found in Pressurised Water Reactor (PWR), this highly aggressive environment has been shown to be very detrimental to SS316 [38].

In summary it has been shown that these mechanisms all contribute to high temperature material performance and depending on the conditions of temperature and loading materials can behave in a wide range of fashions. Trends can be noted although these are not all encompassing and much

---

more understanding is required to understand their relationships for different materials and conditions. These complex loading modes have driven a desire to undertake computational modelling and associated materials testing to better understand materials behaviour [39].

## 2.3 Electrical Properties

Many of the suitable crack measurements both in laboratory tests and on real plant are electrically based, it should also be noted that the work within this thesis to develop an advance ACPD system will rely on these properties.

### 2.3.1 Direct Current

In DC the flow of an electrical charge is in one direction, this can be in a material or even in a vacuum by means of electron or ion beams. This was discovered by Alessandro Volta in 1800, he found this by studying electro-chemical cell or a voltaic pile, which was the first battery. In this initial work the nature of current flow was not understood, until Andre-Marie Ampere conjectured that current travelled in one direction from points of positive voltage to points of negative voltage.

DC is a unidirectional system current flowing in one direction, the voltage at any point in a circuit that has achieved steady state will remain constant with time. The relationship between the voltage (V), current (I) and resistance (R) between the two measurement points can be described by eq. (2.3)

$$V = IR \quad (2.3)$$

When considering DC current flow; the only material property affecting the response is the resistivity ( $\rho$ ), if the length of the conductor (L) and the cross sectional area (A) is known the relationship can be described by eqs. (2.3) and (2.4).

$$R = \frac{\rho L}{A} \quad (2.4)$$

This is key in using Direct Current Potential Difference (DCPD) in that

---

it demonstrates that the voltage change measured is linked only to the area of the remaining material in the plane of the crack, often referred to as the remaining ligament, therefore can be linked to crack area. If the geometry of the crack is known or can be reasonably assumed then the crack length can be calculated.

### 2.3.2 Alternating Current

In considering AC the constantly changing electric field results in a magnetic field which affects on how the current flows in the conductor. This results in the skin effect, where the current does not flow uniformly in the conductor as with DC current, but in a reduced thickness near the edge of the conductor. The thickness of this skin is related to the material properties and the frequency of the AC current. Frequency is important as this describes the rate of change of the electric field and therefore the strength of the resulting magnetic field.

The relationship between electric and magnetic fields was first discovered by James Maxwell, and these equations are still in use today. He first published his Lines of Force [40] in 1861 and followed this in 1873 with the text book A Treatise on Electricity and Magnetism [41], in which his main equations were published. These are now commonly referred to as the The Maxwell Equations, and describe the interactions of electric field and the magnetic field .

The magnetic field gives rise to an electric field in the opposite direction to the applied current, this is termed a back electro-motive force (EMF). The field strength is greatest in the centre of the conductor and reduces towards the edge, resulting in the cancelling out of current in the centre section of the conductor. This manifests as a skin of current flowing in the conductor hence the name, skin effect. In the work presented later, changing the thickness of the current containing region gives the ability to probe features at different depths in the samples. The Maxwell Equations can be used to derive a simple equation (eq. (2.5)) for the thickness of this skin ( $\delta$ ) [42], given the resistivity of the conductor, the frequency ( $f$ ) and the permeability ( $\mu$ ) of the material.

$$\delta = \sqrt{\frac{2\rho}{2\pi f\mu}} \quad (2.5)$$

The skin effect drives the effect seen in ACPD, where the current flows in a thin surface layer. As the crack grows the perimeter of the samples effectively gets bigger as the current needs to flow along the newly formed surface of the crack, this longer path length then gives rise to the larger potential between the measurement points.

## 2.4 Materials

### 2.4.1 High Temperature Steels

Two important steels in the power generation industry are SS316 and 9Cr-1Mo Ferritic-martensitic Steel (P91), SS316 is often used for high temperature structural parts of nuclear reactors and P91 is used in steam pipes for nuclear and other types of power station [43]. Other austenitic stainless steels are also used in nuclear plant such as 321 [20]. The fabrication method for most of these structures is welding, this leads to heat affected zones which can often have lower creep and fatigue resilience. These materials can be subject to prolonged periods at high temperatures under constant mechanical load as well as cyclic loads and thermal cycles so creep, fatigue and the creep-fatigue interactions are of high importance. At lower temperatures and higher loading frequencies fatigue cracking tends to be the most significant. If temperatures are increased, frequencies reduced or hold times incorporated into the loading regime then creep and creep-fatigue can be observed. The crack growth in fatigue tends to be transgranular [44] initiating from surface defects [45], creep and creep-fatigue cracks are typically intergranular.

### 316 Stainless Steel

Work has been carried out to understand the high temperature performance of SS316. In strain controlled LCF testing at elevated temperatures it has been seen that the material initially hardens over the first 70 to 100 cycles

showing an increase of peak load then a slow softening for most of the life ending in a rapid softening as cracking becomes significant [43,46]. Although the hardening and softening trends hold true for a variety of loading regimes, environmental conditions and loading waveforms can have an effect on life.

Above 400°C there is a significant drop in the material properties of SS316, when below 300°C there is little effect of temperature [47] and environmental conditions [24] meaning below 300°C it is very stable. The strong dependence at higher temperatures has been attributed to creep [23,47,48] even seeing a reduction of life in LCF to a quarter when creep hold periods are introduced to the loading cycle [44]. Oxidation is also important [23] and if the sample is tested in a vacuum a six fold increase in life can be observed [49].

In LCF testing it is generally seen that higher temperatures lead to shorter lives, with TMF testing it is a little more complex. It is seen that the TMF lives fall in between the LCF at the minimum and maximum temperatures, although depending on the temperature range OPTMF and IPTMF can have differing lives. At sub-creep temperatures it has been seen that OPTMF has a shorter life than IPTMF this is attributed to two factors. With OP loading there is a positive mean stress due to the stiffness of the material increasing as the maximum strain is exerted resulting in a higher stress in tension than compression. Oxide cracking can also be significant, at the high temperature in compression oxides form then as the temperature drops and the tensile strain is applied to the specimen the oxide cracks and these cracks then propagate into the base material. At higher temperatures where creep is significant there is a reversal of this trend and the IPTMF has the shorter life which has been attributed to the significance of creep in the tensile loading [23,24,43].

DSA has also been observed in both uni-axial tensile and LCF testing of SS316. This is seen temperatures ranging from 250°C to 650°C and strain rates from  $10^{-5}\text{s}^{-1}$  to  $10^{-3}\text{s}^{-1}$ . This effect can be observed in the stress strain curves or plots of peak stress against number of cycles manifesting as saw tooth patterns or steps in the plots. The mechanism for this is the interaction of the dislocations and solute atoms and their relative rate of generation and diffusion hence the dependency on strain rate and temperature [30,50–53].

This interaction tends to lead to a rise in fatigue strength due to increased resistance to plastic flow due to these iterations, but can also lead to embrittlement so can result in a shorter fatigue life [44, 54].

### *9Cr-1Mo Ferritic-martensitic Steel - P91*

P91 is widely used in the power generation sector for such parts as steam pipes, headers, and is often chosen for this application due to its high strength and low coefficient of thermal expansion [3]. In these conditions the material is subjected to a creep loading condition due to the internal steam pressure and the loading due to thermal expansion or contraction, the thermal cycling due to plant start-up and shut-down also introduces fatigue loading into this system.

In comparison to SS316, P91 does not go through an initial hardening stage at the start on an LCF test. An initial softening is seen followed by a large region of slow softening and finally a rapid drop in strength prior to failure. In the first and second stages the softening is due to coarsening of the sub-grains and cracking is only seen in the third region of rapid weakening [3]. This alloy also shows shorter lives at higher temperatures and holding a constant load in either tension or compression have a detrimental effect on life [43].

The loading regime that results in the shortest life is isothermal fatigue (IF) at the maximum temperature of the TMF cycle. When IPTMF and OPTMF are compared it is found that OP cycling leads to shorter lives due to the cracking of the brittle oxide, which is formed at high temperature in the compressive phase, as the sample is taken into tension [43]. This is born out when looking at tests with either tensile or compressive holds, in air these hold are quite detrimental to fatigue life whereas in a vacuum this is not observed. This is also affected by strain amplitude, the presence of oxide at small amplitudes where the oxide may not crack on loading are much smaller when compared to higher strain amplitudes where the oxide cracking propagates into the steel and initiates a crack in the material [34, 55].

DSA is also observed in P91 in tensile and LCF conditions in a wide

temperature range. In tensile loading types A, B and C have been shown to occur, this has been shown to be affected by heat treatment condition but is mainly controlled by the temperature. At low temperatures from 250°C type A is present, B and C develop as temperatures increase up though to 400°C [56]. This also manifests in both tension and compression in LCF loading, in these temperature ranges about 250-400°C [55].

As welding is a necessary part of the fabrication of steam plant there has been some work undertaken to understand the creep crack growth behaviour in welds and heat affected zones (HAZ). [57, 58]

#### 2.4.2 High Temperature Nickel Alloys

A range of nickel based alloys have been developed to cope with the very high working temperatures in jet turbine engines and also to a lesser extent land based power plant. In developing these alloys a number of metallographic properties have been used to give high strength, good creep resistance and protection from harsh, high temperature environments. These high strength and low ductility alloys have been considered creep brittle [59]. Titanium and aluminium are typically added to increase the  $\gamma'$  - Ni<sub>3</sub>TiAl intermetallic phase. This phase strongly resists the movement of dislocations. Heat treatments can form a highly ordered structure with the  $\gamma$  as the primary phase and  $\gamma'$  as a fine secondary phase dispersion. This structure has high strength and creep resistance. Other elements such as tantalum are added increasing the  $\gamma'$  fraction and  $\gamma'$  strength, also zirconium is added as it can react with the oxygen and sulphur in alloys. Oxidation is also a problem and chromium is added as it preferentially oxidises thus protecting other elements in the material [60].

The processes of powder metallurgy (PM) and hot isostatic pressing (HIP) are also utilised to closely control the properties of the material although the use of PM can result in other weaknesses. Ceramic inclusions, remnants from the powder processing, can be present in the final material. Attempts are made to minimise these by sieving the powder before the HIP process. However, small particles can still be present and these are the most important

defect causing crack initiation [61] Also the presence of voids following HIP can also initiate cracks [59]. With PM materials it can be considered that as the size of the part increases there is an increased chance that a significant particle inclusion, void or other flaw could be in a critical location, such as a surface, which could lead to crack initiation [60]. These PM materials are very uniform and homogenous, however it has been seen that the junction of different grains can be an initiation point for cracking [62]. So it can be seen that these PM materials have excellent properties but great care is required when working with these.

Nickel alloys can be utilised at high temperatures and only show decreased performance at temperatures, depending on the alloy, in excess of 500°C. Significant amounts of LCF work have been done to study the performance of these materials at a range of temperatures. It has been reported that at lower temperatures there is little effect of temperature increases up to a temperature threshold, which is alloy dependant. Over the threshold the cracking mechanism changes from purely fatigue based transgranular cracking to intergranular cracking. This intergranular cracking is quicker [63] than the transgranular leading to lower LCF lives. [2, 60, 63–66].

This higher rate of intergranular crack growth is primarily due to the susceptibility of the grain boundaries to oxidation embrittlement [59, 67]. The oxidation effect has been shown to be strongly dependant on the partial pressure of oxygen in the test environment, above a certain pressure then the cracking mode changes from transgranular, at low partial pressures and in a vacuum, to faster intergranular cracking [66, 68]. This oxidation has been shown to happen ahead of the crack tip using atomic probe tomography to map the oxide formations [69]. This happens quickly, a significant embrittlement can be seen after only ten seconds of exposure [59], so intergranular cracking is dominant unless the loading frequencies are very high. The oxidation effect is only seen at higher temperatures in excess of 400°C to 500°C [64, 65] above these temperatures the life can be linked to the time at temperature whereas below such temperatures the life and crack growth rate can be linked to the number of loading cycles [64, 65]. This decrease in life as the temperature increases is likely to be due to the increased diffusion rate of

---

oxygen into the material as the temperature rises, this time at temperature dependency is not seen in a vacuum [66]. One of the highest performance alloys is RR1000, this is very stable being able to operate in temperatures up to 650-700°C without any grain growth [70], notable grain growth does not occur until close to the gamma prime solvus at around 1145°C.

## 2.5 Crack Measurement

Crack measurement both in service and in laboratory tests [71] can give a good measure of the progression of fatigue damage as this can often be associated with crack formation in the material [72]. Plant and jet turbines are known to have cracks present during normal operation [2], periodic inspection can be carried out and if enough is known about crack growth rates then the remaining life can be estimated. There are a number of methods that can be used for this including, dye penetration, crack opening displacement (COD), ultrasound as well as a range of electromagnetic techniques. The electromagnetic techniques can be eddy field, magnetic flux leakage or a potential drop technique [73].

### 2.5.1 Penetrants

Penetrant techniques have been used for many years, they started by using oil and whiting [74]. In modern times dark coloured dye is used. These techniques can only detect surface cracks that are on the outer (visible) surface of a component. This process involves first applying a penetrant (typically a dark coloured dye) to the surface to be inspected, an amount of time is allowed to elapse then the excess dye is wiped off the surface. If cracks are present some of the dye will have seeped into the cracks and will remain there after the excess has been removed from the surface. Then a chalk dust is applied to the surface, this draws out an amount of the dye from the cracks by capillary action. The contrast between the light coloured chalk and the dark dye then allow the location and lengths of the cracks to be observed. This is a suitable technique for determining the presence of

---

surface cracks but does not give any understanding about the depth of the cracks into the material.

### 2.5.2 Surface Measurements

In situations where the crack can be held open by applying a tensile load it is often possible to view the crack on the surface. This can be achieved in laboratory specimens in high rate tests by pausing a test and holding the sample under a tensile load or if the loading rate is slow it may be possible while the test is running. The crack length can then be measured by the operator using a microscope or a camera could be used to automate this, which can be aided by timing the exposure of a camera to match the maximum load in the cycle. This approach works well if the location of the crack is known, as in pre-notched specimens.

Another technique which can be used when the crack initiation site is not known is to take replicas of the surface. To do this a polymer sheet is soaked in solvent to soften it, then placed on the surface. Once the sheet has hardened and taken the shape of the surface, it can be removed and stored as a replica of the surface at that point in time. This can be repeated many times as the loading continues and once a crack is clearly visible its growth can be tracked back through the replicas, enabling the tracking back of a crack to its first time on the surface. This is time consuming but can be effective.

Surface measurements, regardless of how they are taken can be limited as the crack may not grow in the same way at the free surface as in the bulk material. However for uniform cracks this can be effective, in particular if an automated system can be used to take images and possibly calculate the crack location.

### 2.5.3 Crack Opening Displacement

COD can be used on laboratory specimens under test, this is predominantly done in either a tensile or bending configuration. Typically the specimens have features machined into them for the gauge to clip onto, there would also

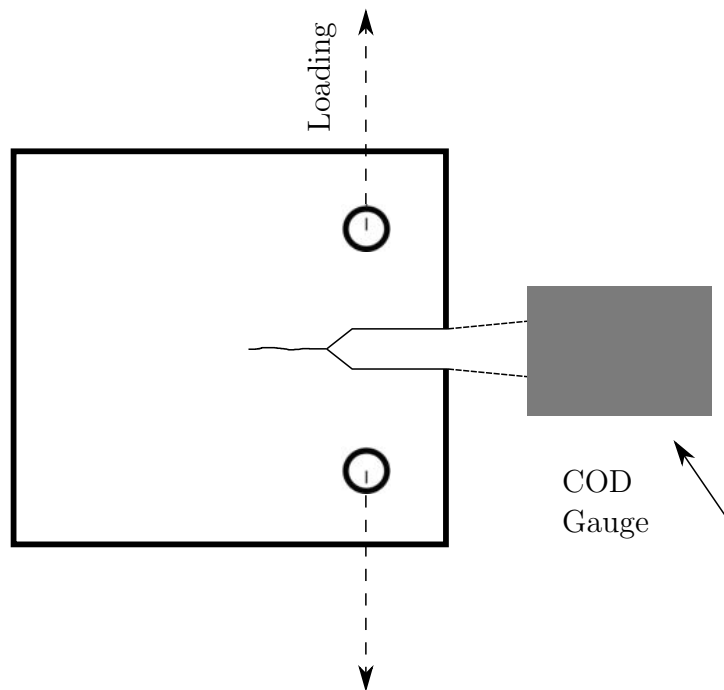


Fig. 2.9: CT Specimen with COD Gauge

be a starter notch machine at the centre position in between these features to initiate the crack. The presence of the notch ensures that the crack will start in the centre of the gauge and that any stress raiser around the COD mounts will be insignificant. The separation of the COD mount features determines the gauge length of the transducer so needs to be known before specimen manufacture. A schematic of a typical Compact Tension (CT) type specimen with a COD gauge mounted can be seen in fig. 2.9.

With knowledge of the COD data with cycles, the specimen geometry and the elastic modulus of the material a range of crack growth parameters can be calculated. Assumptions need to be made about the shape and uniformity of the crack, as with other measurements such as most PD measurements.

#### 2.5.4 *Ultrasound*

Ultrasound is typically used for inspection of parts, quite often in service. This technique employs a workhead which encompasses an emitter and a sensor, this is placed on the surface of the component and a short wavelength sound wave is injected. The sound propagates through the component, if there is a feature such as a crack in the component the wave is reflected back to the workhead, the sensor element then receives the signal. With knowledge of the speed of sound in the material and the time between the emitted signal and received signal the depth of the feature can be determined. The workhead can then be rastered over the surface of the component, often by a human operator, and from this the size of the feature (possibly crack) can be determined. It should be noted that this is only sensitive to planar features that are parallel to the surface of the part. If features are perpendicular, there will be very little surface for the sounds to reflect off therefore very little signal will be received, also if a feature is at an oblique angle the reflected wave will be at an angle to the emitted wave and will not return to the workhead.

This is a very flexible technique that needed minimal preparation of the item on test, which makes it very useful for in service inspections. However this has little to no use in laboratory materials testing experiments, typically cracks in test pieces are not parallel to a surface and the option of moving a sensor head around with sufficient resolution is unlikely.

#### 2.5.5 *Eddy Currents*

Eddy field and Magnetic Flux Leakage techniques have been put to good use in inspection of such things as pipes. These both involve inducing a field in the material to be inspected and monitoring the change in this field caused by discontinuities in the part, if the material is uniform these discontinuities are often cracks. This sort of effect was first noticed by William Hoke [74,75] when he magnetised a gun barrel and applied ferromagnetic particles to the surface. These would gather at a discontinuity as the magnetic flux leaked out of the crack in the barrel. This technique is still used to inspect some parts in a qualitative manner as with dye penetration. This magnetic flux

leakage can also be measured by using a travelling sensor across the surface and monitoring peaks in magnetic flux. There are a number of problems with this technique. The part under test must be ferromagnetic so this cannot be used on materials such as aluminium or austenitic stainless steels also it is only sensitive to cracks that run perpendicular to the direction of the magnetic field, if the cracks run in line with the field then minimal leakage occurs.

Eddy field techniques involve inducing an electrical current in the part to be inspected and monitoring the resultant field produced from this. If there are no changes in the material as the sensor head moves across the part then no change is detected in the readout, if there is a feature such as a crack then a change is observed in the detected field. Probes can be simple hand held surface devices which are moved over a surface to detect cracks. In the pipe and boiler industries where there is interest in monitoring the inside of tubes, devices have been developed which can be inserted into and even drive down the inside of pipes and tubes. These can then monitor the condition of the inside of these pipes. Work has also been done to determine the shape and size of cracks from this information. This has involved using computer models to predict the resultant field generated by cracks of different size and shape, a complex problem which can yield crack shape information [76, 77].

#### 2.5.6 Beach Marking

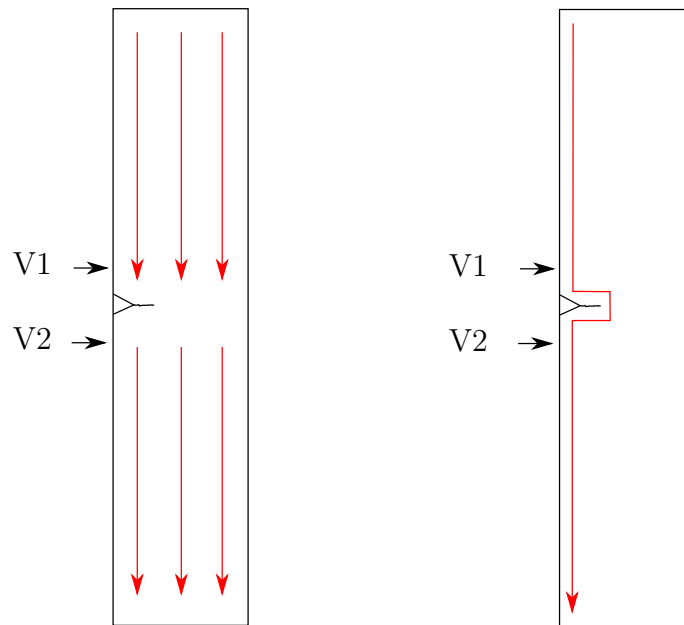
Beach marks are macroscopic marks on fracture surfaces giving an indication of the progression of the crack. These are normally generated by changes in the microscopic structure, the variation results in light reflecting from the surface differently which lead to differences in colour or brightness this is normally recorded by use of a camera or light microscope. It is also possible to observe this in an SEM, where the electrons are also scattered or absorbed in to different degrees with changes in microscopic texture. The oxidation process can also be used, this can be called a 'heat tint' [78] whereby if the sample is held at temperature without cycling, increased levels of oxidation on the existing crack surface can give a contrast with further crack growth

that is still yet to happen.

The methods to generate a difference in texture varies between materials and test conditions. Therefore different strategies are used, the one chosen tends to be based on experience and limitations of the testing apparatus. Methods used to make the marks tend to be less aggressive than the normal loading so as to affect the test as little as possible. These may include; holds at zero, mean or max load, cycling at reduced amplitude or an increased R-ratio. If cycling is used it is often undertaken at a higher frequency to speed the test and potentially change the cracking mode to increase the difference with the test loading. [79–82]

### 2.5.7 *Electrical Potential Drop*

Potential drop techniques can be split into two broad categories; DCPD uses a DC source to drive the current through the material, a voltage can then be measured across a crack which will increase with crack length. This voltage change is due to the remaining element reducing as the crack extends, this thinner element has a higher resistance so the voltage drop across the crack increases. ACPD is similar to DCPD in that a current is driven through the part, although this is an AC and this current can normally be substantially smaller than the DCPD. The current can be smaller due to the skin effect and current tunnelling that can be exploited when using AC. Skin effect means that the current flows through a thin layer at the surface of the part which is much smaller than the full depth of the sample as in DCPD. Also the current has more directionality so current passes only between the input and output probes with minimal losses via other routes. The skin effect means that the voltage measured is not due to the thickness of the remaining material but is because the path length through which the current flows increases as the crack grows [83]. In DCPD the sensitivity is linked to the remaining ligament, this means that it can be insensitive to small cracks where the crack and crack length change is very small in comparison to the size of the remaining material, this is generally overcome by the use of high gain amplifiers and quality instrumentation. However this is not the case in ACPD



Vx - Voltage Measurement Locations

Left - DCPD - Uniform Current Flow

Right - ACPD - Current Flowing on the Surface (Skin Effect)

*Fig. 2.10:* Direct and Alternating Current Flow

as the voltage change is directly linked to path length change, therefore the sensitivity is uniform regardless of crack length. A representation of the different current flows can be seen in fig. 2.10.  $V_1$  and  $V_2$  indicate two positions, either side of a feature from which a crack is growing, between these points a voltage drop can be measured. As this crack grows it can be seen that the amount of remaining material decreases so in the case of DCPD the potential difference between these two points increases. Likewise in the case of ACPD this potential can be measured, although in this case the difference will increase with crack length due to the increased distance that the current travels to get between these two points.

The previous paragraph has described the laboratory use of potential drop techniques. Some work has also been carried out using both ACPD and DCPD with both the current input and voltage measurement probes in a mobile sensor head to map the cracks on components. The sensor head is moved taking measurements at different points around a crack, the recorded voltage changes due to the different spacial relationship between the probes and the crack. This can then be used to evaluate the location and size of the crack [73, 84, 85]. A similar approach has also been used for laboratory specimens, by welding multiple sets of measurement wires onto a specimen at distances from the starter notch [86]. In addition to this a small amount of work has been undertaken to attempt to track the direction of cracks in laboratory specimens. Spitas et al have done some work in this field using DCPD [87], in this they passed a DC current through a specimen designed to exhibit pure shear loading and therefore an angled crack. They demonstrated that it was possible to understand the direction of the crack by using two pairs of measurement wires located across the starter notch. Some preliminary work has also been published from this project showing that the shape of a conductor affects the measured ACPD response [88], this suggests that the current in non-circular conductors is not uniformly linked to skin depth.

The ACFM has been used to determine crack shape by taking multiple measurements along the surface of the material where the crack is present at the surface. These readings of PD at different locations can be used to map the depth crack along its length and thus its shape [89]. This approach

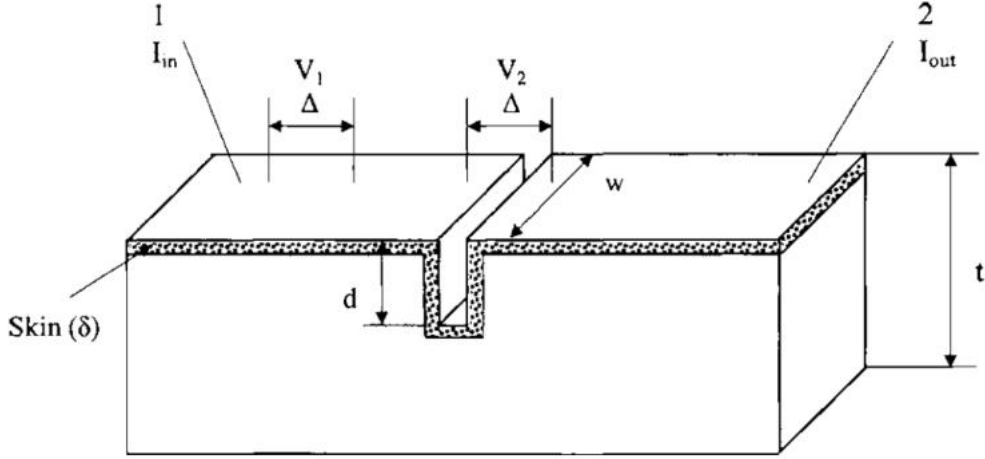


Fig. 2.11: Thin Skin ACFM [91]

works well for wide cracks where the current must flow down into the material and past the crack front, however when the cracks are narrow compared to their depth significant errors can be seen due to the alternative current path around the side of the crack [90]. ACFM has mainly been assumed a very thin skin where all the current is passing, therefore the voltages measured can be closely linked to path length which is approximately twice crack depth. It has been shown for this thin skin approach, that if two measurements are made voltage on an un-cracked areas ( $V_1$ ) and the voltage across the crack ( $V_2$ ) the voltages can be linked to purely the gap between the probes ( $\Delta$ ) and the crack length ( $d$ ). [89]  $V_1$  is simply  $\Delta$  and  $V_2$  is  $\Delta + 2d$ . In this case the crack length can be determined by eq. (2.6), where  $t$  is the part thickness and  $w$  the crack width. A schematic representation can be seen in fig. 2.11.

$$d = \frac{\Delta}{2} \left( \frac{V_2}{V_1} - 1 \right) \quad (2.6)$$

At lower frequencies a thick skin situation occurs, it is considered that the skin is thin when the conditions in eq. (2.7) are satisfied and a thick skin in any other condition. It is considered that in a thick skin condition eq. (2.8) can give an approximation of the crack depth [91,92].

$$\frac{t}{\delta} > 10, \frac{d}{\delta} > 10, \frac{w}{d} > 10, \quad (2.7)$$

$$d = \frac{\Delta}{2} \left( \frac{V_1}{V_2} \right)^{\frac{1}{2}} \left( \frac{V_2}{V_1} - 1 \right) \quad (2.8)$$

Some work has been undertaken by Saguy and Rittel [91–93] looking at primary empirical methods of unifying the thick and thin skin equations. They show data to support that with the addition of two functions eq. (2.9) and eq. (2.10) that attempt to take account of corner effects. They have shown that this can retain the accuracy in the thin skin regime and much improve the measurement in the thick skin range. They have also published work on their measurement of 'bottom surface cracks' these are features that are on the opposite side of the plate to where the current is input and the measurements are taken [93]. It has been shown that at small skin depths the feature is not seen as the measurement is dominated by the current travelling on the top surface, however once the skin becomes sufficiently large measurements of the bottom surface cracks can be made, this limit has been shown to be when  $\frac{\delta}{t-d} > 0.5$ . This onset point has been used to characterise the depth of bottom surface cracks, using eq. (2.11) and the knowledge of the thickness of the plate and the skin depth of the current the depth of the crack has been measured successfully [92].

$$f_1(\Delta, \delta) = \Delta \exp \left( -\frac{\Delta/2 + \delta}{\delta} \right) \quad (2.9)$$

$$f_2(d, \delta) = 2d \exp \left( -\frac{d + \delta}{\delta} \right) \quad (2.10)$$

$$\frac{\delta}{t-d} = 0.5 \quad (2.11)$$

## 2.6 Summary

This review has covered a range of relevant subjects supporting this work. The aim of this work is to better understand and measure crack growth, this can then allow better understanding of fatigue life and inform finite life estimations. In this review, fatigue has been introduced and the reliance in modern life outlined from the early days of locomotive transport to more recently, and more closely linked to this work, the fatigue crack growth in high temperature steel and nickel based materials. Understanding crack growth in these high temperature materials is of high value, both from a safety and cost standpoint, and better understanding of this could lead to more realistic approximations of the life of jet engines as well as ground based power plant. If this is achieved the financial and safety benefits would be significant, allowing extension of life to some components and in other cases decommissioning or remedial works to prevent failure. This would increase productivity, reduce cost, maximise profit alongside the very important safety matters.

In this work the crack and feature measurement has been undertaken using both beach marking and ACPD method, previous development in these techniques and other relevant techniques have been outlined. In particular the use of variable frequency thus variable skin depth is relevant in this case. The ACFM that has been implemented in some work detailed in this review, this has relevance although it is significantly different to this study. This is a mapping technique for periodic inspection whereas the techniques developed here are for continuous measurement of cracks and their development in real time using a single point measurement.

DSA has also been reviewed, this has manifested itself in some of the crack growth rate testing seen in this work, on SS316. This is materials, temperature and strain rate dependant so has only been seen in some of the tests presented here.

## 3. METHODOLOGY

This thesis is centred on the measurement of non-uniform cracks that are generated in laboratory tests. In this chapter details of the development work on the TMF rig to include the use of fixed frequency ACPD, a novel beach marking technique to mark fracture surfaces in a predictable and repeatable fashion to record crack shape and of an advanced ACPD to be able to monitor crack shape are given. The development of the TMF rig covers the incorporation of a commercial ACPD system with a view that this can be upgraded to the advanced ACPD system, in due course.

### *3.1 Thermomechanical Fatigue Rig Development*

This section covers the developments made to the existing TMF rig at the University of Nottingham, this includes the work to interrogate the fixed frequency ACPD system and the other modifications made to the rig to accommodate this while ensuring that the system is still able to operate to the correct standards [21, 94, 95]. This has been undertaken to enable us to test materials in conditions that are representative of real world scenarios. In these conditions cracks form in the parts and the development made here enables not just the loading, both thermally and mechanically that drive this behaviour, but also includes the incorporation of an ACPD crack measurement system.

#### *3.1.1 Temperature Control*

Typically hollow specimens are used for TMF testing allowing the use of cooling air, passed axially through the centre of the sample fig. 3.1. This specimen geometry would not be suitable for crack growth testing as there

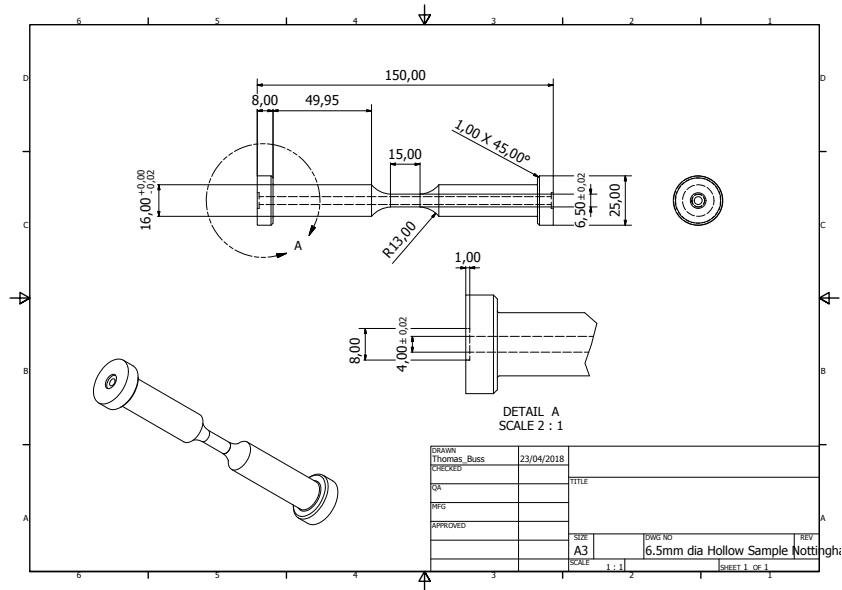


Fig. 3.1: Standard TMF Specimen

is very little material in this specimen for a crack to grow into, also the cracks will be slow to form and occur randomly in the gauge length. The most relevant standard sample considering limitations of the gripping on the Instron 8862 machine which was to be used for this work was the corner crack geometry. This is a solid square cross-section sample which has a small starter notch machined into one corner at the centre of the gauge section, this controls the start point of the crack by introducing a stress raiser and the sample being solid gives a good amount of material for the crack to grow through fig. 3.2. The industrial sponsor of this project typically uses 7mm by 7mm square cross-section corner crack specimens, given the expected loads for crack growth work and gripping capacity currently available on the machine this geometry could be accommodated, although the induction coil and air cooling would need to be modified.

It was realised that the induction coil would need to be of larger diameter than the standard equipment used on the rig, in order to accommodate the additional wires required for the measurement of voltages on the sample, the function of these wires is described later. A coil was manufactured and installed in the testing machine. The heating was calibrated by instrument-

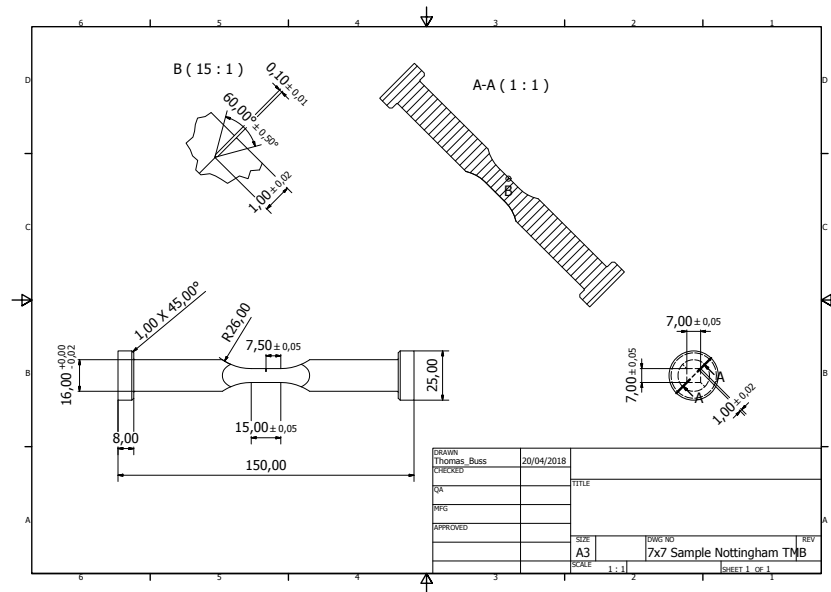


Fig. 3.2: Crack Growth Rate TMF Specimen

ing specimen with five thermocouples on the parallel section of the sample spaced equidistant along the axis. These were distributed on all four faces and one at a corner between two faces to get an understanding of the temperature distributions on the sample. The locations of the thermocouples are detailed in fig. 3.3. Thermal control was achieved within a  $\pm 2^\circ\text{C}$  tolerance, as the typical uncertainty on thermocouples is  $\pm 1.5^\circ\text{C}$  the total error remains within the accepted tolerance of  $\pm 5^\circ\text{C}$  in the TMF standard BS ISO 12111:2011 [95]. This standard describes the tolerances on all the systems and tolerances between them. This ensures that the intended mechanical and thermal waveforms are accurate in themselves and in relation to each other.

The heating/cooling system was developed in a multi-stage process. First a coil was fabricated, this was based on the wealth of experience gained at the University of Nottingham working on a range of materials. As the grips on the testing machine use hydraulic clamping, they require cooling to protect the seals in the hydraulic system from heat transferred from the sample. This is achieved by passing chilled water through channels within the grips close to the front face. This however has the effect of acting as a large heat sink

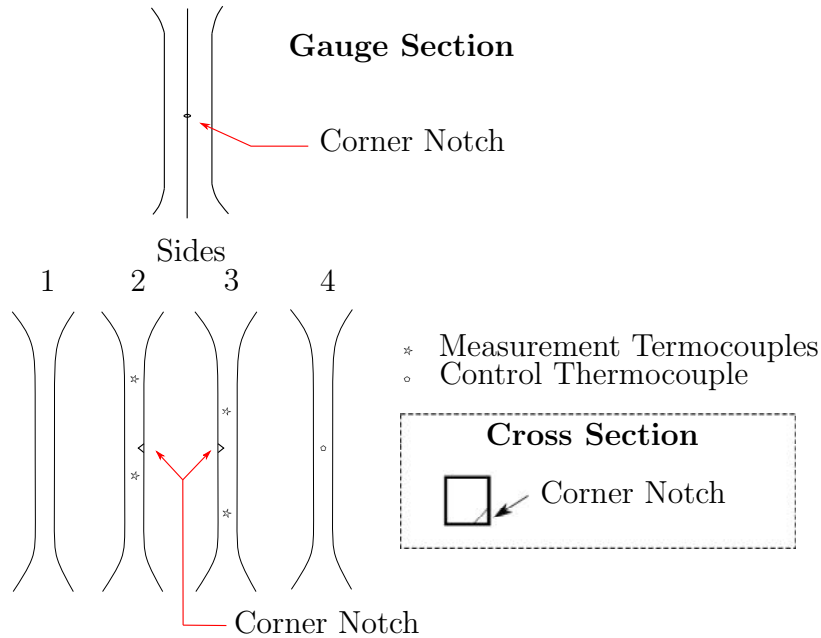


Fig. 3.3: Thermocouple Positions

at either end of the specimen, coupled with the larger thermal mass of the end gripping sections, has a strong influence on the temperature gradient in the specimen. To overcome this it is necessary to put a disproportional amount of heating into the shoulder of the specimen in order to shield the gauge section of the specimen from this heat sink. To do this, the coil was designed with three tightly wound coils at each end and one gently looping coil around the gauge section as shown in fig. 3.4. The tightly wound coils results in greater flux density in this region and so puts more power in to the end of the gauge section and the shoulder regions. As the two groups of coils are both wound in the same direction there is also coupling between them which, along with the looping coil, heats the gauge section. A new mandrel was manufactured to allow a length of copper tube to be coiled into the desired diameter. Balancing the spacing of the tightly wound coils to adjust the power gradient in the ends of the coil and therefore the specimen, and the spacing between the two sets of tightly wound coils can control the

---

power to the gauge section. The spacing of the coils is done on the mandrel by measuring the distances between the turns, by a combination of steel rules and marks on the mandrel. Once set, the coil is tested on the rig and the gradients monitored, the position of the coil and the turn spacing is then adjusted to improve the performance in an iterative process. During this process the control gains proportional, integral and derivative (PID) were also optimised to give a stable power output. The PID settings need to be adjusted to take account of the coupling of the sample to the electromagnetic (EM) field generated by the induction furnace, this is dependant on the properties of the sample material and the geometry of the coil and sample. As both the sample geometry and the coil have been modified, the PID settings needed some optimisation. This is done by injecting a perturbation into the set point and monitoring the control of the system. This can be done automatically by the temperature controller, although this has been seen to lead to a potentially unstable setting. This has been attributed to the PID tuning software in the controller giving the most responsive settings, if the systems changes this may lead to an over response. Again due to technical experience on this system, this is normally achieved in manual mode. The system is heated at a constant temperature rate to a specified set point and during this heating and hold, the power output and temperature is monitored by the technician and the PID are adjusted to give a smooth heating and hold with minimal overshoot and ripple on either the heating or hold sections. Initially the steady state temperatures at the planned, minimum, mean and maximum of the testing program is checked and verified. Once close control is achieved at these points a thermal waveform is run, representative of the fastest waveform in the test program, as this will be the most challenging for the system. The PID are set for this, also slower waveforms are also tested to ensure that the performance is robust and will be repeatable across the range of the parameters in the test program. Some data from a typical thermal calibration cycle can be found in fig. 3.5. The image in fig. 3.4 shows a completed induction coil and thermal calibration specimen.

Typically accelerated cooling has been achieved by using a hollow specimen. A 3mm hole is be bored down the axis of the specimen, resulting in the

---

gauge section being a thin walled tube with a wall thickness of 1.5mm. There is a hole through both top and bottom grips through which compressed air can be supplied. The degree of cooling can be controlled by utilising the second (cooling) output on the temperature controller and an electronic proportional regulator. This controls the air pressure supplied to the cooling channel and therefore the flow rate of the air through the sample. This allows closed loop control on the cooling of the specimen. As the samples in the case of crack growth testing need to be solid the hollow specimen approach could not be used. Therefore an external air cooling system was designed. This incorporated three nozzles which supply a smooth jet of air, the flow rate from these can be adjusted independently to give different flow rates. These were mounted on the test machine with some articulated arms and the cooling air was rerouted to supply these nozzles instead of the grips. It is most important to have a uniform cooling effect from these nozzles on all sides of the specimen. In order to achieve this, the sample was held at constant temperature and a constant air pressure was applied to the cooling jets. The nozzles were then adjusted, both in position and flow, to give a uniform cooling effect, see fig. 3.6. Once this was achieved in this static mode, the closed loop control was re-enabled and some cyclic heating and cooling tests were carried out. This system was then tested to ensure the specimen gauge length remained within  $\pm 5^\circ\text{C}$  during dynamic heating and cooling cycles.

### 3.1.2 Notches and Pre-cracking

A machined notch was used to initiate the crack at the centre point of the gauge section. During the pre-cracking the crack length was measured on the surface of the specimen using a travelling microscope. To get a stable image the cycling was stopped and the sample held at maximum load, holding the crack open, while the measurement was made. To initiate the crack a high load was used, once the crack was started the pre-cracking was continued at a reduced load level to approximately 2mm total length, with the load reduced to ensure that the final stress intensity was less than at the start of the test. This was done to ensure that the crack would grow in the test condition and to



*Fig. 3.4:* Induction Coil and Thermal Calibration Specimen

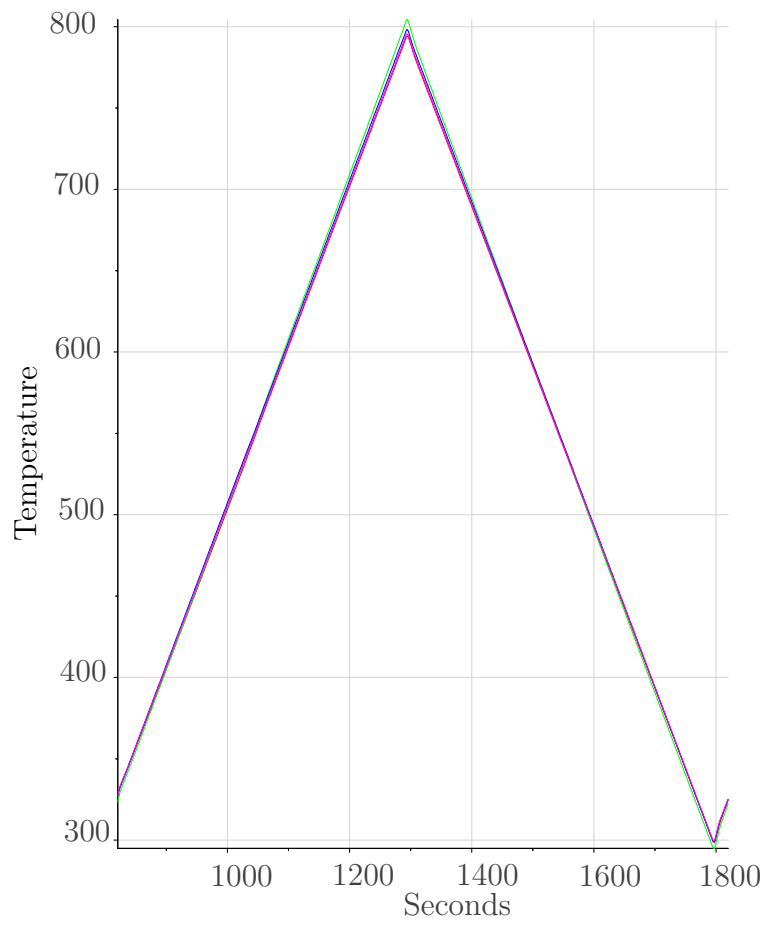


Fig. 3.5: Typical Thermal Calibration Cycle

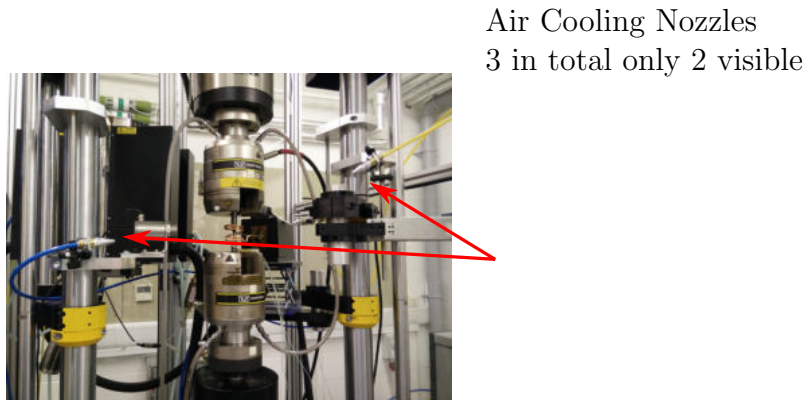


Fig. 3.6: External Cooling Arrangement

conform with the Rolls Royce Materials Mechanical Methods document [96].

For the SS316 the machined notch was 1mm deep, pre-cracking was started at 14kN which results in a stress close to yield. This however did not initiate a crack, therefore the notches were machined to a depth of 1.5mm. In RR1000 a much smaller notch could be used, only 0.25mm deep, due to this material being much more sensitive to notches. However the pre-cracking was initiated at much higher load of 44kN and due to a greater yield stress for this material.

The pre-cracking was all performed using an Instron 1341 servo-hydraulic testing machine running a Rubicon controller. This was at a rate that the machine could achieve without undue vibration, 20Hz for SS316 and 5Hz for RR1000. The rate was reduced for the RR1000 as the load required was near the load capacity of the machine, therefore the elastic deformation in the load string and test frame was significant.

### 3.1.3 Crack Growth Measurement

When considering the options for a PD system to install on the rig, both DCPD and ACPD were considered. Due to modern electronics both DC and AC systems can achieve high accuracy and resolution so the debate mainly focused on the interaction between the crack growth system and other elements of the rig. DCPD is extensively used by industry and academic institutions working in this field, DCPD is more straightforward; as there is no interaction between the crack measurement current and the current induced by the induction furnace. However there can be an interaction with DC systems, the main one of interest within this work being the thermocouple used for temperature control. The induction furnace on the system has its main power output at frequencies greater than 150kHz and therefore it was thought that the signals from the induction could be eliminated with a low pass filter.

A Matelect CGM-7 unit with two filtered pre-amplifiers, which had a low pass filter with a cut-off frequency of 10kHz was used, and this was expected to have separated the ACPD and induction furnace signals. The filters were very effective and removed the main power frequencies from the induction furnace. However, whenever the furnace was switched on, the ACPD measurement system went into saturation. It was discovered that there were other lower frequencies being emitted by the furnace, which in comparison to the power signals from the furnace were very small, only resulting in a few millivolts on the sample. However, this is very significant as the maximum signal that would be present in the ACPD system would be 4mV. These spurious signals were examined and shown to be present at frequencies down to around 3 to 5kHz, so were not being filtered out by the pre-amplifier filters. Working with Matelect the pre-amplifiers were modified to reduce the cut-off frequency to 500Hz. This successfully eliminated all the signals from the furnace, although it also reduced the maximum working frequency to around 100Hz due to the roll-off of the filter. At 100Hz the skin depth in SS316 is 10.7mm, larger than the cross section of these samples, therefore it is not possible to utilise the benefits of the skin effect.

---

The CGM-7 unit is a stand-alone unit which supplies AC at a user defined frequency to the samples, it also has two voltage measurement inputs with selectable gains. The second measurement can be used as a reference to eliminate fluctuations in the measurement which may arise from changes in the voltage readings from such things as temperature fluctuations. Therefore this is a complete system to measure crack growth, however this needed to be incorporated into the TMF testing system so that the crack length could be recorded alongside the other variables, such as the force and temperature. The  $0^\circ$  and  $90^\circ$  (sine and cosine) signals relative to the input current wave are both available on each of the voltage measurement channels, and these can be output as a DC voltages that are proportional to the measured value. These can be used individually, if the voltage is in phase with the current, or they can be used to calculate the overall magnitude and phase of the voltage signal with reference to the input current signal. This is often the case at higher frequencies where the inductive effects move the voltage out of phase with the input current. In this work the  $0^\circ$  signal was the most prominent at this low frequency as there is little phase shift so this was taken into the Instron 8800 controller. Two channels can be measured on the CGM-7, one being the voltage over the crack and the other typically a voltage measured in a region of uniform current flow away from the crack. The purpose of the second measurement at a point away from the crack (the reference pair), is to take account of any uncontrolled change during the test that may result in variation of the baseline voltage. It is important that the second voltage is measured between two points in a region of uniform current flow and with the same separation as the primary measurement, so that the magnitude of the change on the reference will be the same as that on the primary. These two signals were taken into the 8801 controller through two available analogue inputs and recorded.

In DCPD, the relationship between the crack length and the DCPD reading is straightforward being only due to the area of the remaining ligament (A) and therefore being explained by the normal resistivity equation (eq. (2.4)). In ACPD at high frequencies the relationship can be considered only to be linked to the path length (l), as the current only travels in a

---

thin skin near the surface of the metal the effective area through which the current is passing is constant, however the path length will increase as the crack grows as the current travels around the crack next to the new surface created. A schematic representation of this can be seen in fig. 2.10. There is some evidence in the literature that the relationship between the potential drop and crack length may not be linear [97,98]. To investigate this a series of experiments were carried out to understand the relationship between the voltage measured by the ACPD system and crack length within the frequency range of interest.

The first experiment was conducted on a high rate 1341 Instron testing machine with loading frequency of 20Hz and an R-ratio of 0.1. The maximum load for the testing was reduced during the test to enable time to take sufficient measurement. The initial maximum load was 14kN and this was reduced in stages finally reaching 7.5kN by the end of the test, the load decreases and final loads were decided during the test based on judgement and ensuring that the crack was growing at a reasonable rate that allows the operator time to review progress. This test was conducted at ambient temperature without any filtering of the input voltage signal. Supply current and frequency remained the same during the test set to 1A at 10kHz. The side of the sample was marked with scribed lines to enable the measurement of the crack length during the test. This was recorded for comparison with the ACPD readings. This data from this can be seen in fig. 3.7. This shows that in this experimental set-up the linear relationship does hold true. It is suspected that this is due to the significant starter notch that is present. In previous publications [97–99] non-linearity is shown to be present in the early stages of crack growth once the crack is past a certain length the response can be considered to be linear.

Further work was needed to confirm this relationship with a filtered signal and at elevated temperature. Also, it was clear that measuring the crack length optically on the surface of the sample was not ideal, as this relied on the operator taking measurements and the crack progression could be retarded at the surface. Previous experience had shown that beach marks could be generated in an isothermal fatigue test at 600°C by using a hold

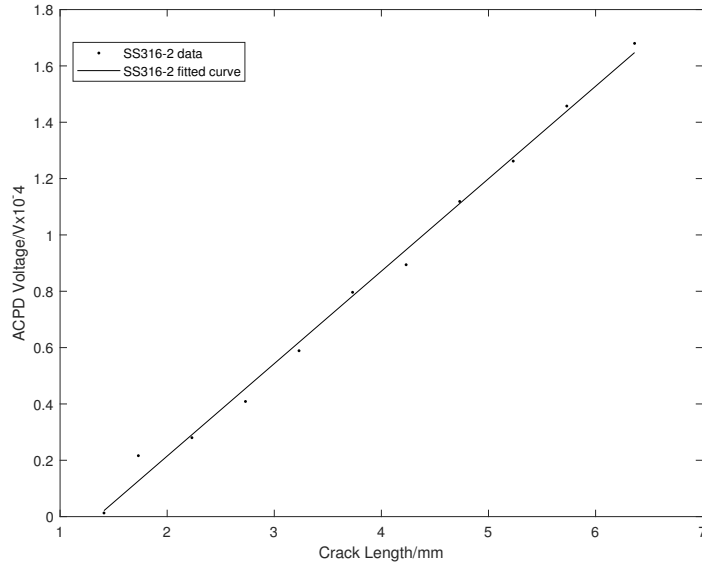


Fig. 3.7: Ambient Temperature Linearity Test

period at mean load. Therefore an isothermal fatigue test at 600°C was undertaken; using ACPD and a travelling microscope to measure crack length, also including number of beach marks to enable accurate measurement after the test. An image of the fracture surface showing the beach marks can be seen in fig. 3.8 and the plot of the data from the travelling microscope and beach marks can be seen in fig. 3.9. It can be seen that there is a clear linear relationship between the ACPD measurement and both the travelling microscope reading and the beach mark measurements, although it should be noted that there is a static offset between the two sets of data. It is thought that this is due to the crack not growing in a truly quarter circular fashion, the crack at the surface is consistently lagging the rest of the crack front (tunnelling) resulting in the travelling microscope consistently reading a short crack length when compared to the beach mark equivalent.

#### 3.1.4 Calculations of Crack Growth Rates

Throughout this work on SS316 and RR1000 alloys the Matelect CGM-7 was used to monitor the crack length. An AC current of 2A was passed through

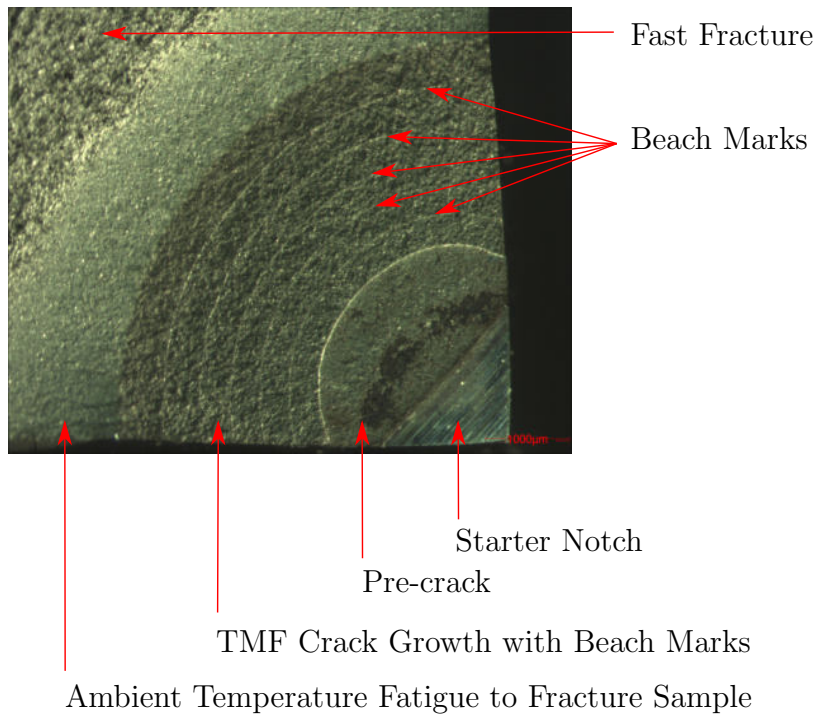


Fig. 3.8: Creep Hold Beach Marks

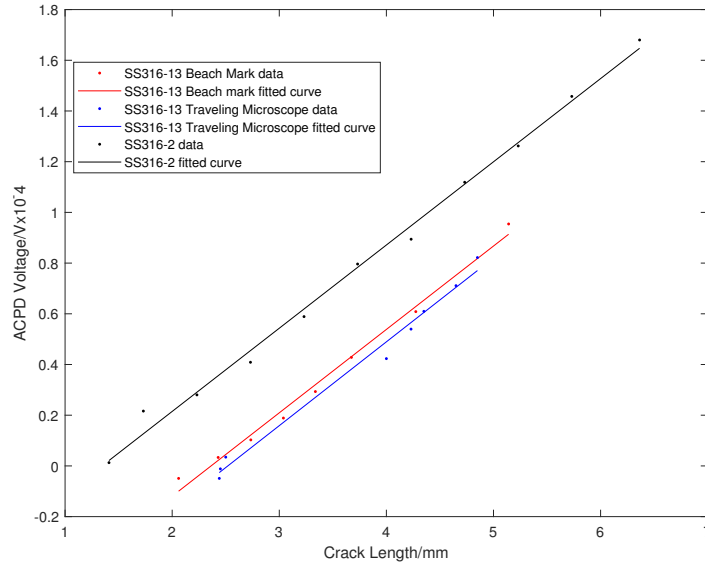


Fig. 3.9: Elevated Temperature Linearity Test 600°C

the sample at 107Hz the voltage across the crack was monitored using the CGM-7 and recorded along side all the other measurements on the TMF testing machine. Amplification was used on the CGM-7 to boost the voltage signal, this was set to ten thousand for all this work.

Post test the fracture surfaces were examined and images taken on a Nikon SMZ1000 stereo-microscope with Euromex DC 1300 digital camera system. The camera and microscope system had been calibrated at all available magnifications by University of Nottingham technical staff. For all the samples the magnification was set to give a good field of view to image the whole fracture surface with sufficient resolution to measure the start and end crack lengths. At this magnification the scale is 255 pixels per millimetre, giving a digital resolution of  $3.9\mu\text{m}$ . Given that typical crack lengths are between two and six millimetres ( $2000\text{-}6000\mu\text{m}$ ) this equates to between one 500th and 1500th of the measurement range, which is a satisfactory resolution. These measurements of initial and final crack lengths were related to the initial and final voltage values, given that the voltage response has been shown to be linear in relation to crack length this allows a linear calibration

value to be calculated for each test. The recorded voltage signals were then converted into crack lengths using these calibrations.

### *Paris Law Method*

The crack growth rates were calculated following methods developed by Paris and Erdogan, commonly referred to as the Paris Law. This relates to steady state crack growth, the incremental crack growth  $\frac{da}{dN}$  to the stress intensity range  $\Delta K$ . The relationship between these can be seen in eq. (3.1). If logarithms are taken of both sides (eq. (3.2)) of this equation a linear relationship can be seen in the middle portion of the curve. This linear section is often referred to as the Paris Region.

$$\frac{da}{dN} = C\Delta K^m \quad (3.1)$$

$$\log \frac{da}{dN} = m \log \Delta K + c \quad (3.2)$$

A typical plot can be seen in fig. 3.10, the Paris Laws can be seen in the centre of this plot. In this analysis the crack growth rate can be broken down into only two factors, the intercept ( $c$ ) on the  $y$  axis and the gradient ( $m$ ).

The length of the crack can be measured using the ACPD system and this is recorded for each cycles, using this the  $\log \frac{da}{dN}$  can be calculated. It is also necessary to calculate the stress intensity factor, for this the geometry of the sample and crack needs to be considered. To calculate this Murakami's Stress Intensity Handbook [100] was referred to. In these calculations the crack was considered to be quarter circular and equiaxed and the sample dimensions to be known (7x7mm). In this corner crack geometry the main equation as shown in the handbook can be seen in eq. (3.3).

$$K = \frac{\sigma\sqrt{\pi b}}{E(k)} F_c \left( \frac{b}{a}, \frac{b}{t}, \theta \right) \quad (3.3)$$

In this work many of these factors can be considered constants as the crack is considered to be a perfect quarter circular corner crack eqs. (3.4) to (3.9).

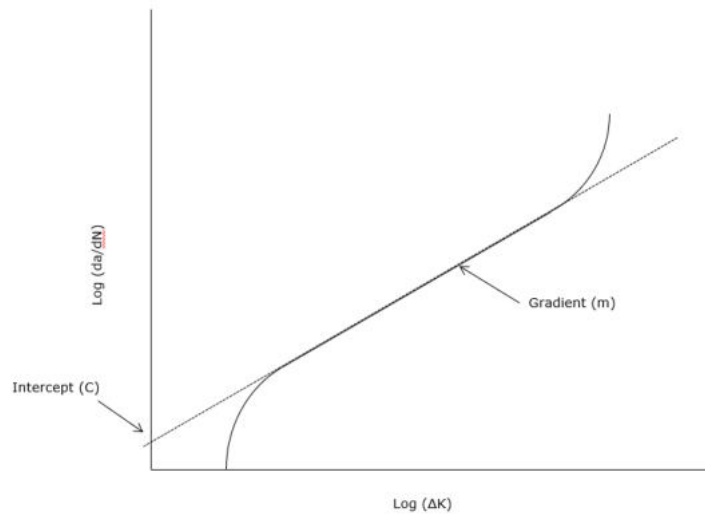


Fig. 3.10: Schematic Representation of a typical crack growth rate plot

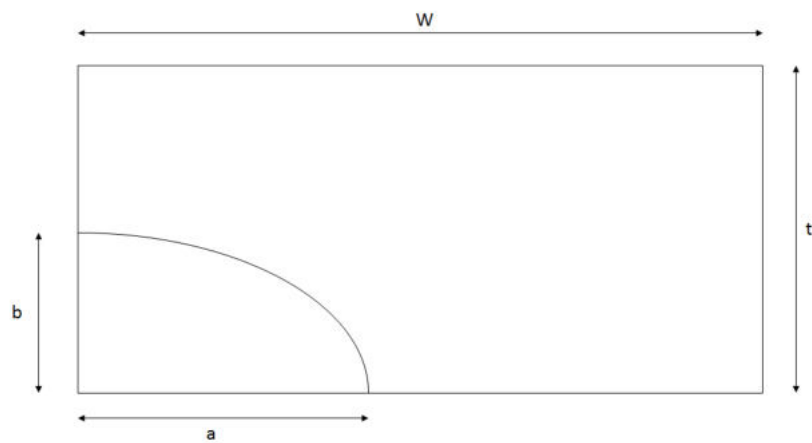


Fig. 3.11: Schematic Representation of the cross section of corner crack

$$E(k) \approx 1 + 1.464 \left( \frac{b}{a} \right)^{1.65} = 1.5697 \quad (3.4)$$

$$F_c = \left( M_1 + M_2 \left( \frac{b}{t} \right)^2 + M_3 \left( \frac{b}{t} \right)^4 \right) g_1 g_2 f_\Phi \quad (3.5)$$

$$M_1 = 1.08 - 0.03 \left( \frac{b}{a} \right) = 1.0500 \quad (3.6)$$

$$M_2 = -0.44 + \frac{1.06}{0.3 + \left( \frac{b}{a} \right)} = 0.3754 \quad (3.7)$$

$$M_3 = -0.5 + 0.25 \left( \frac{b}{a} \right) + 14.8 \left( 1 - \frac{b}{a} \right)^{15} = -0.25 \quad (3.8)$$

$$f_\Phi = \left( \left( \frac{b}{a} \right)^2 \cos^2 \theta + \sin^2 \theta \right)^{\frac{1}{4}} = 1 \quad (3.9)$$

Some do not reduce to constants as they relate to the current crack length and therefore need to be calculated for each increment.

$$g_1 = 1 + \left( 0.08 + 0.4 \left( \frac{b}{t} \right)^2 \right) (1 - \sin \theta)^3 \quad (3.10)$$

$$g_2 = 1 + \left( 0.08 + 0.15 \left( \frac{b}{t} \right)^2 \right) (1 - \cos \theta)^3 \quad (3.11)$$

A Matlab function was written to deal with this as shown in appendix A.4. The function requires the maximum load in the fatigue waveform, the R-ratio of the loading and the crack length at the maximum load in each loading cycle. In the process, data for crack lengths greater than 0.6 of the width of the sample were discarded, this follows the guidelines set out by Rolls Royce in the relevant Materials and Mechanical Methods document [96]. This should be done as the stress intensity factors cannot be relied upon in the range over 0.6 of the sample width. The data is then used to calculate the minimum and maximum stress in each cycle and therefore the minimum

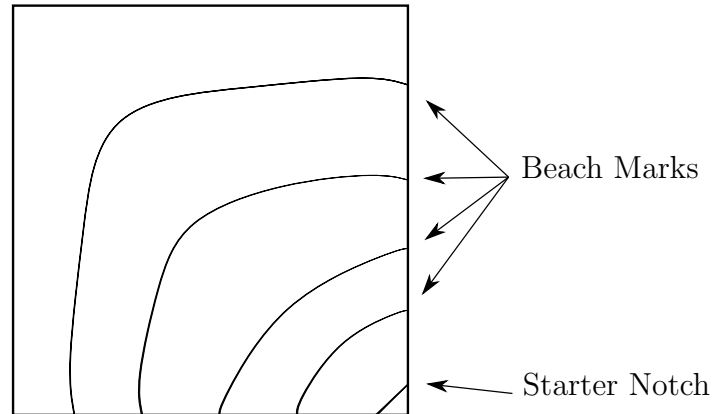


Fig. 3.12: Schematic Representation of Beach Marking

and maximum  $K$  values, giving  $\Delta K$ . The cycle number and crack length are used to calculate  $da/dN$ , due to the fundamental noise on this data it cannot be differentiated directly. To get a unidirectional smooth data set an exponential function is fitted to this curve and this can then be differentiated. Once this data has been processed logarithms of both can be taken and the data plotted.

### 3.2 Beach Marking

Beach marks have been used to characterise the size and shape of cracks in real world components and during laboratory tests [38, 79, 80, 101–103]. The loading experienced by components in the field is rarely simple and repeatable, the loading may change due to things such as plant startup and shutdown or may change as the load is redistributed as multiple cracks grown in the part. These changes can lead to changes in the texture or small lines on the fracture surface which can be seen as beach marks. fig. 3.12 shows a schematic representation of a possible fracture surface based on a corner crack specimen, in this representation the crack starts quarter circular but at larger crack lengths tunnelling develops.

### 3.2.1 Loading Trials

The MAX software on the Instron TMF rig can be used to schedule sequential tests, this was used to undertake a range of experiments to investigate the effect of different loading regimes on the resulting fracture surface. In this a nominal fatigue test waveform was chosen and a range of other loading conditions were trialled with the intention of producing beach marks. A number of marking waveforms were tried on one test sample, the fatigue test waveform would be run for a period and then an alternative loading was used. The alternative loadings applied ranged from compressive loads, to hold periods and cyclic loading at different frequencies and R-ratios.

### 3.2.2 Fracture Mechanics Approach

In this work a robust method of generating marks was considered. Typically, as in the Loading Trials work shown above and in the literature [38, 81, 102, 104], the method to generate marks has been determined on a case-by-case basis based on experience. Given the knowledge of the instantaneous crack length the stress intensity factor can be calculated, and if the Paris coefficients are known for the test and beach mark waveforms it should be possible to plan the position and size of the beach marks. Tests were undertaken to gain the required information for both the test and beach mark waveform, these were then used to design a fracture surface based on the predicted crack length during the testing.

## 3.3 Alternating Current Potential Drop Technique

### 3.3.1 Bench Frequency Sweep Testing

The aim in this section of work was to undertake some initial tests on a number of specimens with machined features designed to simulate specifically shaped cracks. The existing Matelect equipment was used which can output frequencies from 10Hz to 300kHz although this does not have the capability to rapidly sweep through these frequencies.

Matelect have developed some LabView Virtual Instruments (VIs). These are small packages of computer code that can be used in the LabView programming language. These VIs enable communication between LabView and the Matelect CGM-7 unit, enabling control of all the available parameters and reading back of data. A short program was written to step through the frequencies from 100Hz to 250kHz in a logarithmic sweep and read the voltages back at each step. The CGM-7 unit takes a number of seconds to stabilise at each frequency, therefore this sweep took in the region of 45 minutes to complete. The LabView code can be seen in appendix A.1. The CGM-7 displays and outputs the sine and cosine components (indicated as the  $0^\circ$  and  $90^\circ$ ) of the measured voltage, which can be viewed on the front display of the instrument. There is also a DC signal which is proportional to this output from the back of the instrument alongside an RS232 9 pin D-sub port. In this work the RS232 digital communication was used to both instruct the instrument, thus performing the sweep, and also to read back the voltage, current and frequency at each step.

It was also noted that although the CGM-7 had the capability of outputting frequencies as low as 10Hz, there was some non-linearity in the pre-amplifiers below approximately 50Hz. To avoid this problem it was decided to only sample from 100Hz and above. This was acceptable in this instance as this work was only a proof of concept and once a method was developed new purpose built equipment would be sourced.

### 3.3.2 *Advanced Alternating Current Potential Drop Kit Development*

Following the work undertaken using the Matelect equipment it was decided to start sourcing equipment that was more suited to the planned work. There were two main problems with the Matelect unit, one was the lack of linearity in the frequency domain at low frequencies which is not a problem if the units are used in the normal fixed frequency mode as the response in relation to magnitude of the measured voltage does appear to be linear. The second is the inability to rapidly sweep through the frequency range, which is needed to enable the rapid measurement over a wide frequency range within a small

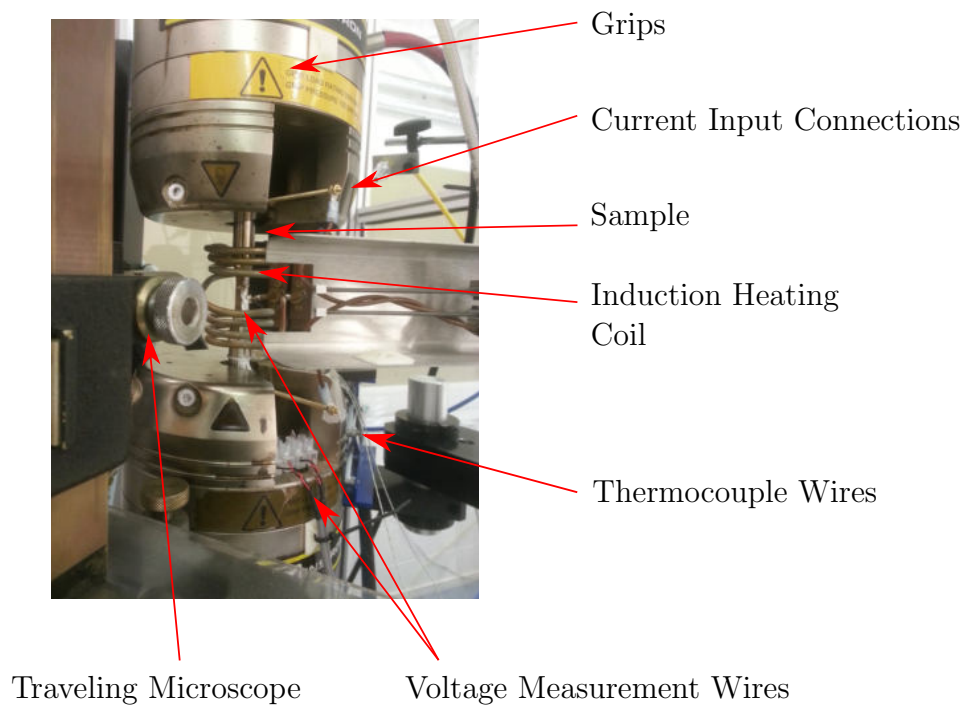


Fig. 3.13: TMF sample and clamping

---

portion of the LCF or TMF loading cycle. This is due to crack closure; if the crack is not fully open at the time of taking readings there may be other conductive paths between the crack surfaces which will affect the reading.

### *Electronics*

There were two main avenues to explore when sourcing this equipment, simple amplifiers with signal generation and logging of data being carried out on a computer or equipment providing a complete 'solution' as with the Matelect unit. A specification for the equipment was drawn up, considering the skin depth in a range of materials and lessons learnt in the Matelect work. Maximum current of 3A and frequency range 0-250kHz was specified, to give a higher current capability than the Matelect unit and to cover a relevant skin range in both ferromagnetic and non-ferromagnetic materials. Plots of the skin depth in a variety of materials can be seen in fig. 3.14, it was determined that the equipment should be able to run from a thick to thin skin condition. It can be seen from the plot that the effect of the magnetic properties on the skin depth is significant, the ferromagnetic Nickel and Iron having a much lower frequency at which the skin becomes thin. Given that samples are typically pre-cracked to more than 1mm, it was considered that a skin depth of 0.5mm would be sufficiently thin, therefore an upper frequency limit could be set at 250kHz. If the skin depth is half the diameter of the sample, it can be considered that the current is uniformly distributed throughout the cross-section of the sample, this can be considered a quasi-DC situation. For a 10mm diameter sample, it can be seen that this is at 0.1Hz in the nickel. This low frequency is virtually DC, therefore quasi-DC to 250kHz was determined as the frequency range. In the Matelect trials it was found that a current of 2A was sufficient to give a measurable voltage drop therefore this was also specified. On the measurement side, an amplifier was specified to match the frequency range of the input and a sensitivity sufficient based on the trials with the Matelect work.

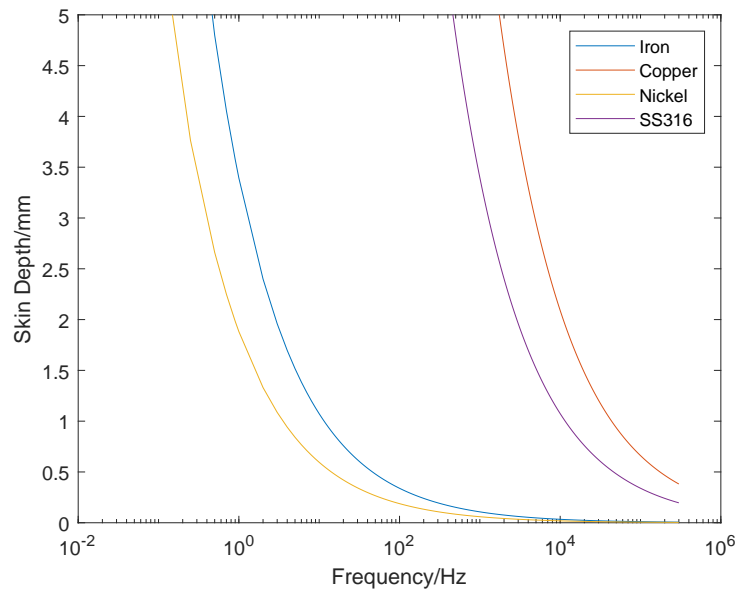


Fig. 3.14: Skin Depth for various materials

The specification of the equipment was:

- Current Supply System
  - Current controlled supply up to 2A
  - Frequency range of DC to 250kHz
  - Load resistance to be less than 1
  - Protected output, supply cuts output if there is an open circuit condition to protect the equipment
- Voltage Measurement System
  - Measurement range from 0 to 0.4 mV
  - Frequency range of DC to 250kHz
  - Options to install filters to eliminate signals from induction furnace

The search for a complete solution led to looking at galvanostats. These have the capability of undertaking a range of testing including injecting currents at various frequencies and sweeping frequencies and measuring normally two voltages. These are mainly used in electrochemical testing, in the study of such things as corrosion and battery performance. A supplier was found that could provide a unit with the current capacity that was desired, the Ivium Vertex was loaned from the company. This unit could supply up to 5 A at frequencies from 10  $\mu\text{Hz}$  to 1 MHz.

Experiments were undertaken on the featured samples to test the performance of this unit. In these experiments the proprietary software (IviumSoft) was used, which enabled frequency sweeping and simultaneous data capture. Initially this looked promising although further trials highlighted that there was little to no difference if the samples were connected or not. It was found that there were more spurious signals from connectors and other artefact than true signals from the samples. The decision was taken that this instrument did not have the sensitivity required in this work.

Alongside this work was sourcing some simple amplifiers. For this there were two elements, the supply and the measurement. The measurement is fairly straight forward; a wide band voltage amplifier would be required, these are available from a range of suppliers. The main challenge is the high current supply amplifier, this would need to drive current at very low voltages. This is due to the sample having a very low impedance. Typical amplifiers are designed to drive a current through a circuit that has an appreciable resistance, for example an audio amplifier would expect to be driving speakers which have a resistance of either 4 or 8  $\Omega$ .

Due to this lack of commercial demand, there are very few products available. A 7224 DC plus audio bandwidth AC signal source was borrowed from AE Techtron. This could run in both voltage or current control. The unit was not able to achieve stable current control; the voltage ramped up very quickly and the amplifier shut down. However it did manage to drive signals through the sample in the voltage control mode once the settings had be altered to move to a low resistance mode. The initial results were promising. A signal generator was used to input a range of signals from

quasi-DC to 250kHz and this worked as long as it was in the voltage mode. During this the amplifier would overheat and start to input some noise onto the signal and then shut-down. It was decided that this product would not be suitable as it was working at the very edge of its operating window on this very low impedance system.

Fylde Electronic Laboratories Ltd. were also contacted and they undertook to design a bespoke current amplifier. The Fylde FE-H379-TA was selected for the measurement amplifier due to its gain range and bandwidth capabilities. The FE-H379-TA has a user selectable gain up to 1000 times and switch-able low pass filters which can be used as needed. In the wide band mode the low pass filter is at 500kHz which is sufficient for the application and also works as an anti-alias filter ensuring that there are no high frequency elements reaching the data capture system. The input impedance on this unit is  $10M\Omega$  so there is virtually no current leakage though the measurement wires therefore the contact impedance at the measurement points can be considered to be zero.

It was also noted that when moving to measurements in the induction furnace some filtering would be required, however this would not be necessary in the bench experiments. A PXI unit with a PXIe-6124, was sourced from National Instruments. This could achieve up to 2.5M/sample/sec on two simultaneous outputs and 4M/samples/sec on four simultaneous input. This along with a MXI interface board and relevant chassis would provide a flexible platform, capable of outputting any waveform as required and reading signals back synchronously. On site trials were started to check the performance of the supply amplifier with the signals generated by the PXI unit. This testing was undertaken using a plain steel bar as the load and was intended to test the performance of the supply amplifier against the specifications from Fylde. During these trials a problem was identified on the signals, a small signal at 254kHz was seen superimposed over the input frequencies. A screen shot of this can be seen in fig. 3.15

This was isolated to the pulse width modulation used in the current input amplifier power supply. This signal was only present at lower output frequencies when the power required was changing. The signal was feeding

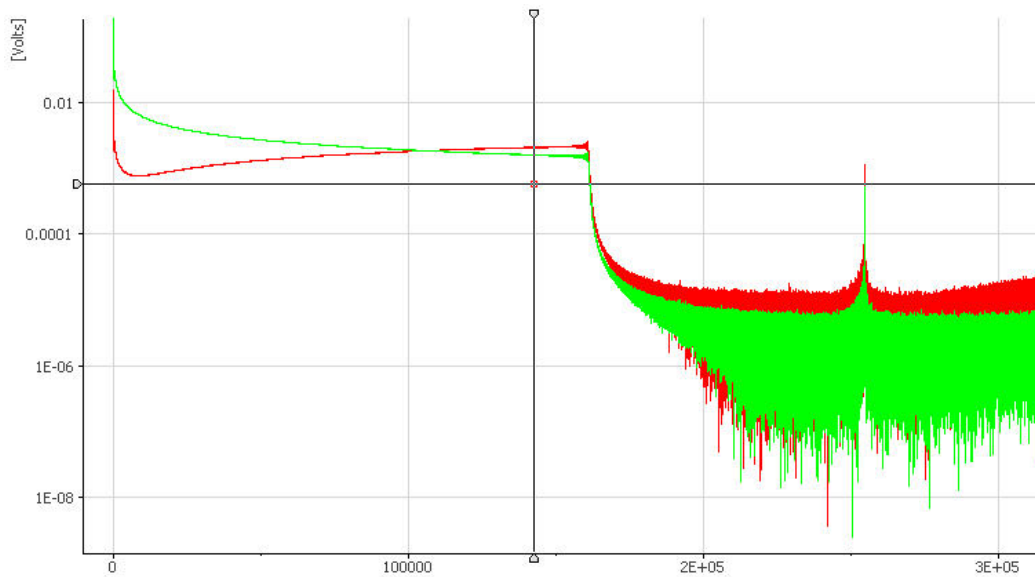


Fig. 3.15: FFT of the signals from Fylde trials showing noise at 254kHz

back through the earth line of the mains outlets in the lab. This was solved by removing the earth connection in the power supply, this is acceptable as the unit is double insulated there does not require an earth connection to ensure user safety. Once this was resolved the linearity of the power output was checked, this was found to be within the 2% tolerance up to 250kHz. However the amplifier was seen to perform to higher frequencies with some roll-off. This is expected due to the 700kHz low pass filters on the output. It was deemed that this amplifier was fit for purpose.

Code was written to generate two output signals and record up to four channels, this can be seen in appendix A.2. The output channels were a swept sine and swept cosine, the sine was used to drive the amplifier and the cosine would be used later to resolve the phase of the resulting signals. The recorded signals were as follows:

AI0 Sine output signal

AI1 Amplifier output current

AI2 Voltage over feature (from FE-H379-TA)

### AI3 Cosine signal

A data rate of 4M samples per second was used to get sufficient temporal resolution at high frequencies, at 250kHz this gives 16 points per cycle. As this code generates all the points in the output waveforms at once this quickly fills the RAM on the computer, thus only a short recording length can be achieved. This was rectified in some updated code, this addressed the data flow issue that was causing the RAM to become saturated. Also the recording was triggered such that the record starts at the start of the sweep, at zero degree phase on the sine output signal and finishes at the end of the sweep. This means that there is no excess data being recorded and that all the sweep is captured.

### *Experimental Setup*

It is known that AC currents passing through a circuit can induce voltages in conductive materials in the vicinity. In this case it is the current running through the samples and input leads that can induce a voltage in the wires used for measurement, these wires are shielded from the connector block to the measurement amplifier however there is a length which is unshielded. This is often referred to as pickup. To understand this an experiment was devised to simulate the loop of unshielded wire in the measurement wiring. To do this a loop of wire which did not connect with the samples was needed to eliminate the signal due to the potential drop. This needed to be of the same length, to encompass the same area and be in the place so as to have the same amount of pickup. To approximate this idealised situation a piece of two core thermocouple cable was used, this was chosen as the two conductors are not twisted running parallel in the outer sheath. At the centre of this length of wire the sheath was removed and one of the conductors cut and welded onto the sample, this would be for the measurement of the voltage on the sample and any pickup. The other conductor was left intact and looped round to follow the same path as the measurement, this was not allowed to contact the sample. This second conductor would therefore only measure the pickup. A schematic representation of this can be seen in fig. 3.16.

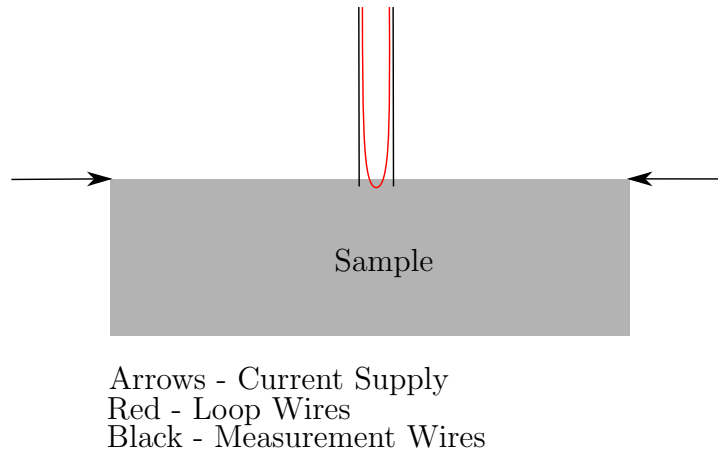


*Fig. 3.16:* Schematic of Loop Sample

The current sweep was run through the sample and the voltage readings were taken from both the measurement wires attached to the sample and from the separate loop wire. The FFT of these was taken and the magnitudes compared, a plot of these can be seen in fig. 3.17. It can be seen that there is a significant signal on the loop wire, which is a large proportion of the total signal at higher frequencies. This indicated that the pickup on the unshielded measurement loop was significant and this problem would need to be addressed.

Only solid single strand wire can be welded to the samples, so normal shielded instrument wire is not suitable for this. This results in the last portion of the measurement wire being unshielded, therefore some sort of a shield was needed to stop stray pickup from the magnetic fields generated by the AC current passing through the sample. It was also noted that when this is to be done in an elevated temperature environment the instrument wire would not be able to withstand the temperatures. Therefore a number of methods to eliminate the unshielded wire types from the EM field were needed. The two main methods considered were surrounding the wires with a material such as steel that can divert the flux around the area, providing

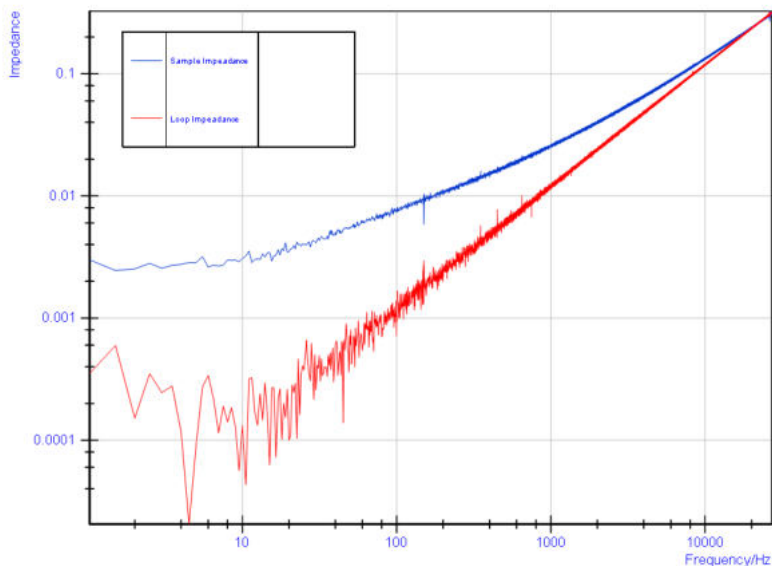
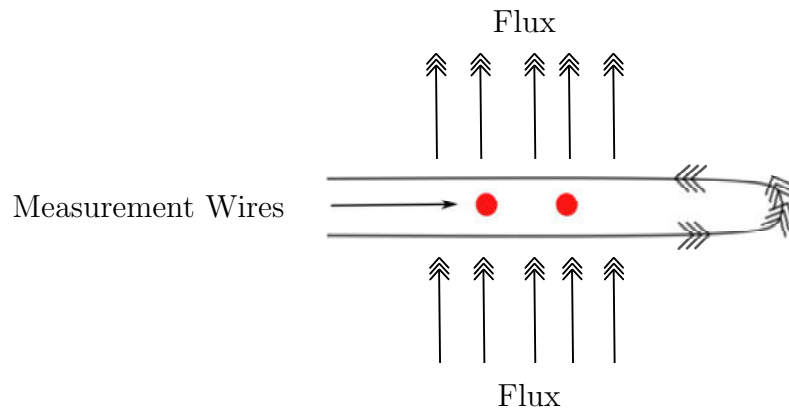


Fig. 3.17: Sample and Loop Signals

a 'bridge' (fig. 3.18), or to block (fig. 3.19) the flux by surrounding the wires with conductive material, the flux would induce a current in the conductive layer and not reach the wires.

To test the performance of these techniques a loop was set up as in fig. 3.16 and the voltage on this loop was measured as the current sweep was passed through the sample. Each of these methods reduced the pickup and when combined the pickup signal reduced significantly. It can be seen in fig. 3.20 that the pickup is significantly reduced as more protection is added, this is most evident at high frequencies where the EM pickup is most significant.

Another method was also tried; it is typical to shield electronics in conductive boxed. To do this, a die cast box was modified to enclose the connector block and sample connection wires. A small slot was cut in the back end of the box to allow the wire to the amplifier to exit, also a very small slot was cut in the leading edge of the box to allow the measurement wires to connect to the sample. These openings were kept to a minimum to prevent EM leakage into the box. The box was modified to allow it to rest on the side of the sample, minimising the length of the measurement wire protruding



*Fig. 3.18:* Schematic of Flux Bridging

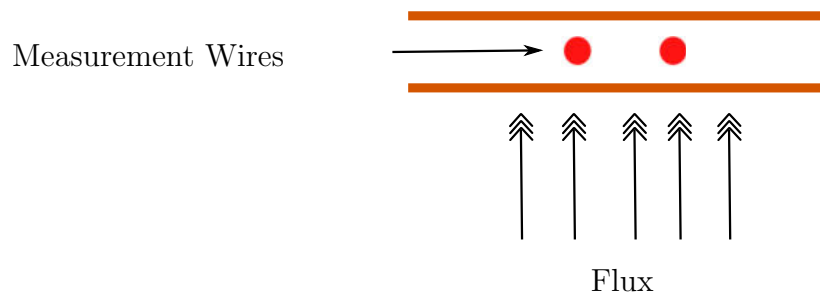


*Fig. 3.19:* Schematic of Flux Blocking

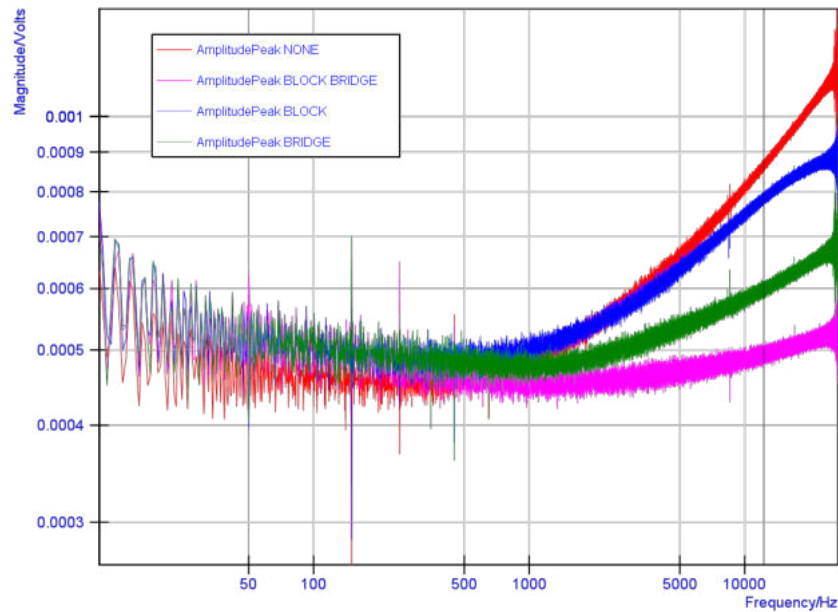


Fig. 3.20: Flux Bridge and Blocking test - Voltages measured on the loop wire

out of the box and the edge of the box was insulated with polymer tape to electrically isolate it from the sample. Images of the box open showing the connector block and wires and the closed box can be seen in fig. 3.21.



Fig. 3.21: Shielding Box

The resulting signal from the loop, as in the bridging and blocking experiments, was recorded as the current was passed through the sample. A

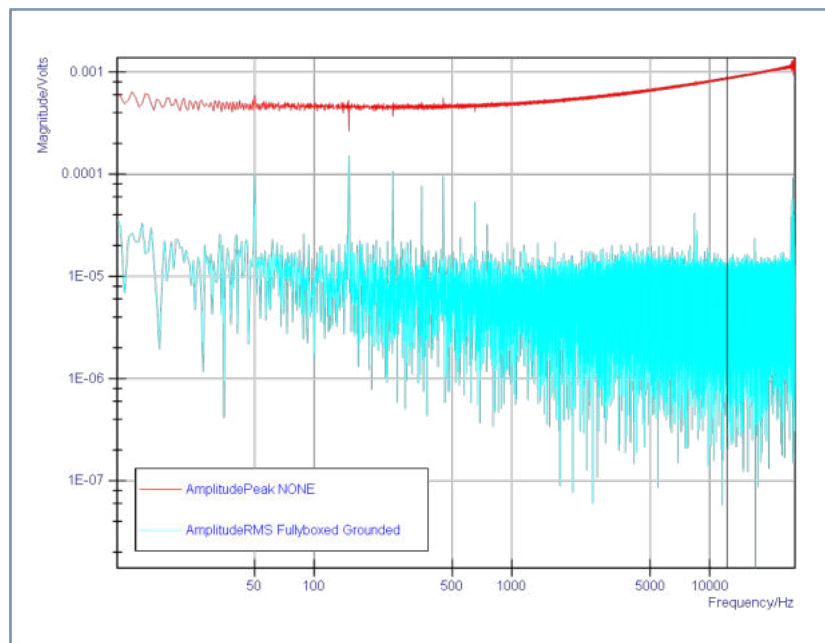


Fig. 3.22: Shielding Box test - Voltages measured on the loop wire

comparison between the unshielded and the box can be seen in fig. 3.22, the box reduced the pick up even lower than in both bridging and blocking combined. This may be due to the box completely surrounding the area, apart from the small amount required to make the connection to the sample. It is possible that if further efforts had been made to fabricate a full enclosure the bridging and blocking may have worked as well as the box. However the die cast box is a very good solution to the problem so the decision was taken to work with this. The box and polymer tape solution is only suitable for ambient temperature work, it is envisaged that this would need to be developed using a higher melting point metal for the box and possibly a glass insulator for high temperature applications. The glass layer would be used to both electrically and thermally insulate the box from the heated sample. For the bench samples this die cast box works well to ensure that the reading from the measurement points are unaffected by outside interference and pick-up from the input circuit.

Alongside this work to protect the measurement wires the input signal wires were considered. In the initial experiments some flexible copper cable

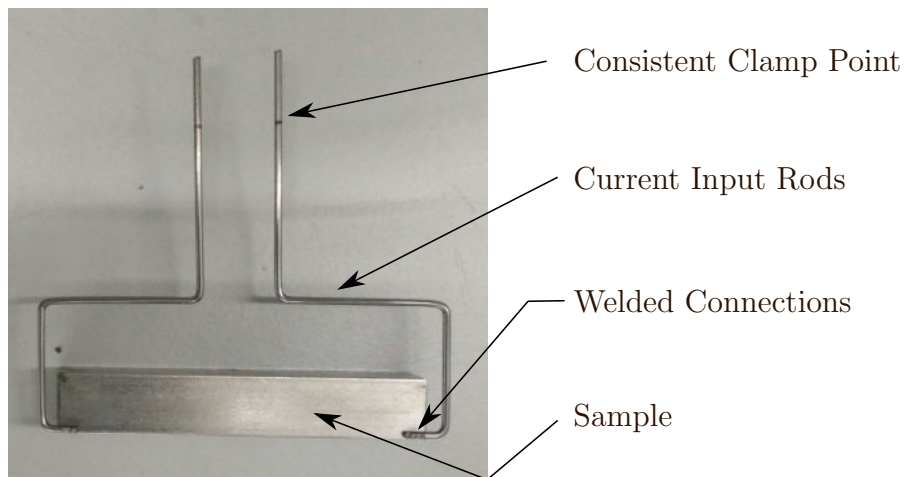


Fig. 3.23: Steel Current Supply Rods

was used to connect between the output lead from the current amplifier to the sample. There were two problems with this; the connections were weak solder joints prone to disconnecting and the wires could not be placed in the same position in each experiment. Experiments were undertaken using a spot welder to make a stronger connection on the samples, copper does not weld very satisfactorily to steel so steel rod was used. It was determined that 0.045 inch (1.14mm) steel rod welded successfully giving a sufficiently strong joint, also this gauge was sufficient to carry the required current without significant heating or causing a very high drive voltage due to the impedance of the material. As this material is stiff it could be bent into a predetermined shape thus controlling the relative position of the input wires and sample. This ensures that if there is any pick-up (although it is believed that this has been greatly diminished) this is repeatable from sample to sample. An example of the final set-up can be seen in fig. 3.23.

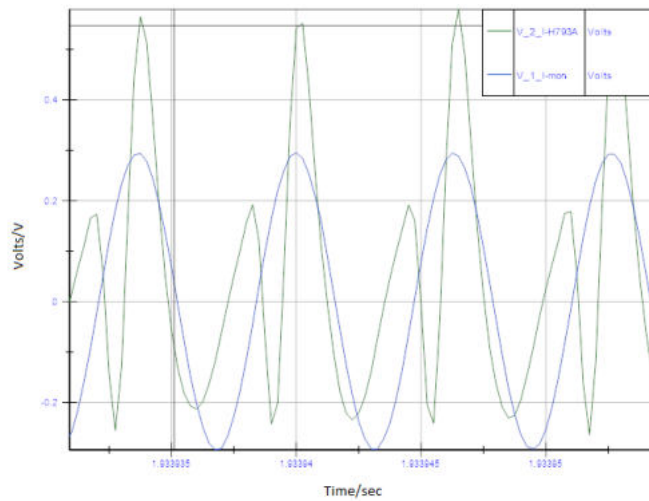


Fig. 3.24: Non-sinusoidal Voltages

### 3.3.3 Troubleshooting

In initial experiments some issues were identified in the measured voltages on the samples at higher frequencies. The voltages measured were not oscillating in a sinusoidal manner, fig. 3.24 shows the sinusoidal current input signal and the corresponding voltage measured on the sample. It can be seen that there is a 'double hump' type feature in each wave, it was not clear if this was a feature of the experiment or an artefact.

The work mentioned earlier in the Experimental Setup Section was revisited, as this could have been a shielding failure. A mu-metal shield was added and the experiments with shielding repeated, this did not affect the wave shape. This was tracked down to a common mode distortion. The FE-H379-TA is a differential amplifier, meaning that it amplifies only voltages measured between the two measurement wires and any other voltages are discarded. So if the voltage on the sample fluctuates with reference to ground this should be discarded, the fluctuation with reference to ground is termed the common mode voltage as this is the voltage which is common to both measurement wires. This enables small local voltages to be measured without being swamped by bulk variations, the limit of common mode rejection on the FE-H379-TA is 10V. The common mode problem was identified by con-

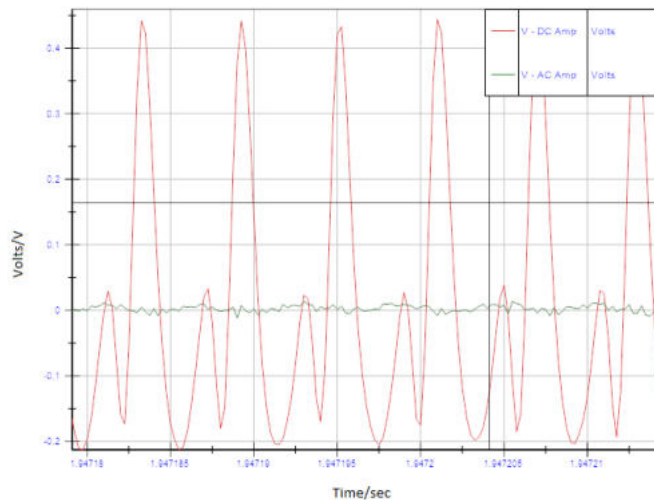


Fig. 3.25: Common Mode Distortion

necting the two measurement wires to the same point effectively 'shorted out' on the sample, in this case no voltage should be measured. This was tested and it was found that at high frequencies some signal was measured, this can be seen in fig. 3.25. To overcome this issue Fylde Electronics designed an amplifier with higher common mode rejection, to achieve this a different approach was used. The FE-H379-TA is a DC coupled amplifier so it is not freely floating with reference to ground, the new amplifier was AC coupled allowing it to float with the bulk voltage on the sample. It can be seen in fig. 3.25 the common mode is eliminated in the new amplifier. This removed the common mode distortion but this amplifier cannot measure frequencies below 500Hz without some distortion. Primarily the distortion manifests as a lag in the signals so this has an impact on the phase relationship, below this frequency a phase shift in relation to the current is seen. Below this frequency the FE-H379-TA would need to be used. The FE-H379-TA works well at low frequencies as the common mode voltage at the lower frequencies is below the maximum common mode rejection limit for the FE-H379-TA.

In practical terms it is not desirable to make two sets of measurement with two different measurement amplifiers, in fig. 3.14 it can be seen that there are two main groups of materials separated by the skin depth. For the SS316

---

and copper the transition from thick to thin skin happens at a frequency significantly above the 500Hz lower limit of the AC amplifier, therefore this can be used without any distortion. In Iron and Nickel this happened at much lower, and this distortion would be significant. However due to the lower drive voltage needed at lower frequencies the double hump features not seen when using the FE-H379-TA in the range of interest for these materials. Therefore the FE-H379-TA can be used for the Iron and Nickel and the AC amplifier can be used for the SS316 and Copper.

### 3.4 Data Analysis

The current injected into the samples is a continuously changing sweep in the frequency domain, this sweep approach ensures that there are no spurious higher frequency elements being injected at steps in the frequencies. If individual sine waves were used to give discrete frequencies there would be quick changes of gradient as the signal changes between the waves, these shifts in rate of change would appear in the high frequency elements in the signals. It is possible that this would be higher than the range of interest, however there would also be harmonics of these high frequencies that manifest in the range of interest.

Due to the swept input signal, the data obtained from the Advanced ACPD equipment is also a continuous sweep of voltage reading which are proportional to the current being passed through the sample and the voltage measured on the sample. These can then be converted into current and voltage readings by scaling the values based on the gain on the amplifiers. The data contains all the frequencies in the specified range, but the sweep is continuous so discrete frequencies cannot be identified. A manual approach could be taken, in this it is possible to measure an amplitude and phase for a nominal frequency but this only gives a coarse and approximate measurement in the frequency domain and is very time consuming, in this work an FFT was implemented using National Instruments data analysis program DIAdem.

This approach, using the FFT function should be verified by comparison with some manual data, as described above. The manual data approach as-

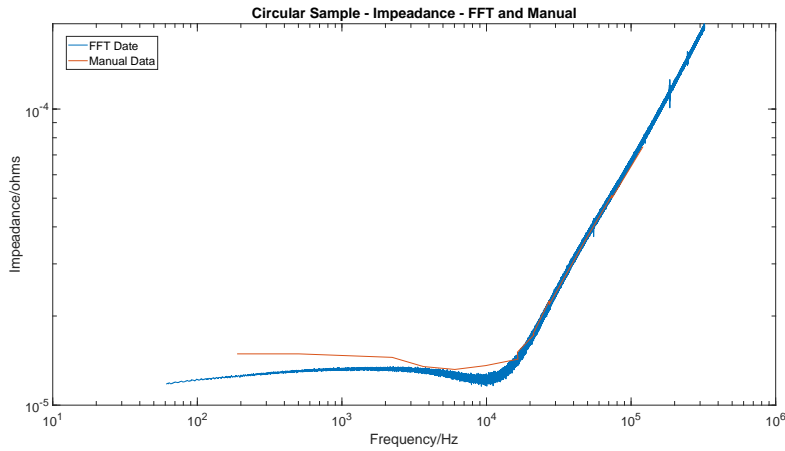


Fig. 3.26: FFT and Manual Data Processing - Impedance - Circular Sample

sumes that there are discrete frequencies, this is therefore an approximation but it was felt that this would give an indication of the impedance and phase relationships without relying on the FFT. Measurements of the raw amplitude of the signals and time shift between peaks in the waves were taken at a number of points through the sweep. The impedance was calculated using the amplitudes of the current and voltage signals and Ohms Law ( $V=IR$ ) From the time shift between the peaks of the two signals and nominal frequency the phase relationship was calculated. A comparison of the data from the FFT and the manual measurements for the circular sample can be seen in figs. 3.26 and 3.27

### 3.5 Discussion

In this methodology there have been three main pieces of work, implementation of ACPD on a test rig utilising induction heating, development of a novel and robust beach marking methodology and the manufacture and test of a variable frequency ACPD system.

The incorporation of the fixed frequency ACPD system onto the testing rig and the use of this during LCF and TMF was successful. Challenges around suitable filtering being the main area of interest, the work has shown that the two AC systems can work simultaneously but filtering out the signals

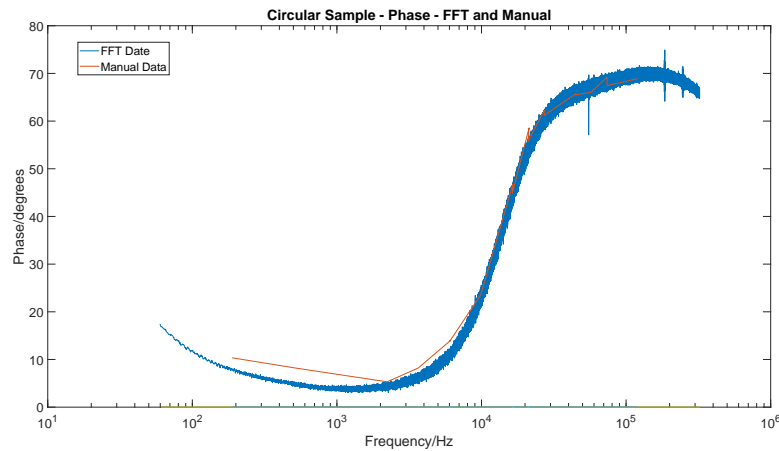


Fig. 3.27: FFT and Manual Data Processing - Phase - Circular Sample

from the induction furnace is paramount. In the fixed frequency mode this has been achieved by the use of an aggressive low pass filter. It can be seen that when the variable frequency ACPD system is brought onto the rig this is not going to work as this will eliminate much of the frequency elements that are of interest. As shown in the work the main issue with the current induction heater is the lower frequency harmonics which are linked to the way that this furnace modulates power. It is likely that a different induction heating system would be needed that outputs at only one frequency. If this is the case then a band pass filter can be used, just eliminating signals in a narrow band around the frequency of the induction furnace allowing all other frequencies to be utilised by the ACPD.

A robust beach marking approach has been introduced using fracture mechanics to predict the position of the crack front, in a stepwise cycle by cycle approach. Testing and refinement of this technique can be found in the Beach Marking chapter.

The advanced ACPD system has been developed, input and measurement hardware tested, methods to ensure repeatable accurate measurements have been covered. The current input system has been shown to work well enabling currents of up to 3A to be input at frequencies from DC to 250kHz. The measurement amplifier has been tested and found to have issues at high frequencies due to the common mode voltage on the sample. This problem

---

has been solved by using an amplifier with higher common mode rejection, this amplifier is AC coupled so cannot resolve DC signals, this is not a problem in the higher frequency work where DC is not of interest. The shielding of the measurement wires has been shown to be key to reliable signals, this is very relevant in both the bench work that has been undertaken here and will also be relevant when transferring to the test rig. The shielding developed here can be transferred to the test rig, it should be noted that a smaller, high temperature solution would be needed, given the temperature of the sample and the space envelope. This could be achieved with a Nickel based metal box with a ceramic or glass isolating layer to isolate this electrically. This isolation could be achieved by a thin glass shim or a plasma vapor deposition (PVD) coating of a ceramic or glass.

## 4. BEACH MARKING

### 4.1 *Introduction*

This covers the work undertaken looking at beach marking to monitor crack growth. A typical method of using a hold has been used to successfully mark SS316 and a new technique has been developed for marking fracture surfaces in a controlled and repeatable manner.

Beach marking relies on the topography of a fracture surface being influenced by the loading under which the fracture occurred, for example in quasi-static loading the trained eye can easily determine a brittle fracture from a ductile one. Likewise, in fatigue loading the texture of the fracture surface can be modified by different loading conditions. In some materials and test conditions changing the loading can affect the crack growth rate, there may be a transition time between different loading conditions, taking a significant number of cycles for a new loading regime to establish steady state crack growth. This interruption of the loading may also affect the crack growth possibly affecting the path or shape of the crack, this has even been used in some testing to ensure that non-uniform crack growth does not occur [96]. Therefore in this work the changes to the loading have been kept to a minimum, also the aim of this work is not to measure crack growth rate but is centred on marking the crack position and shape at pre-determined times in the fatigue test.

The purpose of this study was to develop a controlled and repeatable marking to give a snapshot of the location of the crack front at user defined times and in a range of materials. This can be used to monitor the progression of cracks and to calibrate other crack growth measurement equipment by marking the fracture surface of a calibration specimen at known points. This

---

can then be linked with measurement from the technique under calibration at those points. Some of this work has been used to calibrate the ACPD system within other sections of this project.

## 4.2 Test Interruption Beach Mark Testing

### 4.2.1 316 Stainless Steel

During the development of the fixed frequency ACPD system there was a desire to check the linearity of the Matelect ACPD system. To do this hold periods were put into a test, the test was undertaken at 600°C the maximum load was 9.1kN with an R-ratio of 0.1, the hold periods were at mean load with a duration of 2 hours. This produced marks on the fracture surface that could be clearly seen using a Nikon SMZ1000 stereo-zoom microscope as in fig. 3.8, using oblique lighting to accentuate the shadowing on the small steps that occur at the hold periods. It can be seen that there is a clear mark for each hold period. To further investigate these marks the sample was also examined using a Jeol XL30 SEM, the images from this can be seen in figs. 4.1 to 4.4.

These images using back scattered electrons can highlight the same features as the oblique lighting in the optical microscopy, but with the advantage of higher magnification without the limitation of a small depth of field that is seen in high magnification optical microscopy. Secondary electron images tend to either highlight compositional changes or topographic variation, in this case the topographical information is of interest. Sloped areas appear dark due to the arrangement of the detector, this means that the back scattered electrons do not reach the detector as they are scattered at an angle too low to be detected. fig. 4.5 shows a comparison of the highest magnification image using both back scattered and secondary electron. The edge of the step is marked with the red line, it can be seen that there is a steep step between the two regions of crack growth.

Another test was run to check that this could be replicated, in this 2000 test cycles were run interspersed with the eight 2 hour hold at mean load, an

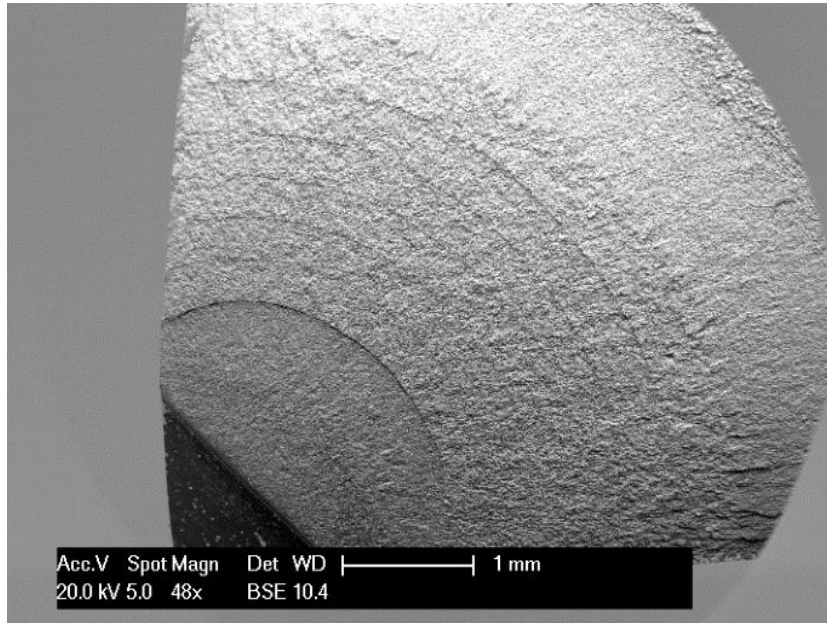


Fig. 4.1: Hold Marked Surface - Back Scattered Electron

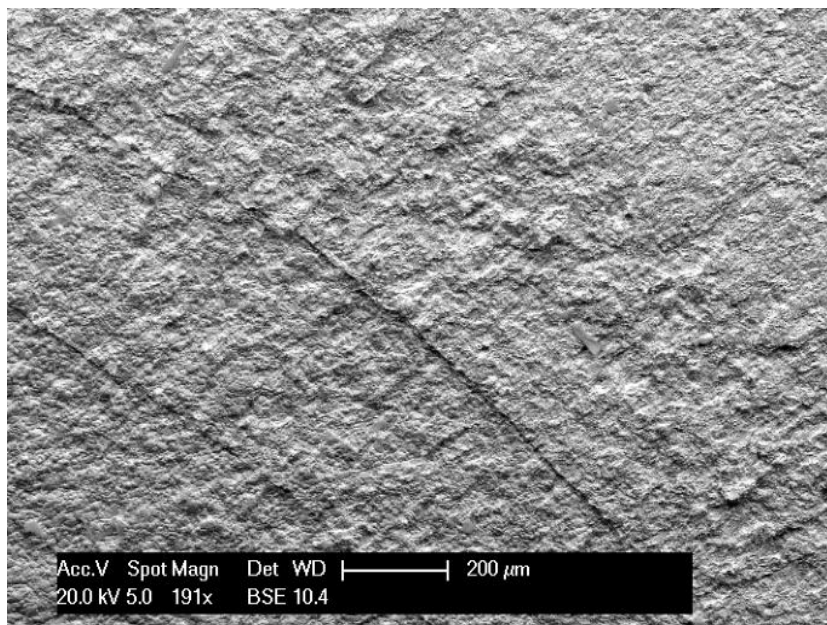


Fig. 4.2: Hold Mark Low Magnification - Back Scattered Electron

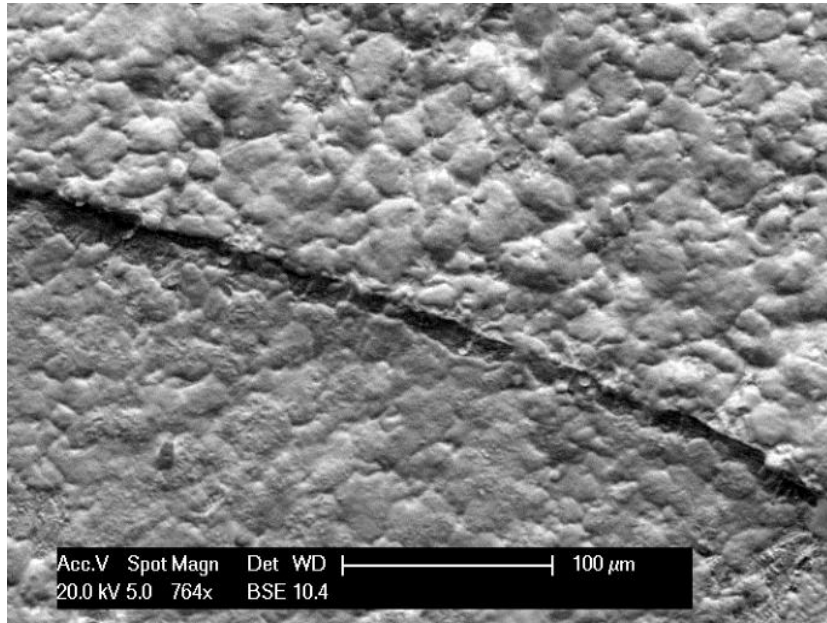


Fig. 4.3: Hold Mark Medium Magnification - Back Scattered Electron

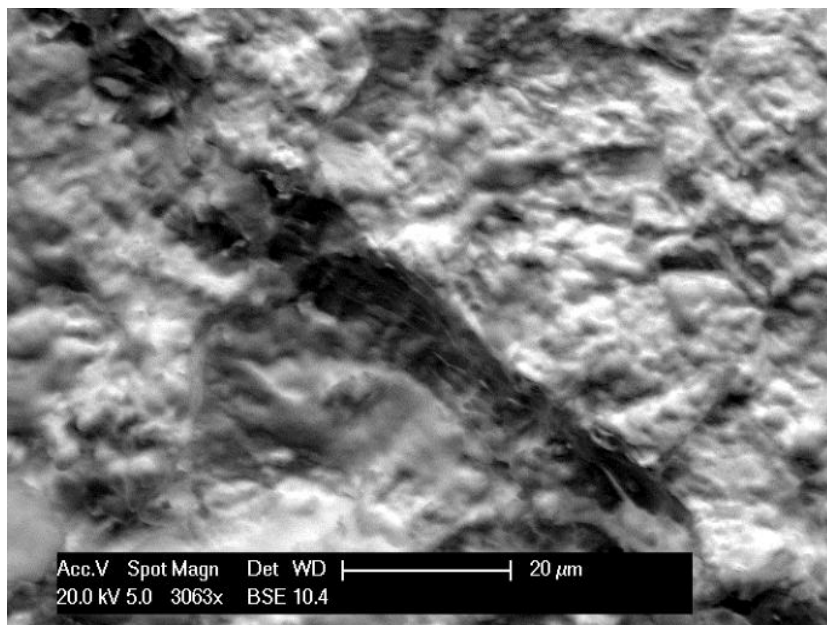


Fig. 4.4: Hold Mark High Magnification - Back Scattered Electron

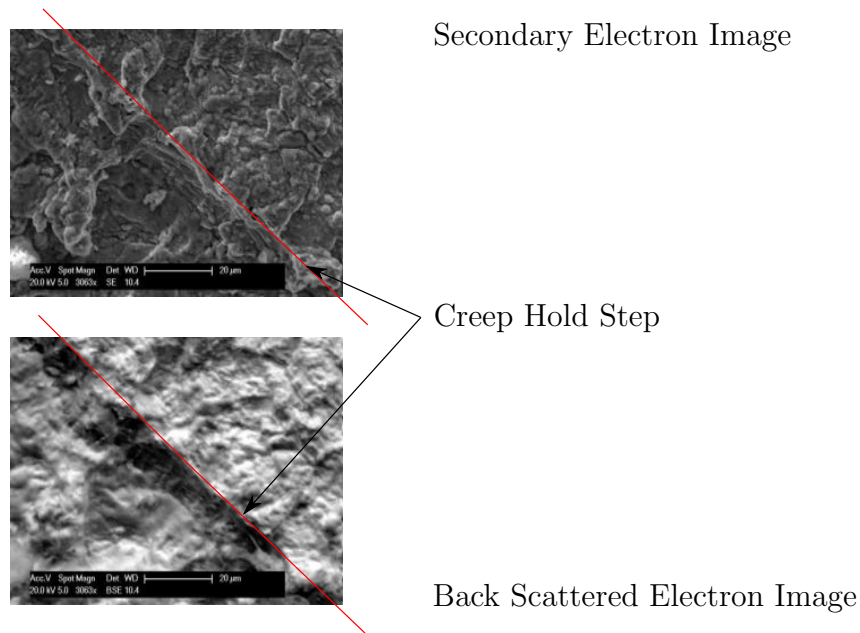


Fig. 4.5: Hold Step in Secondary and Backscattered Electron Modes

image of this fracture surface can be seen in fig. 4.6. The raw data potential drop against cycle number can be seen in fig. 4.7, in the hold periods data was recorded at the frequency of the test cycle therefore this is plotted as effective cycles. It can be seen in the potential drop data that the steps occur at the end of the hold period when the test load is reapplied. This is likely to be due to accumulation of creep damage during the hold period, this weakens the material in the highly stressed region ahead of the crack tip. Once the test load, which is higher than the hold load, is applied there is local failures in this damaged region leading to a step in crack growth and on the fracture surface.

With a view to develop this technique into other test conditions further tests were undertaken using the same loading conditions, with fatigue interspersed hold periods, at temperatures of 400°C and 500°C. In these tests no surface marks were seen, figs. 4.8 and 4.9, this is attributed the the creep rate at these lower temperatures being significantly lower therefore the accumulation of creep damage ahead of the crack tip is not sufficient to have

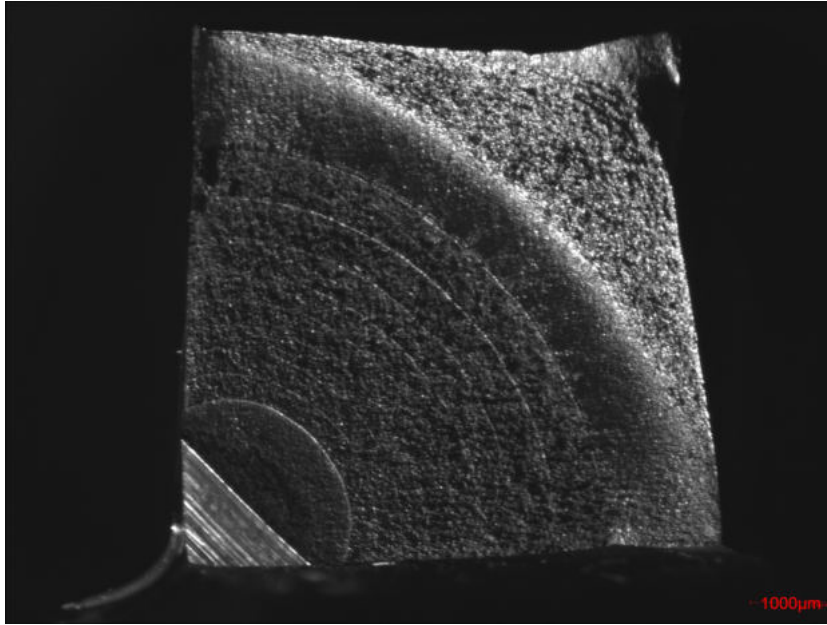


Fig. 4.6: Eight Hold Marks - Optical Microscope Image

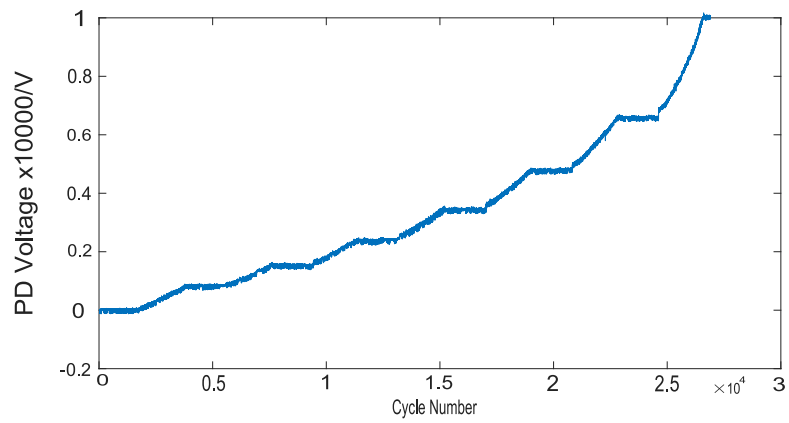


Fig. 4.7: Eight Hold Marks - Potential Drop Data

significant local failures on the reapplication of the fatigue loading. A test was also conducted at 500 °C with a higher hold load. A higher load was chosen based on the typical yield stress of SS316, taking the mean load of the holds at 600 °C was 5kN taking this as a proportion of the UTS the equivalent proportion of the UTS at 500 °C was calculated at 6.3kN. The holds were for 2 hours as in the other tests, these still did not show any marks, higher stresses or longer hold periods may produce marks fig. 4.10. However longer hold periods would extend the tests to an amount that could not be tolerated. So it was concluded that this method is not ideal and only produces good marks at high temperatures such as 600 °C.

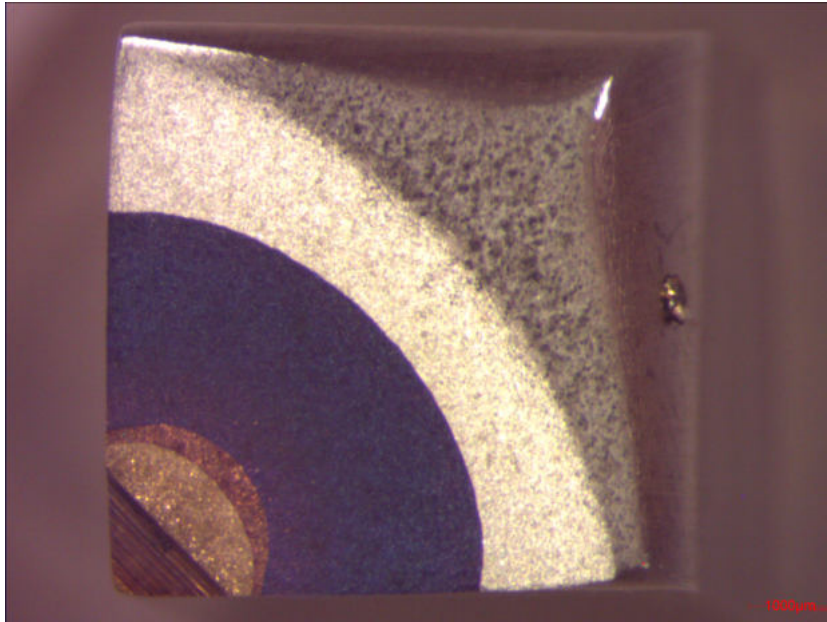


Fig. 4.8: 2 Hour Holds at Mean Load - 400 °C

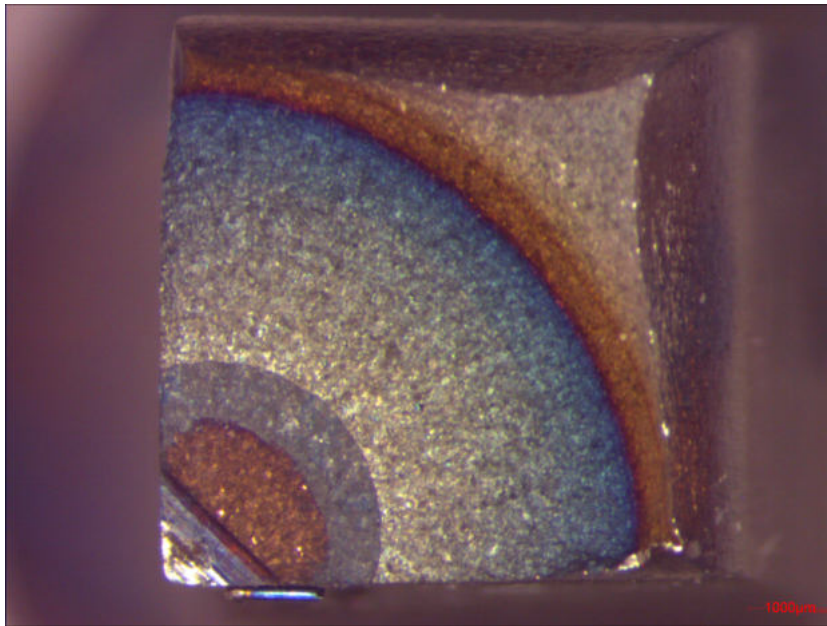


Fig. 4.9: 2 Hour Holds at Mean Load - 500 °C

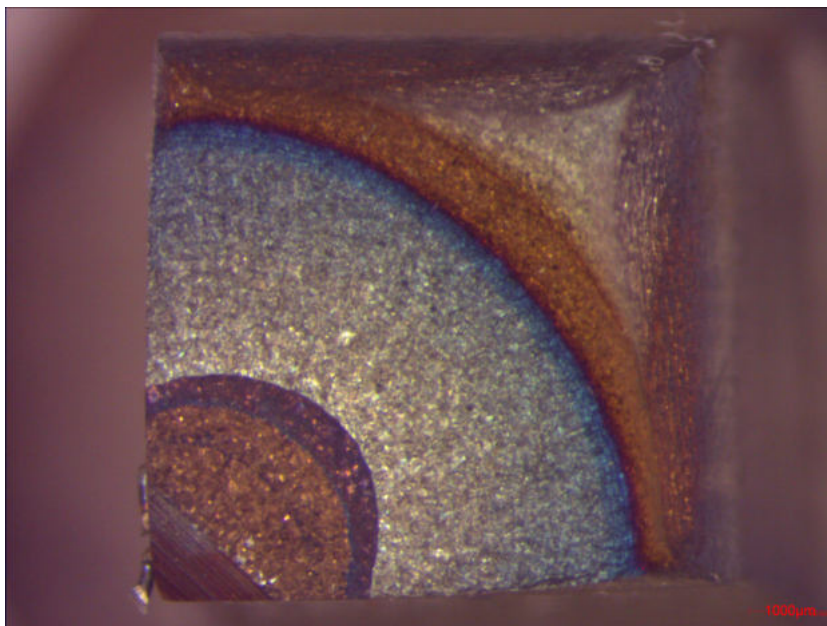


Fig. 4.10: Holds at 6.288kN Beach Marks Trials - 500°C

#### 4.2.2 RR1000

Within the package of work to investigate the crack growth rate in RR1000 there was the opportunity to undertake a trial to understand the feasibility of beach marking in this material. To maximise the benefit from these high value samples a range of marking strategies were tried on one specimen, these were:

- Cycling at R-ratio of 0.7
- Creep hold
- Cycling at R-ratio -1

As with the work on SS316 the beach marking periods were interspersed in a test waveform with R-ratio 0.1. However as this material is much stronger than the SS316 the maximum load applied for the test periods and cyclic beach mark periods was 24.5kN. An annotated image of the resulting fracture surface taken with plane lighting on Nikon SMZ1000 microscope can be seen in fig. 4.11, this shows that all of these marking strategies can be identified on the fracture surface. The creep hold period has the least distinct mark, only being noted by the small change in colour, in this there is not a step. This is expected due to the high creep resistance of this alloy. It can also be noted that the colourations may not follow what could be expected, it can be seen the the R=0.7 region is very light in colour in spite of being exposed to high temperature in the presence of air for most of the test whereas the R=-1 region is very dark in colour as may be expected in a heavily oxidised surface. Therefore the colouration may not be due to oxide film thickness, to further understand this the sample was examined on the Joel XL30 SEM. There are also some marks in the pre-crack, these are from the load shedding during this period. The crack being initiated at high load and the max load being reduced to ensure that the precrack is at a lower K value than the test waveform.

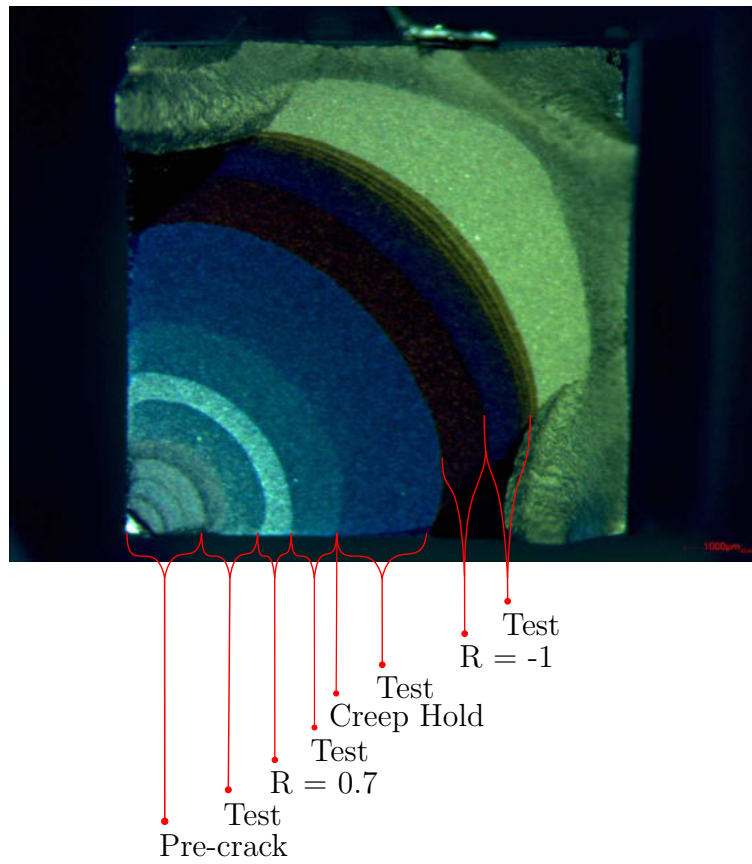


Fig. 4.11: RR1000 - Beach Mark Trial

### 4.3 Fracture Mechanics Method

Following on from this work it was considered that it may be possible to use reduced R-ratio sections to control beach marking. The use of the reduced R-ratio should not induce an increased plastic zone in front of the crack tip therefore should have a minimal effect on the crack growth, the change of loading regime should produce a band that can be seen on the fracture surface. In the RR1000 beach mark trial, the number of cycles needed to give a clear mark was estimated, this is not very reliable. It was thought that if the Paris coefficients are known for the test and a beach marking waveform then the number of cycles needed to generate a given crack growth could be calculated, details of these calculations can be seen in section 3.1.4, this can then be used to design a fracture surface giving test sections and a predetermined number of beach marks. This approach was attempted on two materials, RR1000 was chosen as marks had clearly been seen in the trials, SS316 was also chosen to trial the method on a different material.

#### *RR1000*

To undertake the calculations of the crack growth the C and m constants for both the test waveform and the beach mark waveform, in this case R=0 and R=0.7 respectively. The values for the R=0 waveform were known from the previous work on crack growth rate in RR1000 in LCF conditions, however the R=0.7 had not been tested, therefore a test with R=0.7 was undertaken. A test was run at 750°C, R=0.7, 500MPa bulk stress at a loading frequency of 1Hz, an image of the resulting fracture surface can be seen in fig. 4.12. The purpose of this R=0.7 is to generate a fracture surface which appears different to the test surface, at R=0.1. It can be seen that the resulting fracture surface is dull in colour and highly textured, and very similar to the fracture surface observed in the R=0.1 test with the same temperature and stress level this can be seen in fig. 5.8. Therefore this is not a useful texture to use for a beach mark as it may be indistinguishable from the fracture surface generated during normal cycling. It is thought that this is due to creep being significant at this high temperature and therefore this fracture

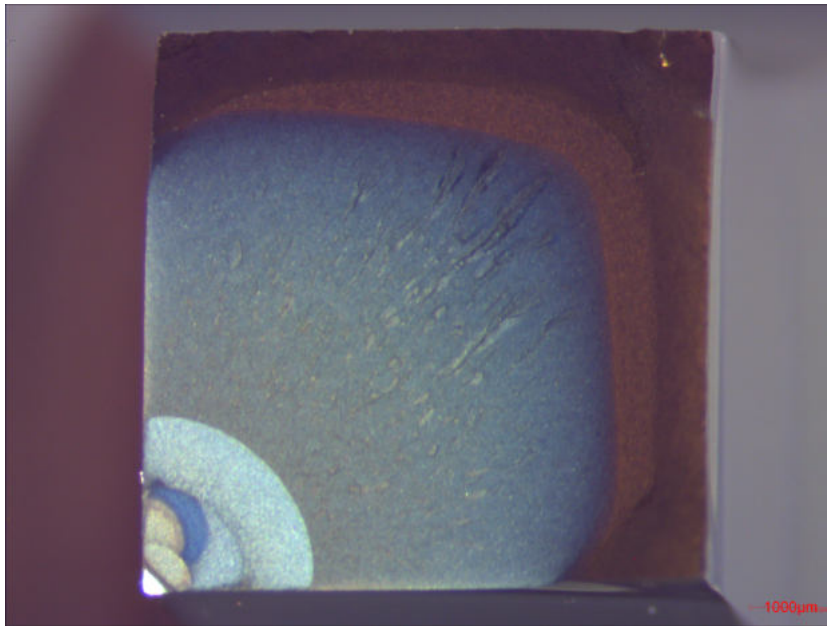


Fig. 4.12: RR1000 Fracture Surface - 750°C R=0.7

surface is dominated by the effect of time under load rather than to effects driven by the fatigue loading. This theory is also corroborated by the strong non-quarter circular growth, which is also seen in conditions where creep has an effect. This also links into the beach marks trials where an R-ratio of 0.7 had been seen to give a clear beach mark at 525°C, see fig. 4.11. At this lower temperature the crack growth is more planar, quarter circular and can be considered to be much more strongly linked the the fatigue loading.

Given that this beach mark methodology is aimed at fatigue and that the marking is clear at 525°C it was decided to move to 525°C for the remainder of this study. A test was therefore carried out at 525°C, R=0.7, 500MPa bulk stress at a loading frequency of 1Hz, an image of the resulting fracture surface can be seen in fig. 4.13. It can be seen that this is a much smoother fracture, synonymous with fatigue and does exhibit quarter circular crack growth.

With this crack growth rate data for tests at R=0 and R=0.7 it was then possible to make the first predictions, and to attempt to design a fracture surface.

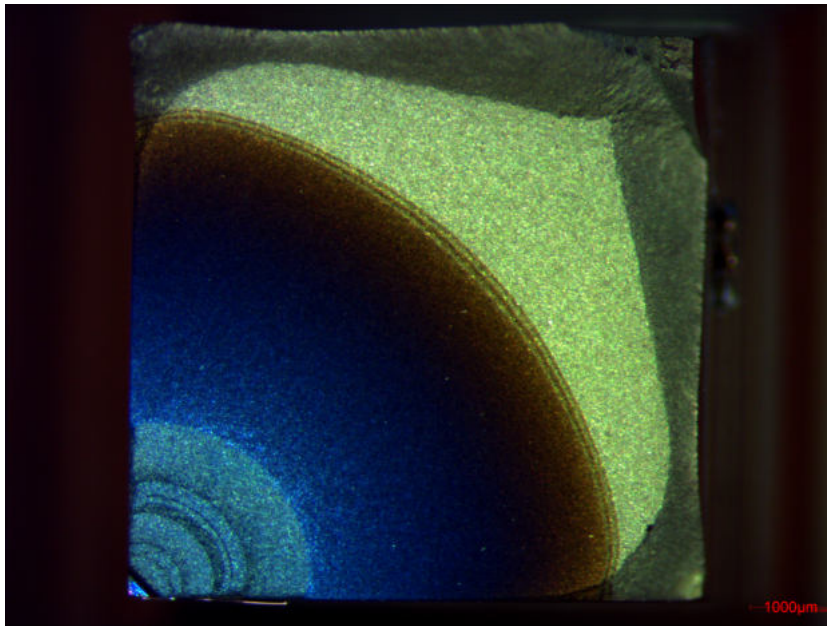


Fig. 4.13: RR1000 Fracture Surface - 525°C R=0.7

A short MATLAB script (appendix A.5) was written to calculate the number of cycles required to generate a specific crack growth, given the starting point at the beginning of that step. The first step starts at the end of the pre-crack, this length was measured on the pre-cracking machine with the sample held at 19kN (the maximum tensile load in the last stage of pre-cracking) to ensure that the crack was open. The distance between the edge of the sample to the end of crack was measured using a travelling microscope. In this first test the pre-crack was 1.8mm long, this was input into the script along with the C and m values for the test condition and the number of cycles to generate 0.5mm of crack growth was calculated. This was then repeated for a series of test and beach mark steps, using the calculated length at the end of the previous step to be the starting length for the next step. table 4.1 shows the plan for this first test showing steps of test, R-ratio of 0 and beach marks with an R-ratio of 0.7, bulk stress of 525MPa and temperature of 525°C.

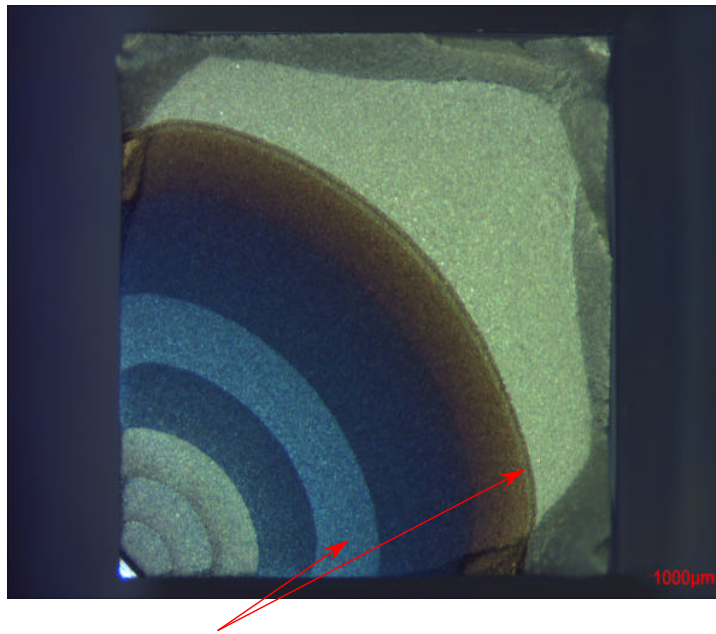
This test ran but the crack growth rate was higher than predicted, so the sample failed three cycles into the third test section. Once fractured

Step	Desired Step Size/mm	Predicted Cycles	Crack Length/mm
Pre-crack			1.80
Test1	0.50	2314	2.30
Beach1	0.20	17980	2.50
Test2	0.50	676	3.00
Beach2	0.10	3083	3.10
Test3	0.50	286	3.60
Beach3	0.30	3587	3.90
Test4	3.10		failure

Tab. 4.1: Beach Mark Plan 1

the resulting surface, fig. 4.14, was examined and the pre-crack and beach marks were measured. This showed that the crack growth moved out of plane in the region of 4.5mm growth, it is noted that in the Rolls Royce testing standard it is considered that if the crack is over 0.6 of the width of the sample the test is considered void, in the case of these 7mm square samples this corresponds to a 4.2mm crack length. It is likely that at high crack length the assumptions made in the calculations of stress intensity factor can no longer be trusted. It was also noted that the initial pre-crack was 1.97mm not 1.8mm as measured with the travelling microscope. These combined may have resulted in the accelerated crack growth.

It was decided to eliminate one of these potential issues, to do this a limit was set on the ACPD signal which would stop the experiment before the limit of 0.6, this limit was determined by looking at data from previous test and was set to 1.3V. In the first test the pre-crack length was measured with a travelling microscope at the end of the pre-crack, with the sample held at maximum load to open the crack. This may have issues of inaccuracy in this measurement as the travelling microscope may not be correctly aligned and the crack can be hard to see through the microscope. Another method of measurement was tried for the second test, the length was measured using a Nikon Eclipse LV-150 metallographic microscope and this value was used as the length of the pre-crack. The same fracture surface was planned, table 4.2,



Beach Marks

Fig. 4.14: RR1000 Fracture Surface - Beach Mark Plan 1

Step	Desired Step Size/mm	Predicted Cycles	Crack Length/mm
Pre-crack			1.68
Test1	0.50	1004	2.18
Beach1	0.20	6577	2.38
Test2	0.50	421	2.88
Beach2	0.10	1909	2.98
Test3	0.50	230	3.48
Beach3	0.30	3527	3.78
Test4			stop on 1.3V limit

Tab. 4.2: Beach Mark Plan 2

using this pre-crack length and the test run.

The test ran well, stopping at the predetermined crack length, however was again much faster than predicted. Measurements on the fracture surface showed that the pre-crack length was 1.85mm not the 1.68mm as measured on the metallographic microscope, therefore it can be concluded that the end of the crack could not be seen on this microscope due to the sample being unloaded and the crack closed so this is not a good method to measure the pre-crack. Another test was undertaken with a short pre-crack this also ran much faster than planned, but inspecting the fracture surface it could be seen that there was some tunnelling in the pre-crack. This meant that the initial crack length was an underestimate.

As there is a need to know the initial crack length and this makes a significant impact on the calculated crack growth rate all the data from the pre-cracks was considered. After close inspection it was found that the crack length measured on the surface was always an underestimate of the average crack length as measured on the fracture surface. This data can be seen in fig. 4.15, it can be seen that there is a good linear fit showing that the true crack can be calculated using this eq. (4.1). It was also noted that the test with a very short pre-crack showed a much greater degree of tunnelling in the pre-crack, this was not included in the data to calculate the true crack length factor. It was also decided to standardise on a minimum pre-crack of

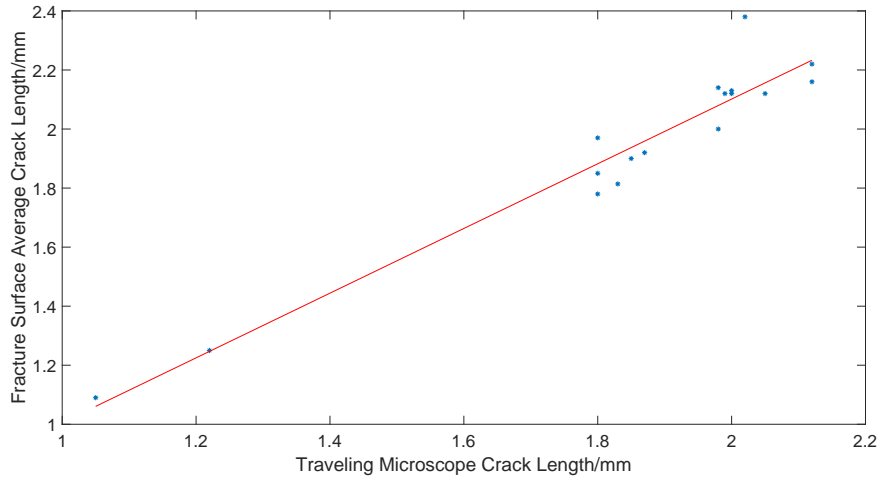


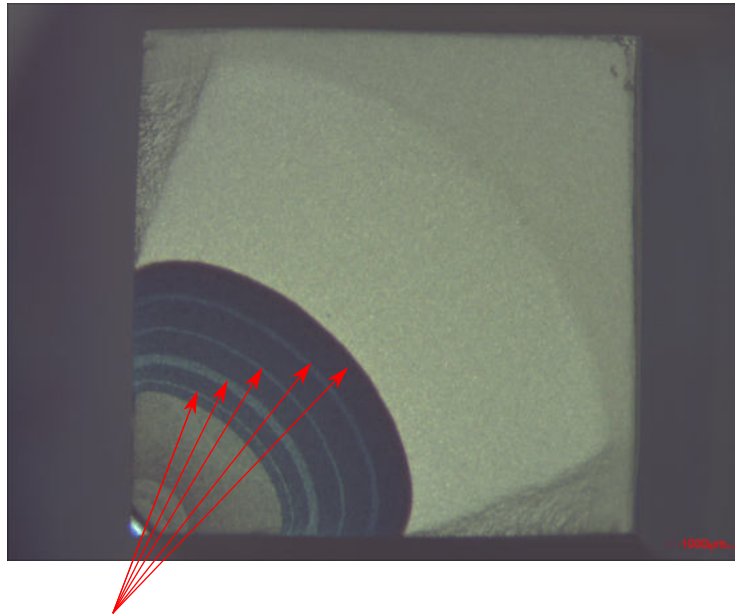
Fig. 4.15: RR1000 Comparison of edge crack length and average crack length

1.8mm, to ensure that the crack was at a suitable length for the factor to be relevant.

$$(AverageCrackLength(mm)) = 1.1138(TravelingMicroscopeReading(mm)) - 0.1124 \quad (4.1)$$

Using this correction factor another test was undertaken, the test plan can be seen in table 4.3. The test ran to plan and stopped in the last beach mark region on the 1.3V limit on the ACPD system, the resulting fracture surface can be seen in fig. 4.16. The positions of the marks were compared to the plan and the accuracy of these was found to be better than 0.97, this can be seen in fig. 4.17 and the full data in table 4.4. The step accuracy is not so good but this is to be expected as a small real error can give a large percentage error if the beach marks size is very small.

This has shown that the method with the crack length correction factor gives good results, the calculations do accurately predict the position of the crack front during the tests and as a result the beach marks are in the desired positions. In the work shown here it can be seen that marks as small as  $25\mu\text{m}$  can be made, to demonstrate the control that this technique provides two more tests were devised. One in which a series of equally spaced  $25\mu\text{m}$  beach



Beach Marks

Fig. 4.16: RR1000 Fracture Surface - Beach Mark Plan 5

Step	Desired Step Size/mm	Predicted Cycles	Desired Crack Length/mm
Pre-crack			2.1
Test1	0.10	146	2.20
Beach1	0.025	874	2.27
Test2	0.20	235	2.43
Beach2	0.13	3409	2.55
Test3	0.30	232	2.85
Beach3	0.050	994	2.90
Test4	0.40	207	3.30
Beach4	0.10	1410	3.40
Test5	0.30	103	3.70
Beach5	0.025	279	3.73
Test6	0.20	55	3.93
Beach6	0.20	1844	4.13
Test7	0.10	21	4.23

Tab. 4.3: Beach Mark Plan 5

Step	Desired Step Size/mm	Desired Crack Length/mm	Real Step Size/mm	Real Crack Length/mm	Step Size Accuracy	Crack Length Accuracy
Pre-crack		2.1		2.0		
Test1	0.10	2.20	0.15	2.14	1.45	0.97
Beach1	0.025	2.27	0.04	2.18	1.62	0.98
Test2	0.20	2.43	0.22	2.40	1.09	0.99
Beach2	0.13	2.55	0.13	2.53	1.08	0.99
Test3	0.30	2.85	0.32	2.86	1.08	1.00
Beach3	0.050	2.90	0.06	2.91	1.11	1.00
Test4	0.40	3.30	0.38	3.29	0.94	1.00
Beach4	0.10	3.40	0.11	3.40	1.08	1.00
Test5	0.30	3.70	0.31	3.70	1.02	1.00
Beach5	0.025	3.73	0.05	3.76	2.16	1.01
Test6	0.20	3.93	0.09	3.85	0.46	0.98
Beach6	0.20	4.13	Stopped on 1.3V limit			
Test7	0.10	4.23				

Tab. 4.4: Beach Mark Plan 5 - Results

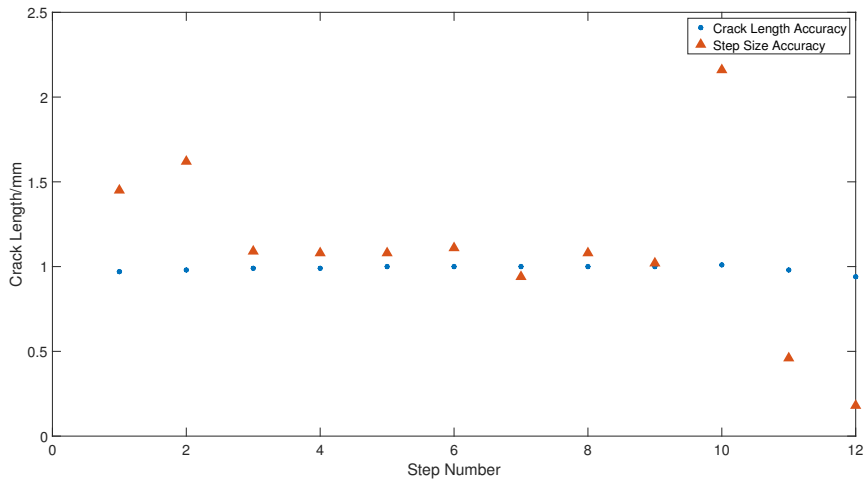


Fig. 4.17: Beach Mark Plan 5 - Accuracy Plot

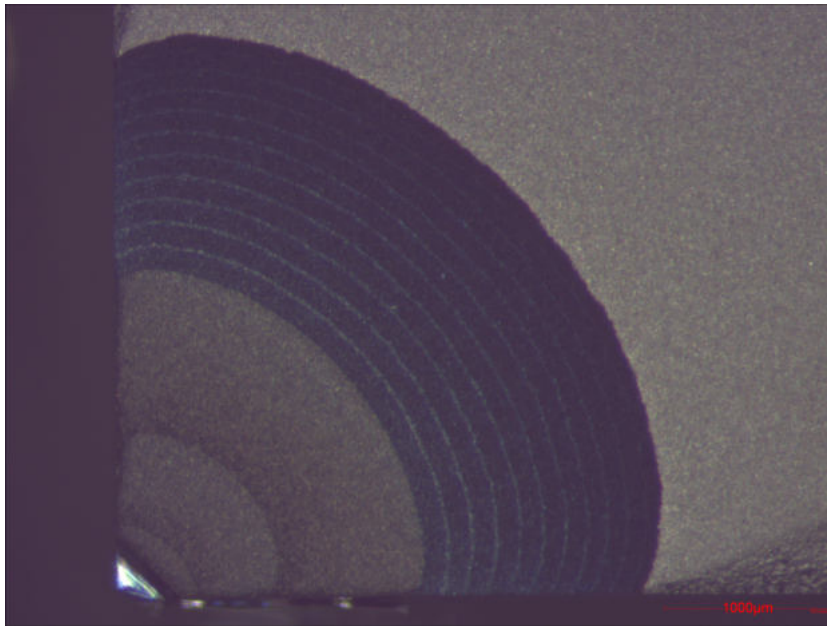


Fig. 4.18: RR1000 Fracture Surface -  $25\mu\text{m}$  Marks equally spaced - Beach Mark Plan

marks are used to mark the crack front at ten locations and a second in which a series of increasing and then decreasing beach marks and test regions give a symmetrical pattern. The resulting fracture surfaces can be seen in figs. 4.18 and 4.20.

The test with the  $25\mu\text{m}$  marks again shows accuracies of crack length better than 0.97, fig. 4.19 and table 4.5. However in the symmetrical test there was an experimental problem, a thermocouple wire came off the sample causing the sample to cool to room temperature in the second test step. The thermocouple was reattached and the test resumed from the cycle in which the thermocouple became detached. Visually on the fracture surface it would seem that the test continued successfully, fig. 4.20, however it can be seen from the measurements that from this point the accuracy drops to 0.84 see fig. 4.21 and table 4.6. Unfortunately, as this was the last sample, the test could not be repeated.

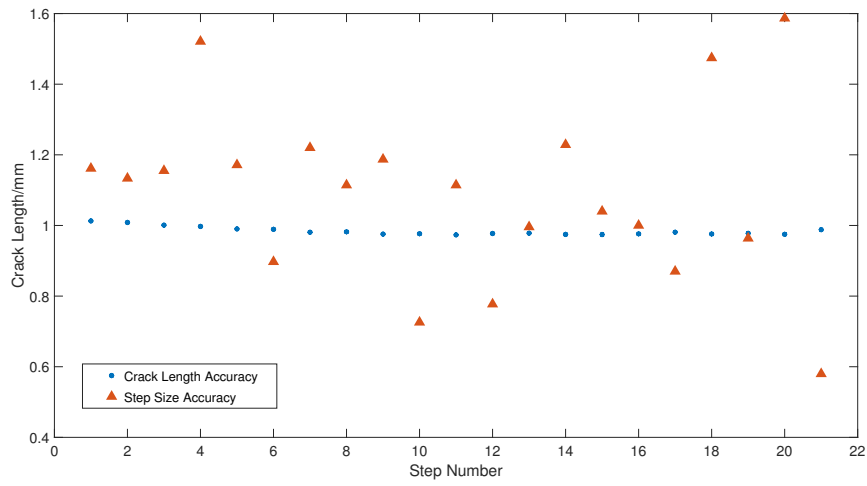


Fig. 4.19: Beach Mark Plan - 25 $\mu$ m Marks - Accuracy Plot



Fig. 4.20: RR1000 Fracture Surface - Symmetrical - Beach Mark Plan

Step	Desired Step Size/mm	Desired Crack Length/mm	Real Step Size/mm	Real Crack Length/mm	Step Size Accuracy	Crack Length Accuracy
Pre-crack		1.96		1.92		
Test1	0.10	2.06	0.16	2.03	1.16	1.01
Beach1	0.025	2.08	0.03	2.06	1.13	1.00
Test2	0.10	2.18	0.12	2.18	1.16	1.00
Beach2	0.025	2.21	0.04	2.22	1.52	1.00
Test3	0.10	2.31	0.12	2.33	1.17	0.99
Beach3	0.025	2.33	0.02	2.36	0.90	0.99
Test4	0.10	2.43	0.12	2.48	1.22	0.98
Beach4	0.025	2.46	0.03	2.51	1.11	0.98
Test5	0.10	2.56	0.12	2.62	1.19	0.98
Beach5	0.025	2.58	0.02	2.64	0.73	0.98
Test6	0.10	2.68	0.11	2.75	1.11	0.97
Beach6	0.025	2.71	0.02	2.77	0.78	0.98
Test7	0.10	2.81	0.10	2.87	1.00	0.98
Beach7	0.025	2.83	0.03	2.90	1.23	0.97
Test8	0.10	2.93	0.10	3.00	1.04	0.97
Beach8	0.025	2.96	0.03	3.03	1.00	0.98
Test9	0.10	3.06	0.09	3.12	0.87	0.98
Beach9	0.025	3.08	0.04	3.16	1.47	0.98
Test10	0.1	3.18	0.96	3.25	0.96	0.98
Beach10	0.025	3.21	0.04	3.29	1.59	0.98
Test11	0.1	3.31	0.06	3.35	.58	0.99

Tab. 4.5: Beach Mark Plan - 25 $\mu$ m - Results

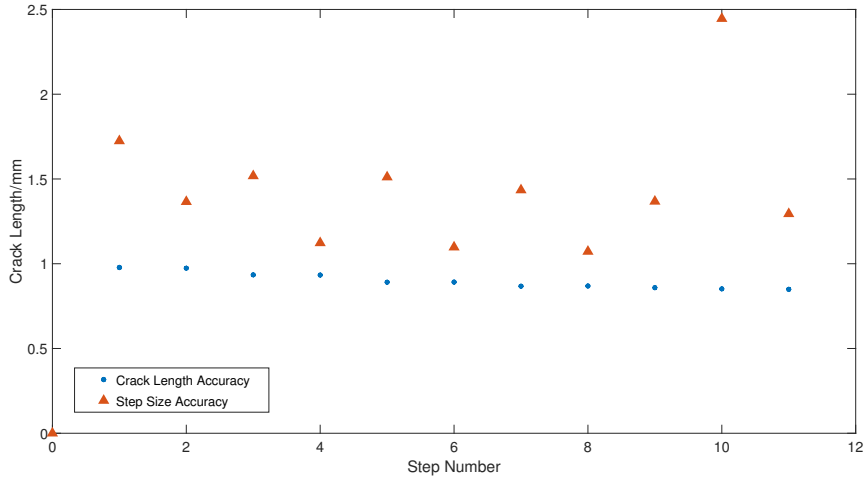


Fig. 4.21: Beach Mark Plan - Symmetrical - Accuracy Plot

Step	Desired Step Size/mm	Desired Crack Length/mm	Real Step Size/mm	Real Crack Length/mm	Step Size Accuracy	Crack Length Accuracy
Pre-crack		1.93		1.90		
Test1	0.10	2.03	0.17	2.08	1.72	0.98
Beach1	0.025	2.06	0.03	2.11	1.37	0.97
Test2	0.20	2.26	0.30	2.41	1.51	0.93
Beach2	0.05	2.30	0.06	2.47	1.12	0.93
Test3	0.30	2.60	0.45	2.92	1.51	0.89
Beach3	0.1	2.70	0.11	3.03	1.10	0.89
Test4	0.30	3.00	0.43	3.46	1.43	0.87
Beach4	0.05	3.06	0.05	3.52	1.07	0.87
Test5	0.2	3.26	0.27	3.79	1.37	0.85
Beach5	0.025	3.28	0.06	3.85	2.45	0.85
Test6	0.1	3.38	0.13	3.98	1.29	0.85

Tab. 4.6: Beach Mark Plan - Symmetrical - Results

---

*SS316*

Trials were undertaken on SS316 to understand the transfer of this technique onto another material, SS316 was chosen as samples were readily available. 600°C was selected as the testing temperature for this following on from the work using hold periods at mean load. Work had already been undertaken at an R-ratio of 0.1 so this was to be used as the test waveform, this was used to calculate the crack growth rate parameters for the test regions. It was necessary to undertake a test at a different R-ratio for a beach mark,  $r = 0.7$  was chosen as this worked well in RR1000. In this initial test it was found that the crack growth rate on this was too slow, after 11.5 days the crack had grown in the region of 0.3mm, in principle the crack was growing but given the available time on the testing machine this was impractical. Therefore another test was put on with an R-ratio of 0.5, this had a more reasonable growth rate so was used as the beach mark waveform in this work.

A test was designed with a variety of test steps and beach marks the predicted cycles required for each step are detailed in table 4.7. An image of the resulting fracture surface can be seen in fig. 4.22, this was taken using oblique lighting. The dark region is the area which was formed during the pre-crack and test, and is darker in colour due to oxidation, the bright region is a result of the cycling at room temperature after the test to fracture the sample. The very flat region adjacent to the notch is the pre-crack, which has subsequently been oxidised during the test, the main region is the test region which can be distinguished as this has more texture. Some small marks can be seen in this region, however they are not as clear as in RR1000. These marks were measured and compared to the ACPD data from the test, these do not match up very well with the beach mark region and it is not possible to be sure which mark relates to which period. Due to this a calculation of the accuracy of the marks, as in RR1000, is not shown here. As these accuracies cannot be calculated however to enable the data to be presented, a plot can be seen in fig. 4.23, showing the ACPD data and the positions where marks can be seen. In this figure the test and beach mark regions can be seen in the ACPD data, the steeper portions of the curve are the test regions and the less

Step	Desired Step Size/mm	Predicted Cycles	Desired Crack Length/mm
Pre-crack			1.98
Test1	0.50	4285	2.48
Beach1	0.10	2437	2.58
Test2	0.75	3160	3.33
Beach2	0.20	1417	3.53
Test3	0.40	885	3.93
Beach3	0.05	191	3.98
Test4	0.22	377	4.20

Tab. 4.7: Beach Mark Plan SS316-1

step the beach mark regions as the crack growth rate in the test regions is much higher than in the beach marks. The first planned beach mark cannot be seen on the fracture surface, this can be attributed to the very small crack growth, which was measured on the ACPD to be only  $8\mu\text{m}$ , much less than the planned 0.1mm. The later marks may correlate with the other planned beach mark regions however this cannot be considered definitive as they are very faint and there is an additional mark which was not planned. It can also be seen in the ACPD data that there are steps at the end of the beach mark regions, it is thought that this may be what is being observed on the fracture surface however this is not clear.

Due to the ambiguities in this first test another was planned with large regularly spaced test and beach mark steps, in an attempt to make it easier to see the marking on the fracture surface. An image of the resulting fracture surface can be seen in fig. 4.24, it should be noted that this image was not taken with oblique lighting as with the one for the previous test as there were no step type features observed, in contrast there were some differences seen with a more general lighting. The positions of these changes in pattern were measured and a plot of the ACPD data overlaid with the observed marks can be found in fig. 4.25. The first mark on the surface, which is a step, can be attributed to an experimental error whereby the test machine shutdown and this has marked the surface, after this the test was continued. Again

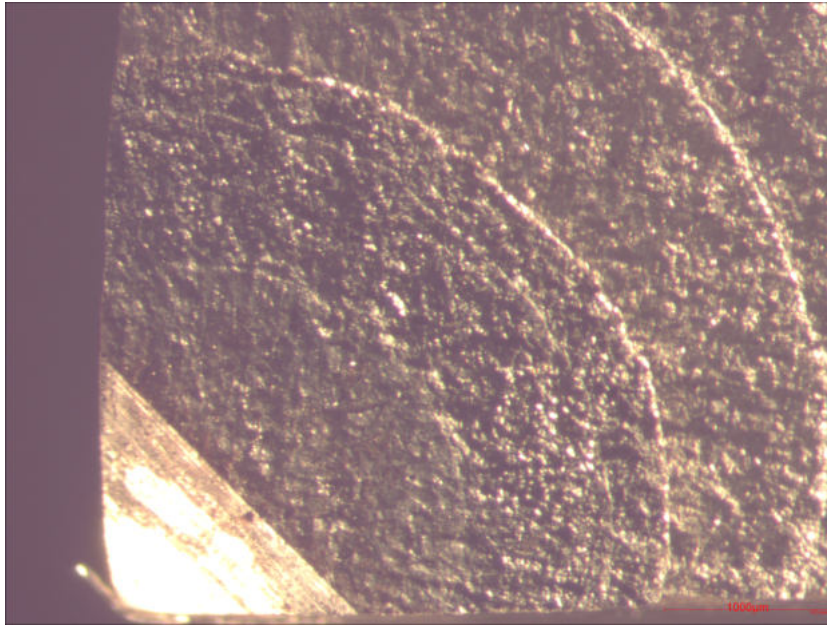


Fig. 4.22: SS316-1 Fracture Surface - Beach Mark Plan 1

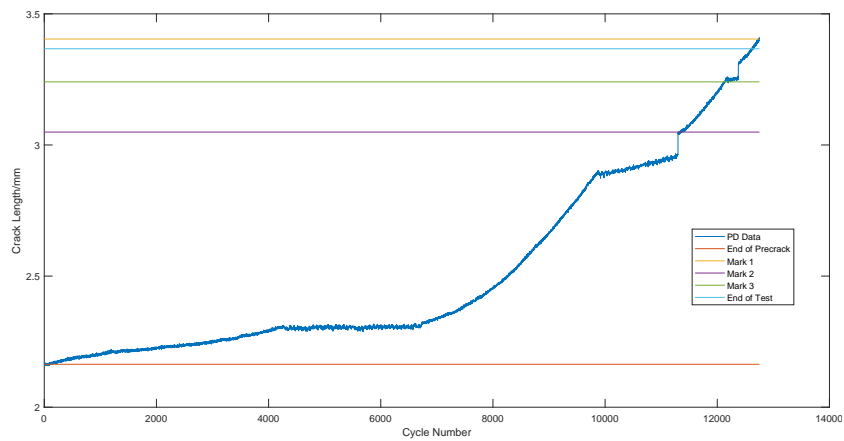


Fig. 4.23: SS316-1 Fracture Surface Measurements

Step	Desired Step Size/mm	Predicted Cycles	Desired Crack Length/mm
Pre-crack			2.20
Test1	0.60	4792	2.80
Beach1	0.30	5267	3.10
Test2	0.60	2027	3.70
Beach2	0.30	1695	4.00
Test3	0.60	1027	4.60
Beach3	0.30	679	4.90
Test4	0.6	592	5.50

Tab. 4.8: Beach Mark Plan SS316-2

the relationship between the observed changes on the fracture surface do not show clear a relationship to the changes between test and beach mark as on the ACPD.

Due to the availability of samples and time on the testing machine it has not been possible to complete this study. Some marking has been seen in SS316 but it is thought that this needs further investigation to fully understand the process by which this is happening.

## 4.4 Discussion

### 4.4.1 Test Interruption Beach Mark Testing

In this chapter a number of beach marking methods have been trialled, centring around holds and changes in R-ratio. In the SS316 work the holds at mean load have been very successful, the holds for 2 hours result in sufficient creep damage at 600 °C that a step in the fracture surface was observed. It can be seen in the ACPD data, see fig. 4.26, that this happens at the end of the hold period on resumption of the loading, this is due to the loading in the first cycle after the hold period giving a higher stress ahead of the crack tip than the creep damaged material can support. It can also be seen that this step becomes larger through the tests, this is linked to the high K value giving a higher stress ahead of the crack tip coupled with the greater creep

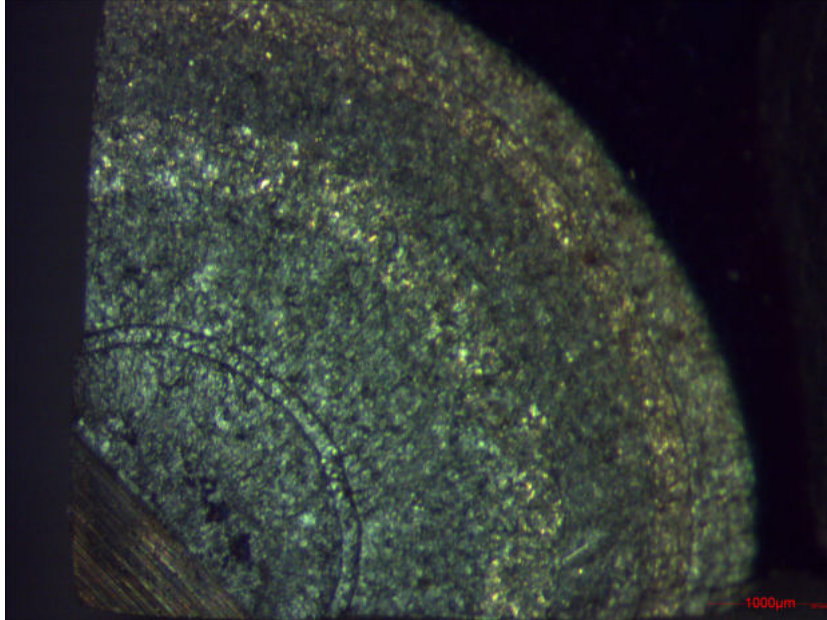


Fig. 4.24: SS316-2 Fracture Surface - Beach Mark Plan 2

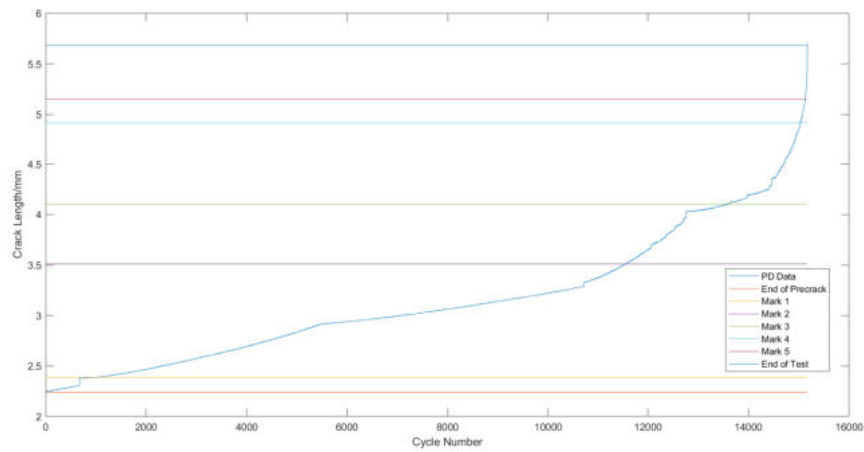


Fig. 4.25: SS316-2 Fracture Surface Measurements

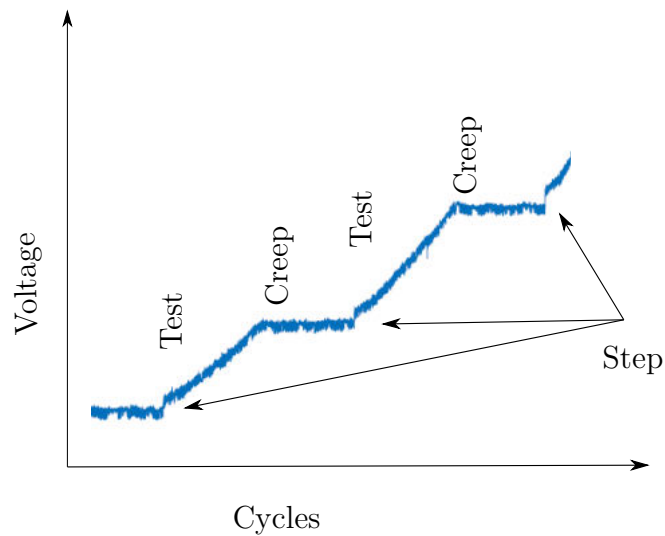


Fig. 4.26: Steps in ACPD data on resumption of loading

damage due to the stress seen in the hold period being higher again due to the the higher  $K$  at longer crack lengths.

The hold at mean method was also tried at other temperatures 400 and 500 °C, however due to the lower creep rates at these temperatures this did not result in sufficient damage to give rise to a step. For example the creep rate of SS316 would be expected to be about 0.02 % per hours at 600 °C and only 0.001 % at 500 °C [105]. Holding for around 20 hours may therefore give rise to a mark however this is too time consuming in a test program.

Given the availability of samples and the interest in RR1000, work was also carried out on this material. A range of methodologies were tried:

- Cycling at R-ratio of 0.7
- Creep hold
- Cycling at R-ratio -1

These all produced clear marks on the fracture surface by eye and on an optical microscope as can be seen in fig. 4.11. The sample was also studied on an SEM to further understand the reason for the different colouration.

fig. 4.27 shows a low magnification SEM image of the whole fracture surface, the black speckling is some non-conductive contamination and should be ignored. The  $R=0.7$  region is still clearly visible but most of the other marks are not clearly defined in the electron microscope. At higher magnification the distinction between the  $R=0.7$  region and the test region can be seen. The test region is rough with a significant amount of micro-cracks, whereas the  $R=0.7$  region is much smoother and planar with minimal cracking. The texture in the  $R=-1$  region is similar to the test areas so the distinction cannot be seen on the SEM. The rough texture and micro-cracking could lead to the darker appearance in both the back scattered electron and optical microscope images. The back scattered electrons from surfaces which are at high angles do not reach the detector, also the electrons emitted in the cracks will get reabsorbed into the wall of the crack these will lead to a darker appearance. Likewise in optical microscopy the surfaces that are not perpendicular to the viewing angle will appear dark as the light will not enter the microscope also cracking can lead to the light being absorbed in the cracks and not exiting so cannot be viewed. fig. 4.28 shows some images using both back scattered and secondary electrons to show the rough surface and the micro-cracks during the test area. In comparison the equivalent images from the  $R=0.7$  region can be seen in fig. 4.29, show much less cracking and a smoother planar fractures. The SEM was also used to gain some insight into the texture in the  $r\pm 1$  region. This was found to have significant texture as in the test areas, but this also exhibits cracking that runs perpendicular to the direction of crack growth, an image of the cracking can be seen in fig. 4.30. This additional cracking may be the cause of the very dark appearance of this region in the optical images.

The SEM investigation shows a good correlation between the macro scale fracture surface and the topography and cracking, however oxidation could also play a role in the appearance of the different areas. To investigate this Energy-dispersive X-ray Spectroscopy (EDX) analysis of the test and beach mark areas was carried out. This technique is available on the Joel XL30 SEM, on a well prepared sample this can give quantitative chemical compositions for metallic samples this would need to be a polished surface.

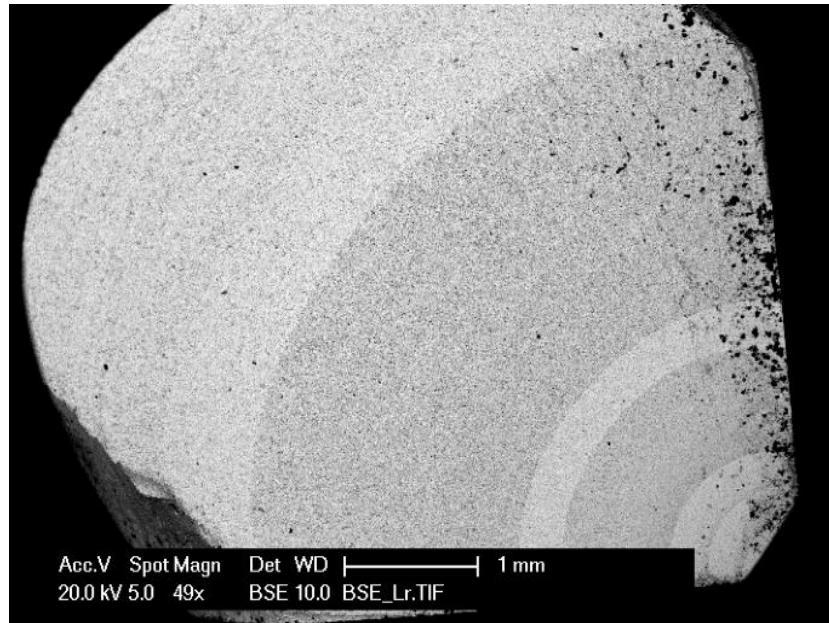


Fig. 4.27: RR1000 - Fracture Surface - Low Magnification - Back Scattered Electron

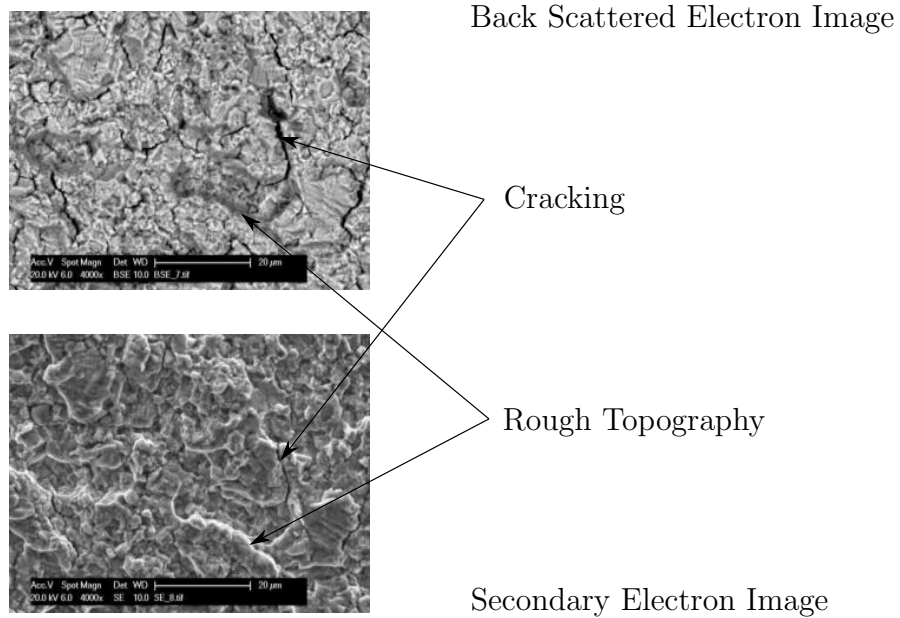


Fig. 4.28: RR1000 - Test Area - Back Scattered and Secondary Electron Images

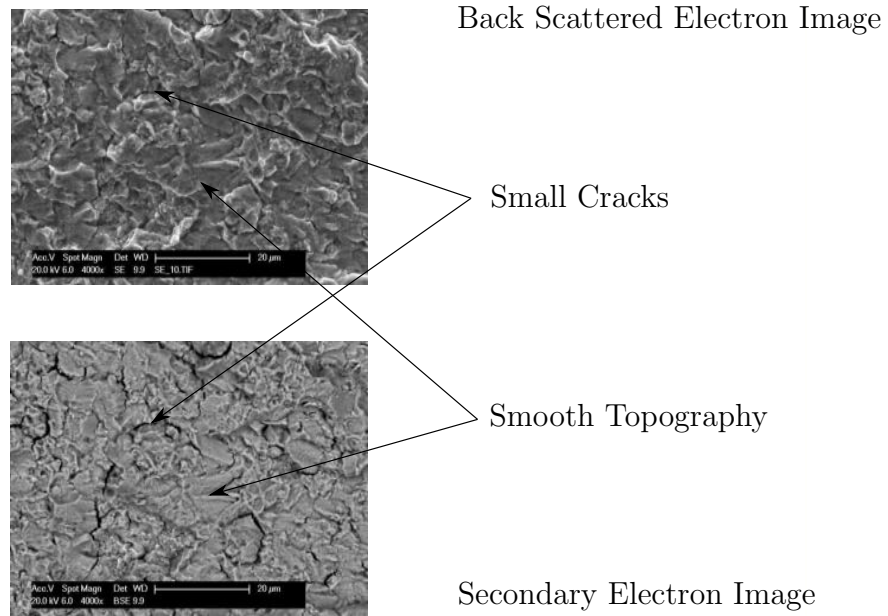


Fig. 4.29: RR1000 - R=0.7 Area - Back Scattered and Secondary Electron Images

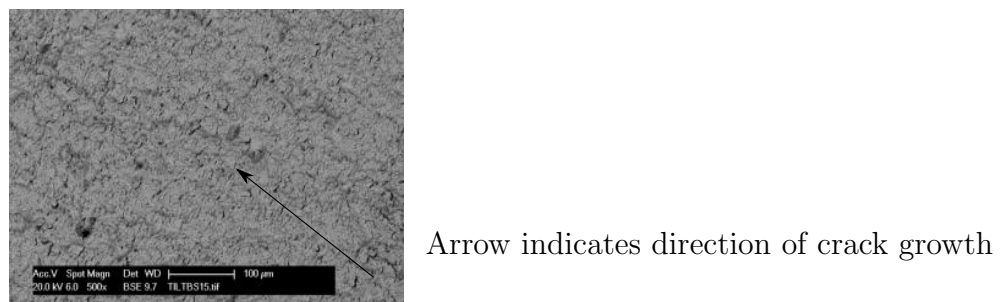


Fig. 4.30: RR1000 - R=-1 Area - Back Scattered Electron Image

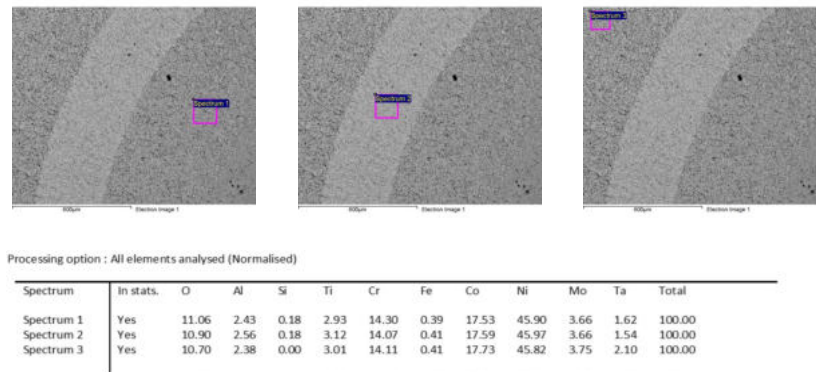


Fig. 4.31: RR1000 - Test Area 1 = Spectrum1 - R=0.7 Area = Spectrum 2 - Test Area 2 = Spectrum 3

Polishing would remove the fracture surface so this is not appropriate in this case, however more qualitative data can be collected from an unpolished surface.

It can be expected that the EDX analysis will sample the composition of the bulk metal as well as the oxidation and any surface contaminants. As this is being used as a qualitative tool all the measurements have been normalised to give a total composition of 100%. In this analysis, a thicker oxide layer will contribute to the measured result more strongly, showing a higher percentage composition at the expense of other elements. The longer a surface is exposed to an oxygen containing environment the more heavily oxidised it will be and this layer will be thicker, therefore it is expected that the older a fracture surface is the higher the oxygen content will be on the EDX analysis.

Firstly it can be seen that there is a much higher oxygen content in the spectra in fig. 4.31 both the surfaces from the test condition and R=0.7 both exhibit oxygen contents in the region of 11% whereas the younger surfaces from later in the test in fig. 4.32 show lower oxygen contents. The test region in these later stages showing less than 10% and the R=-1 only 7.5%.

Considering only the data comparing the test and R=0.7 regions, shown

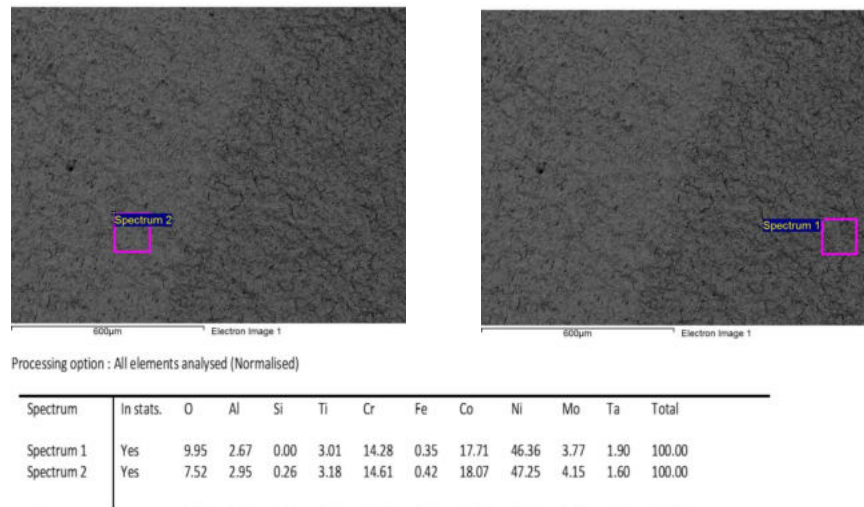


Fig. 4.32: RR1000 - Test Area 3 = Spectrum1 - R=-1 Area = Spectrum 2

in fig. 4.31, can be seen that the chemical composition of the different regions are very similar. The oxygen content reduces slightly in line with the age of the fracture surface, therefore this cannot be linked to the micro-scale appearance of the fracture surface. In the later stages in fig. 4.32 the oxygen content is changing rapidly, this can be attributed to the very short time that these surfaces were exposed to the air. In this late stage of the test the crack was growing very fast and the sample failed very shortly after the surfaces were generated. It is normal for a more highly oxidised surface to appear less reflective, however the darker R=-1 region has a lower oxygen content than the preceding test region. This quite sizeable change in oxygen content is believed to be due to the age of the surface not in relation to the R-ratio. Therefore it can be seen the oxygen content variation between the different regions is due to the age of the surface and the differences in appearance can be linked to the topography and cracking.

#### 4.4.2 Fracture Mechanics Method

In this work it has been shown that the fracture mechanics method works well, allowing the marks to be spaced as desired during the test and the size of these marks can be set as desired. A clear understanding of the initial position of the crack front is key in this as all subsequent calculations are based on this one value, if this is not correct then the subsequent crack growth rates cannot be determined. In this work it has been shown that the crack is not perfectly quarter circular, the crack growth is slightly retarded at the surface of the specimen. As the measurement of the crack length on the surface is the only method of measuring the initial crack length it is therefore essential to understand the degree of this retardation of the crack growth. By studying previous data it was possible to characterise this and create a correction factor. If the factor is applied the method worked well.

It has been shown that the predicted crack length error is less than 25% and in some cases such as the test with  $25\mu\text{m}$  steps the error was down at 2%. The step size accuracy is significantly higher, giving 30% to 50% error in some cases, however it should be noted that this is a percentage error and the step sizes are small so the absolute error does not affect the overall crack length error too much; resulting in acceptable levels of error, particularly in the case of the small beach marks. From this observation smaller beach marks give better overall accuracy, this would also normally be the better approach from an experimental view point enabling most of the loading to be in the test mode and only a small proportion to be beach marks. The error here is being driven by the beach mark steps and moving from a test step to a large beach mark step is pushing the error up. This can be attributed to the change of damage ahead of the crack tip, the large beach marking step changing the damaged area that the crack is growing into, this is less prevalent in the case of the small beach marks as there is significantly less growth in the beach mark mode so limiting the effect on the material ahead of the crack tip. Beach marks down to  $25\mu\text{m}$  have been tested here, the limitation of the size of a usable beach mark is linked to the method used to observe the fracture surface. The microscope system used in this has a digital

---

resolution of  $3.9\mu\text{m}$  per pixel, resulting in the  $25\mu\text{m}$  beaching marks being 6.3 pixels wide, given this marks much smaller would be hard to resolve.

The work on SS316 was less conclusive, unfortunately due to limited number of specimens this could not be brought to a full understanding. It can be seen that there is very little difference in surface texture between the 0.5 and 0.1 R-ratio regions. SS316 is much less crack sensitive than the RR1000, which lead to the 0.7 R-ratio crack growth being impractically slow. It may be that this approach would work better at lower temperatures where the material will be more brittle and less susceptible to creep effects, however it was not possible to investigate this due to sample and machine availability.

## 5. CRACK GROWTH TESTING RESULTS USING FIXED FREQUENCY ALTERNATING CURRENT POTENTIAL DROP

### 5.1 *Introduction*

Testing of two materials in both isothermal LCF and TMF conditions has been undertaken, with the aim of demonstrating the capabilities of the test rig and to generate some typical crack shapes. This will show the relevance of the techniques developed in this thesis around the topic of real time crack shape monitoring. The materials chosen were fine grain RR1000, sourced from the industrial partner, and SS316. The RR1000 was chosen due to the industrial link; there is interest in measuring crack growth rates in this material as cracking is seen in service. It is also known that RR1000 exhibits non-uniform crack growth in certain conditions. The SS316 was chosen as it is used in high temperature environments such as nuclear reactors [24, 29, 38, 43, 106]. Also much work has been undertaken on SS316 material at the University of Nottingham [1, 2, 4] so there is significant knowledge of this material in both mechanical and thermal loading and control, in addition this material readily available so is convenient for method development.

Samples were manufactured to suit the TMF machine that is available at the University of Nottingham, this machine had been further developed within this project to allow crack growth testing in both LCF and TMF conditions. A drawing of the samples can be seen in fig. 3.2. All calibrations of temperature and loading were undertaken to comply with BS ISO 12111:2011 [95], load calibration was carried out by an external company to UKAS standards to class 0.5 and the thermal control was verified in house to better than  $\pm 5$  °C.

This work aims to demonstrate the additional testing capability generated in this project as well as displaying a range of cracking behaviours in the materials. The test conditions were selected to be representative of a range of operating conditions both in isothermal and thermal cycling conditions. Throughout this all the mechanical loading has been in load control, extensometer control would be possible but this would be measuring the strain in the sample and crack opening. Given this the load control option was selected as the most suitable for the crack growth experiments. For all this work the crack growth rates were calculated as covered in section 3.1.4.

## *5.2 Stainless Steel - 316*

### *5.2.1 Test Conditions*

A range of LCF and TMF tests have been undertaken in the temperature range 400°C to 600°C with maximum bulk stress of 184MPa and R-ratio of 0.1. The temperature range was selected with reference to operating ranges for the material and previous LCF, TMF and creep work carried out at the University [1, 4].

Following the thermal calibration of the testing system it was determined that a reasonable frequency for the TMF was 0.012 Hz (83.3 seconds per cycle) due to limitations of cooling rate. The rate was chosen to ensure that the work was undertaken within the performance envelope of the system, ensuring that the temperature remained in control and the phase relationships between load and temperature were maintained. LCF testing was undertaken at two frequencies, work was undertaken at 0.25 Hz (4 seconds per cycle) and at 0.012 Hz as in the TMF testing. The slower 0.012Hz loading enables direct comparison between the LCF and TMF tests, at the same frequency.

### *5.2.2 Results*

All the data collected from this series of tests were processed as described in section 3.1.4, to calculate the crack growth rates. A plot of all the tests can

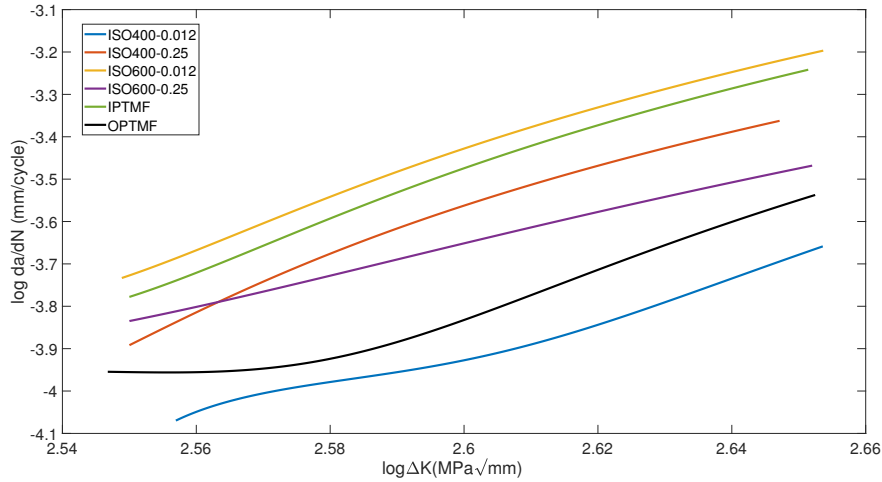


Fig. 5.1: SS316 Crack Growth Rates at Loading Frequencies 0.25 Hz and 0.012 Hz

Test	m	c
ISO400 0.012 Hz	5.13	-17.27
ISO400 0.25 Hz	5.52	-17.92
ISO600 0.012 Hz	5.30	-17.23
ISO600 0.25 Hz	3.78	-13.22
OPTMF 0.012 Hz	5.59	-18.35
IPTMF 0.012 Hz	5.50	-17.80

Tab. 5.1: SS316 Crack Growth Rate Parameters

be seen in fig. 5.1. There are a number of competing mechanisms at work in these tests, there is the temperature of the test affecting the strength and creep properties of the material along side this is the loading, the frequency and phase relationships (for the TMF) all play a part.

Firstly we can consider all the 0.012 Hz data. Four tests were undertaken at this frequency, isothermal LCF at 400 and 600°C and TMF both in and out of phase between these two temperatures. It can be seen in fig. 5.2 that there are two groups in this data, the LCF at 600°C and IPTMF are similar as are the LCF at 400°C and the OPTMF. So it can be seen that the LCF at 600°C shows the highest growth rates and there is a small reduction in growth rate in the IPTMF where the maximum loading is at the maximum temperature. The lower temperature at other loading points in the IPTMF

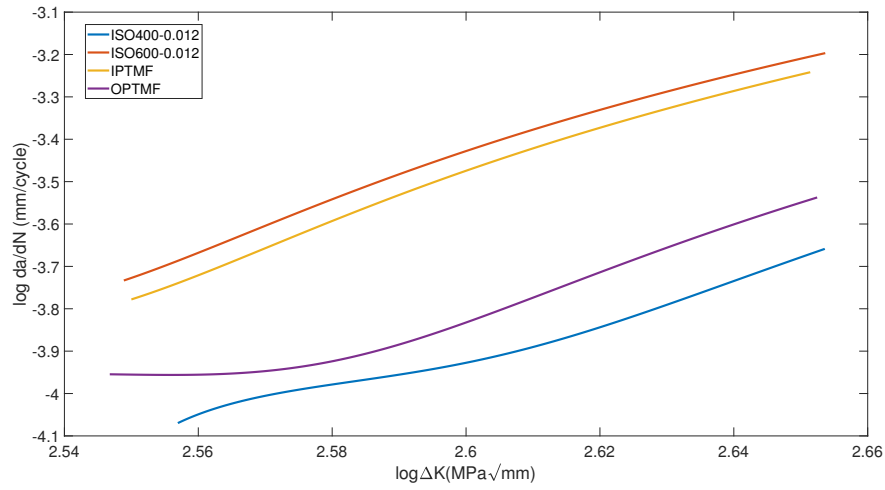


Fig. 5.2: SS316 Crack Growth Rates at Loading Frequency of 0.012 Hz

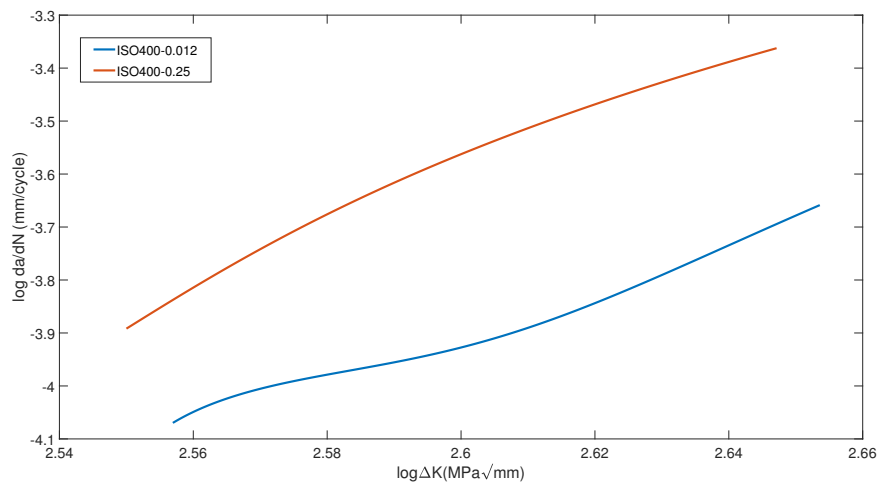


Fig. 5.3: SS316 Crack Growth Rates at 400°C

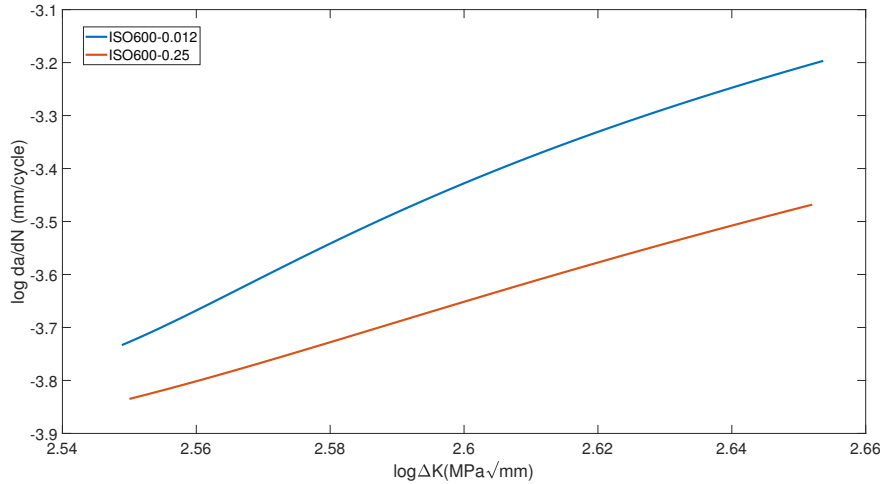


Fig. 5.4: SS316 Crack Growth Rates at 600°C

test does decrease the growth rate, which is to be expected. The other main group is the LCF at 400°C and the OPTMF, as with the other group LCF at 600°C and IPTMF. It can be seen that the lowest growth rate is for the LCF at 400°C and a small increase in rate is seen in the OPTMF due to the temperature being higher in other parts of the loading. figs. 5.3 and 5.4 show the comparisons between the two testing frequencies. In the LCF test at 600°C it can be seen that there is a reduction in crack growth rate with increased frequency although the gradient of the line is similar. Whereas in the low temperature case at 400°C the opposite is true, the higher loading rate exhibits the higher crack growth rate.

### 5.3 RR1000

#### 5.3.1 Test Conditions

For this material the LCF and TMF tests have been undertaken in the temperature range 300°C to 750°C, and for all but one test maximum bulk stress 500MPa and R-ratio of zero. The temperature and load range was selected in conjunction with Rolls Royce. These were chosen with a view to compare this facility with others and attempt a comparison of the data between

facilities and testing equipment. As tunnelling is an interest for both University of Nottingham and Rolls Royce, the opportunity of non-uniform crack growth was also considered. Tunnelling had been seen in much previous work in these load and temperature ranges so this was chosen with the view to possibly investigate this behaviour. In a project run at another institution a lower stress of 400MPa had been used, in this work non-uniform crack shapes were seen. In an attempt to replicate this work one test was also conducted at 750°C with a bulk stress of 400MPa.

Following the thermal calibration of the testing system it was determined that a reasonable frequency for the TMF was 0.005 Hz (200 seconds per cycle) due to limitations of cooling rate. As with the work on SS316, the rate was chosen to ensure that the work was undertaken within the performance envelope of the system. The lower frequency being necessary due to the significantly increased cooling time to achieve the low temperature of 300°C. It was decided to undertake the LCF testing at the same frequency to make the data more comparable by limiting the range of variables.

### *5.3.2 Results*

A plot of all the tests that were carried out can be seen in fig. 5.5 and the main crack growth rate factors can be seen in table 5.2. It can be seen in this plot that there are two main groups within this study, the LCF tests at 750°C and the IPTMF test have much higher growth rates compared to the other tests. This can be attributed to the fact that RR1000 has very little temperature dependency up to the region of about 700°C, the change over this temperature dominates the segregation here. In the two LCF tests at 750°C there is a small difference in crack growth rate, the lower stress exhibiting a slightly higher crack growth rate. It can also be seen that the IPTMF has a lower crack growth rate than the two LCF tests.

The other tests are all grouped in a fairly close band, even though there is a large range of temperatures in these tests. This all follows the basic trend, crack growth rate following temperature, the LCF test at 525°C being faster than 300°C. It should be noted that although 525°C is higher in growth rate

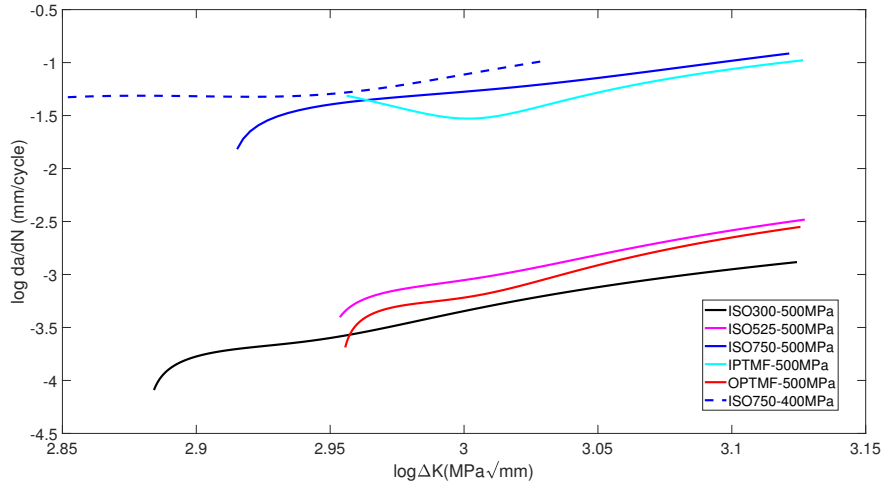


Fig. 5.5: RR1000 Crack Growth Rates

Test	m	c
ISO300 500MPa	4.38	-16.50
ISO525 500MPa	4.62	-16.91
ISO750 400MPa	1.71	-6.27
ISO750 500MPa	2.74	-9.47
IPTMF 500MPa	4.78	-15.89
OPTMF 500MPa	5.54	-19.83

Tab. 5.2: RR1000 Crack Growth Rate Parameters

than the 300°C test it is very much grouped with in the lower band.

Post test all the samples were observed on a Nikon SMZ1000 Stereo-zoom microscope and images of the fracture surface were taken, these can be seen in figs. 5.6 to 5.10 It can be seen that the two groups of test described earlier in the section have significantly different fracture surfaces. In the 1st category when the maximum load is seen at 750°C the crack remains in plane, perpendicular to the loading direction although in plane these are not quarter circular in shape figs. 5.8 and 5.10. It is not clear from this work at what point in the test the cracks departed from quarter circular; no surface markings can be observed to enable this. In other loading conditions non-planar crack growth is seen although this does remain quarter circular figs. 5.6, 5.7 and 5.9. The non planar growth is only exhibited at high crack

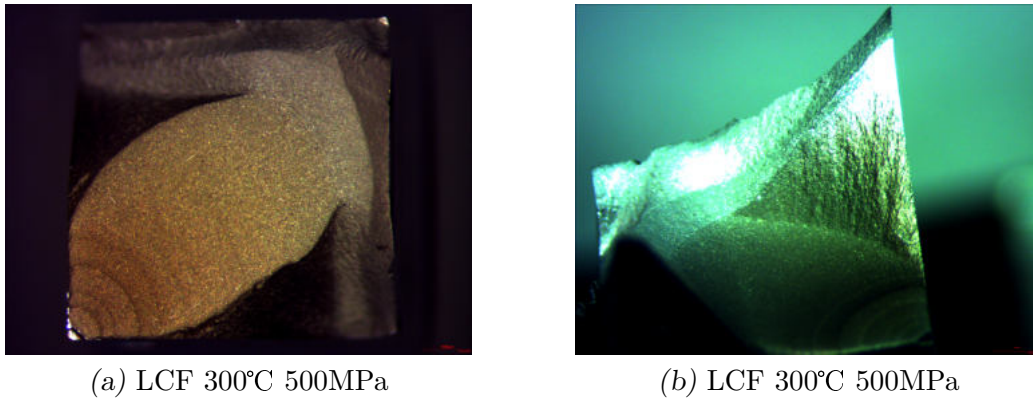


Fig. 5.6: RR1000 LCF 300°C

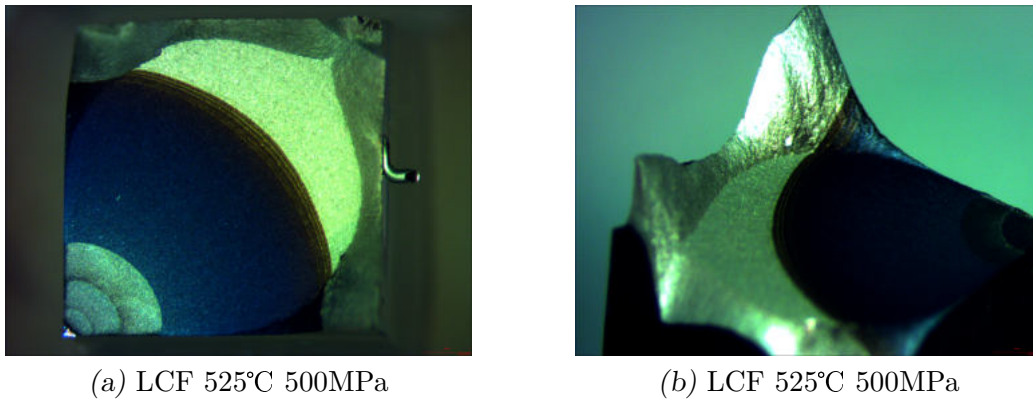
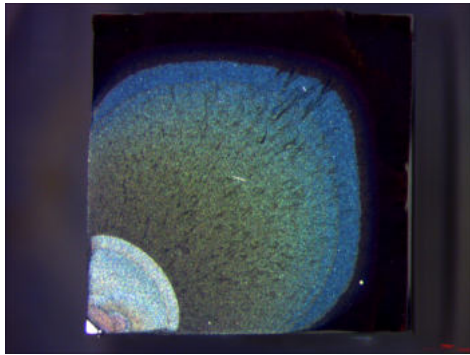


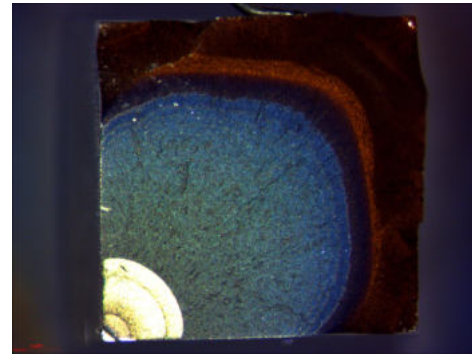
Fig. 5.7: RR1000 LCF 525°C

lengths, therefore has been eliminated from the crack growth calculations due to the  $a/w$  limit of 0.6.

One of the aims when deciding on test conditions for this work was to attempt to generate cracks that do not all grow in a quarter circular fashion. This has been seen in the LCF at 750°C and IPTMF tests, but non-planar growth has been seen in other tests. Although in this section of work no attempt has been made to measure this evolution of crack shape, this forms a good demonstration of the requirement to understand this in more detail. It is seen that the cracks start quarter circular and planar in the pre-cracking regions and end with a mixture of tunnelling and growth out of plain during the LCF and TMF tests. Measurements showing the degree of tunnelling

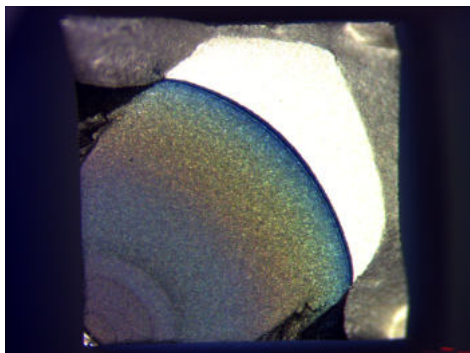


(a) LCF 750°C 400MPa

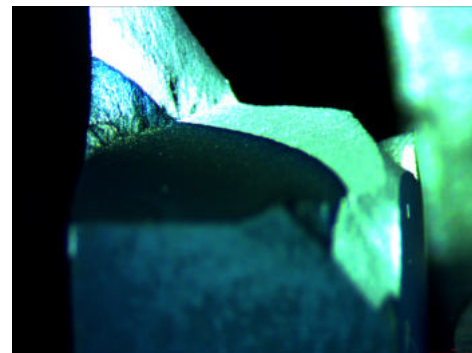


(b) LCF 750°C 500MPa

Fig. 5.8: LCF 750°C

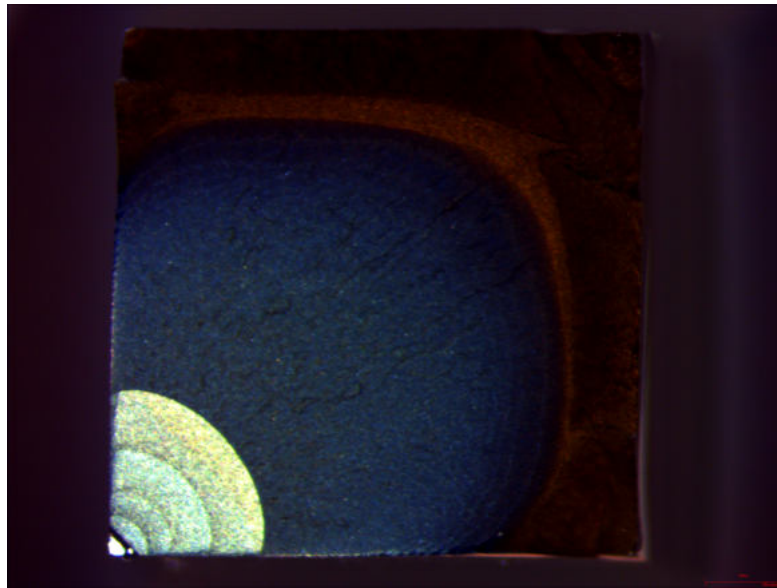


(a) OPTMF 300-750°C 500MPa



(b) OPTMF 300-750°C 500MPa

Fig. 5.9: OPTMF 300-750°C



(a) IPTMF 300-750°C 500MPa

Fig. 5.10: IPTMF 300-750°C

in the various tests can be found in table 5.3, a higher the ratio indicates a greater level of tunnelling.

## 5.4 Discussion

### 5.4.1 Stainless Steel - 316

Here two fatigue rates were explored in isothermal conditions, 0.25 Hz and 0.012 Hz. The slower crack growth rate at 600 °C at the 0.25 Hz frequency is believed to be due to the reduction in time at the higher loads due to the shorter cycle time, this reduces the time available for creep action at the high tensile loads. This is likely as creep is significant in SS316 at this temperature [1, 44, 47] given that it is significantly over the 0.4-0.5 of the melting point [107, 108] which is generally considered the region where creep becomes significant. The 400°C LCF tests reverse this trend, the higher rate test exhibiting a greater crack growth rate. It is considered that at this lower temperature the fatigue properties of the material are dominant, and in this case the rate is key not the time at high load for creep to happen.

Test/crack position	Average 0 and 90°length/mm	45°length/mm	Ratio
ISO300 500MPa Pre-crack	2.01	2.12	1.03
ISO300 500MPa End of Test	6.86	6.79	0.98
ISO525 500MPa Pre-crack	2.12	2.25	1.07
ISO525 500MPa End of Test	5.92	5.95	1.01
ISO750 400MPa Pre-crack	2.01	2.16	1.07
ISO750 400MPa End of Test	4.95	8.07	1.63
ISO750 500MPa Pre-crack	1.76	1.85	1.05
ISO750 500MPa End of Test	5.00	7.70	1.54
IPTMF 500MPa Pre-crack	2.04	2.17	1.06
IPTMF 500MPa End of Test	5.08	7.53	1.48
OPTMF 500MPa Pre-crack	2.11	2.13	1.01
OPTMF 500MPa End of Test	6.10	6.28	1.02

Tab. 5.3: RR1000 degree of tunnelling

Inspection of the fracture surfaces corroborate these conclusions, the 600°C tests show highly textured fracture surfaces where the 400°C tests have much more planar fatigue type surfaces.

When the rate effects are eliminated, with all tests being conducted at the same frequency of 0.012 Hz, comparing the LCF at different temperatures and the IP and OP TMF show that the predominant factor is the temperature at which the maximum load is applied. This temperature-load phase relationship, the temperature at peak load governing the response [33] can be seen in the IPTMF being most similar to the 600 °C LCF test and the 400 °C being similar to the OPTMF test. It would seem that the excursions to higher temperatures at low load have little effect on the crack growth rates in the OPTMF test, in some materials systems such excursion and possible oxide formation can have a the effect of increasing crack growth rates in OPTMF tests, but this is not seen in this testing on SS316. In the SS316 work very little non-uniform crack growth was seen and all the cracks grew in plane.

#### 5.4.2 RR1000

The crack growth rates in this testing on RR1000 are split into two bands which can be seen in fig. 5.5, those at 750 °C and the ones at lower temperatures. This can be attributed to the significant change in mechanical properties in RR1000 over approximately 700°C. It can be seen that there is a similar load-temperature phase behaviour in this material, the IPTMF sitting alongside the LCF test at 750 °C It can be seen that the OPTMF test sits within the band of lower LCF tests, this confirms that the main factor in this is temperature at maximum load although this does sit above the isothermal 300 °C test suggesting that the excursions to higher temperatures do have a small effect .

From looking at the micrographs of the fracture surfaces, figs. 5.6 to 5.10, significant non-uniformities can be seen. In the tests at 750 °C and the IPTMF test, cracks remain in plane but deviate significantly from a quarter circular crack shape, these tests all have a ratio of centre to end crack length around  $1.55 \pm 0.1$  . In other conditions cracks remain quarter circular, keeping a ratio of centre to end crack length within  $1 \pm 0.1$  , however some of the cracks significantly deviate away from the plane perpendicular towards the loading direction.

These deviations cannot be measured using DCPD or conventional ACPD. In the case of DCPD the area of the remaining ligament is measured which is not a function of the crack shape only the area that has been broken. With conventional ACPD we only measure the path length for the current flow, depending on the frequency of the applied AC current the current path may be different but with this one frequency measurement this would not enable any understanding of shape. This is a demonstration of the need for a method to measure this non-uniformity during the test, two methods are covered in other chapters covering beach marking and variable frequency ACPD.

## 6. ADVANCED ALTERNATING CURRENT POTENTIAL DROP DEVELOPMENT

### *6.1 Introduction*

Having undertaken work to investigate crack growth using fixed frequency ACPD a plan was developed to start the work on developing the ability to sample a wide range of frequencies. As the sample is cyclically loaded in the LCF or TMF test the crack opens and closes, the closing of the crack can add a conductive path extra to the one through the remaining material. This means that the time in the loading cycle when the measurements are taken needs to be known and controlled and if the different frequencies will be measured at different times then this also needs to be understood. In the fixed frequency work the supply current was passed through the sample continuously and readings taken alongside the other readings on the test system; load, displacement etc. The main reading was taken at maximum load when the crack is fully open therefore eliminating the current path due to the crack faces being in contact.

In this work to develop the technique a range of samples, with machined features, have been used to simulate cracks. Readings at a specific time the a loading cycle is not relevant for this study. However this equipment should be able to be deployed in LCF and TMF tests, so care has been taken to ensure that the measurements can be taken in a controlled manner over a short time period. This will enable this to be done on a real fatigue test when the sample is in the maximum tensile loading so the crack is open.

The development of the ACPD system can be split into two main areas. Initial work done using readily available equipment to understand the feasibility of this work and to identify possible challenges which could inform the

development of this. This initial work uses the Matelect equipment in a slow stepwise frequency sweep. The work then continues using the specially developed amplifier systems that can supply a user defined signal. This could be a sinusoidal signal that constantly increases in frequency within a few seconds this is often referred to as a chirp or a stepped sine signal.

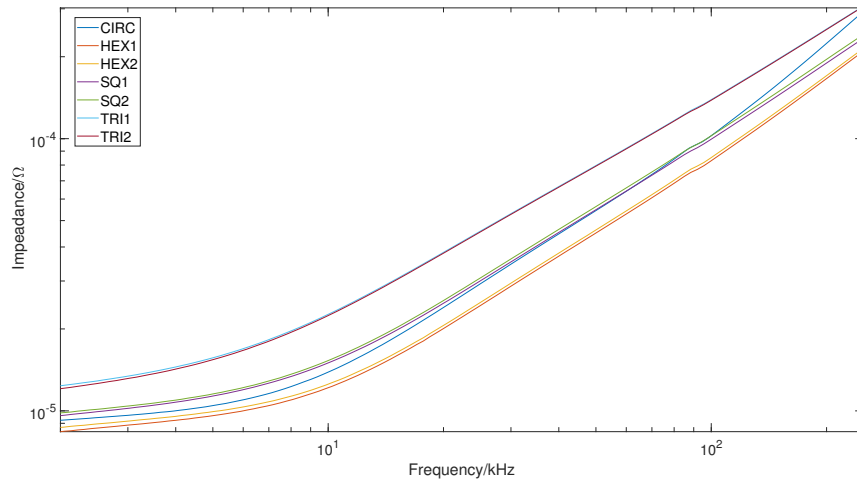
## 6.2 *Trials with Existing Equipment*

Pieces of 100mm square cross section 316 stainless steel were used in order to create samples with four different cross section geometries, circular, hexagonal, square and triangular. The Matelect unit controlled by the frequency sweep code (appendix A.1) was used to do some initial trials, measurements were taken on the four geometry samples. The test current was kept constant at 2A and the frequency was swept from 100Hz to 250kHz and the sine and cosine components of the voltage were read back and recorded at each step. This data could then be processed to give the magnitude of the voltage signal as well as the phase in relation to the input current. This data can be seen in fig. 6.1.

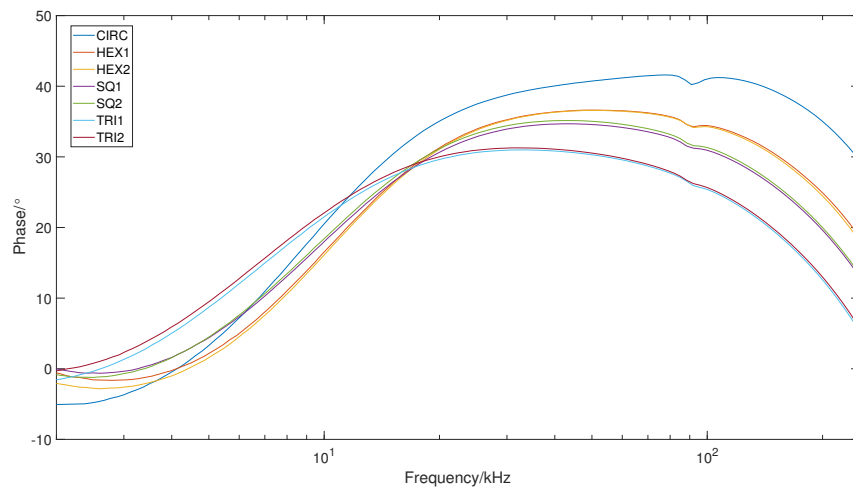
As these samples are 316 stainless steel the skin depth at 1kHz is 3.5mm and at 10kHz is around 1mm, the significant depth as described in eq. (6.1) is 5mm and this frequency is close to the thin skin condition. Therefore the transition from low frequency DC response across this range is reasonable. However there is little data at the lower end of this range and there is not a flat purely DC region as would be expected.

$$\text{Significant depth} = \sqrt{\text{area}}/2 \quad (6.1)$$

It can be seen that there are variations in both the magnitude and phase responses for the different geometries. These changes correlate with the internal angle of the apex, the 'severity of the apex'. In the circular sample the internal angle is effectively zero, the hexagonal is 60°, the square is 90° and the triangular is 120°. The response of the impedance and phase signals throughout the frequency range follow this order of severity of apex.



(a) Magnitude



(b) Phase

Fig. 6.1: Data from the Trials with the Matelect CGM-7

### 6.3 *Advanced Alternating Current Potential Drop*

Following the initial trials with Matelect unit there was one clear limitation, this was the time to run a sweep. The sweeps from 100Hz to 250kHz took about 45 minutes, in real tests under fatigue conditions it would be necessary to take all the readings at one point in the cycle. This would typically be at maximum tensile load when the crack is fully open, eliminating any path for current to flow between the fracture faces should the crack be closed or partially closed. The development of the equipment for the fast sweep is detailed in the Methodology chapter, in this chapter the experimental work on a range of samples is discussed.

#### 6.3.1 *Bench Samples*

In the initial work with the Matelect equipment only one batch of samples was used to start to investigate the feasibility of this method. In this work with the advanced ACPD equipment two additional batches have been produced. The three batches are:

- Cross Section Geometry

To investigate the effect of the shape of the section

- Feature Shape

To investigate the effect of the shape of a features machined into the section, which have been designed to simulate cracks

- Feature Width

To investigate the effect of the width of machined features

#### *Cross Section Geometry*

Four samples were machined from SS316, each with cross sectional area of  $100\text{mm}^2$  and a length of 55mm. This area was chosen as it matches the work done on square cross section samples measuring 10mm x 10mm, 55mm

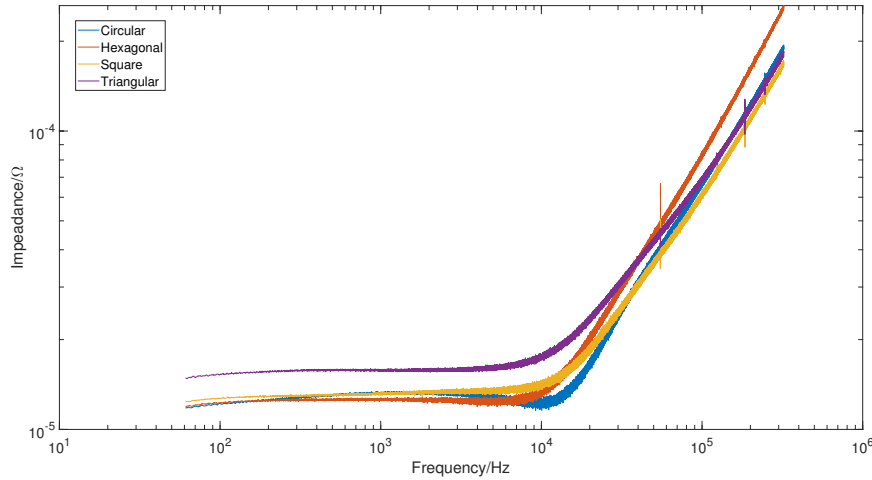


Fig. 6.2: Impedance Plot - Geometry Samples

long. The geometries chosen were, square, circular, hexagonal and equilateral triangle. For all this work, as with all the other square cross section experiments, the current is input on the same apex as the measurement was taken. As these samples are austenitic the frequency was swept up to 250kHz, sampling from quasi DC to a high frequency AC thin skin condition.

Plots of the impedance data and impedance data scaled for wire separation can be seen in figs. 6.2 and 6.3 respectively, the wire separation was measured using a Nikon SMZ1000 microscope after the experiment. It can be seen that the error introduced by the user welding the wire does make some difference to the measurement but this is mainly seen in the low frequency DC dominated range and becomes much less significant as the magnitude of the signals increase. Even with this error differences in the gradients of the impedance plots can be seen and the error does not affect this.

### *Feature Shape*

Four different feature shapes were identified that could be manufactured in the workshop, drawings of these can be seen in fig. 6.5. 10x10mm square section steel bar was used so that the unfeatured section of the samples have the same cross sectional area as the geometry samples. As these samples were

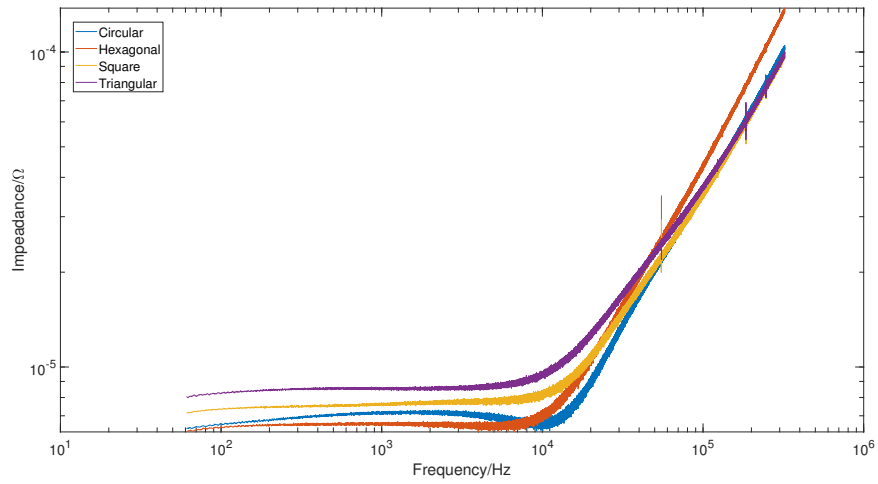


Fig. 6.3: Impedance Scaled for Wire Separation Plot - Geometry Samples

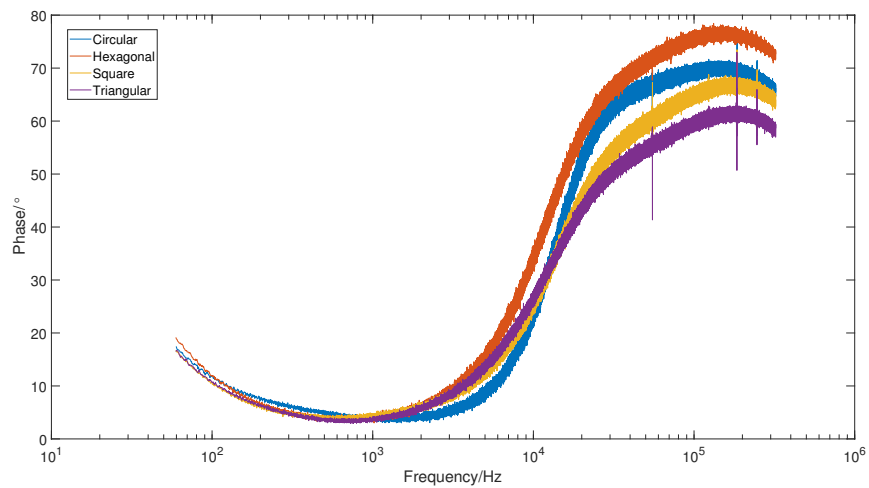


Fig. 6.4: Phase Plot - Geometry Samples

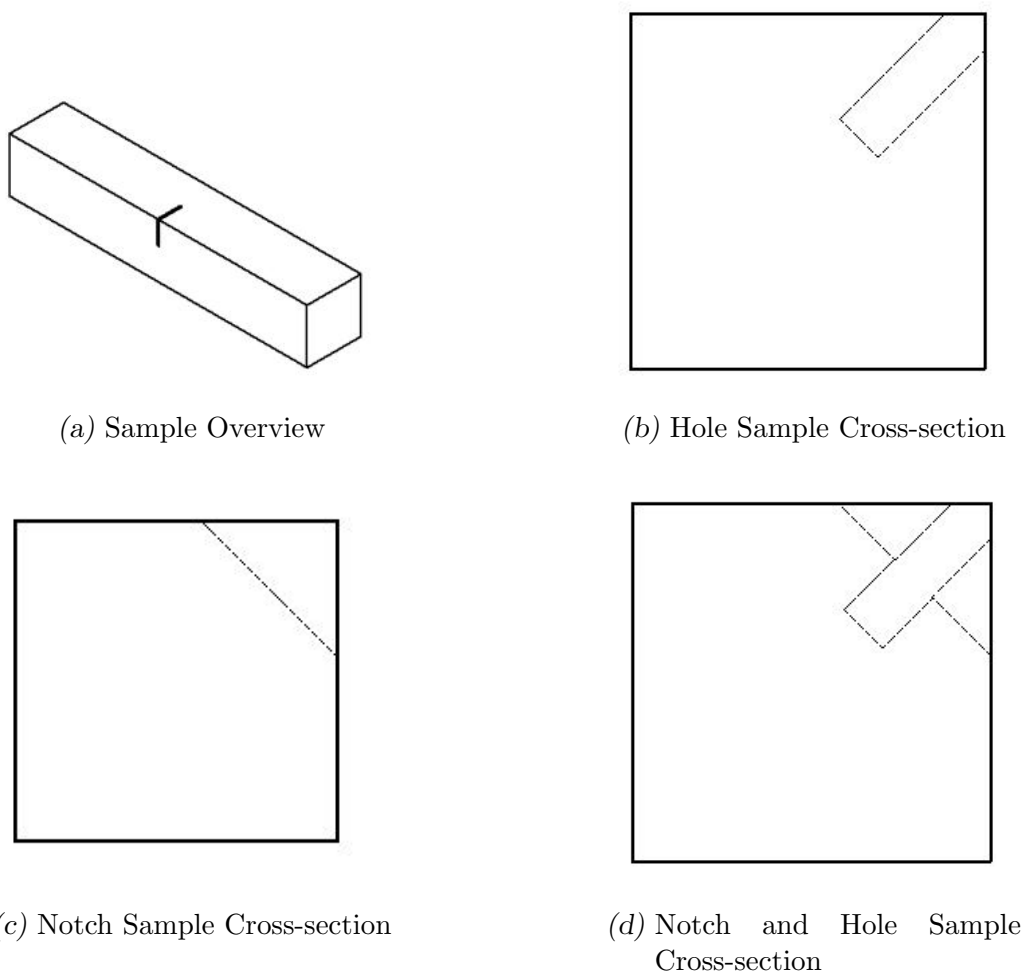


Fig. 6.5: Samples with simulated quarter circular and tunnelled cracks

made from a ferritic steel the frequency range needed to be reduced from the ones used in the SS316 samples, to ensure that the thick and thin skin ranges were covered. For reference it should be noted that in this material which equates to 1mm in a cylindrical conductor is in the region of 10Hz.

There is a clear difference in the impedance fig. 6.6 between the samples with a notch and those without, this can be seen throughout the frequency range. The notch makes a large change to the cross-sectional area of the sample at the sampling point, therefore it is clearly seen in the low frequency response. The effect of the hole is also seen both in the notched and un-

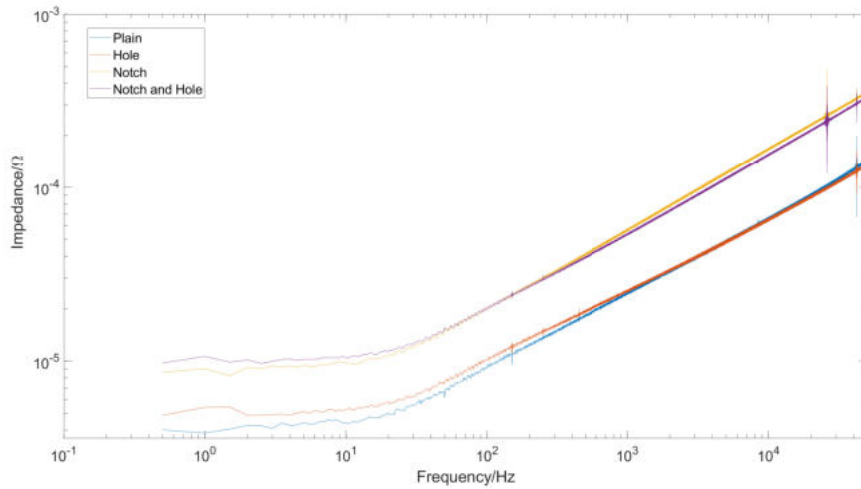


Fig. 6.6: Impedance vs Frequency Plot - Feature Samples

notched case, again in the low frequency range, due to the change in cross-sectional area. It can also be seen that the presence of the hole affects the gradient of the impedance response. The hole reduces the gradient of the plot, as the hole increases the impedance at low frequency this leads to the lines crossing in both the notched and un-notched cases.

The phase, fig. 6.8, also shows differences between the notched and un-notched samples, the pair of curves having differing shapes. The samples with the notch attaining a higher phase shift before the phase shift dropping more steeply at high frequency. Again there are differences between the samples with and without the hole in both notched and un-notched cases. The hole seeming to hold the phase shift down a little before coming back to follow the non-hole response at higher frequencies.

### *Feature Width*

Following on from the featured samples, specimens were manufactured out of the same grade ferritic steel. These all had a notch feature machined in one corner with varying widths, three of each width were manufactured. The aim of this was to understand the effect of the width of the feature on the measured values to understand how this work on machined samples may

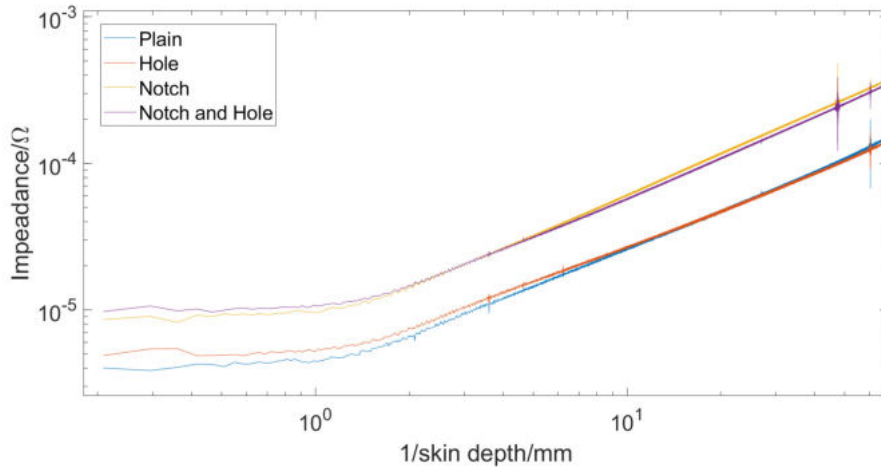


Fig. 6.7: Impedance vs Skin Depth Plot - Feature Samples

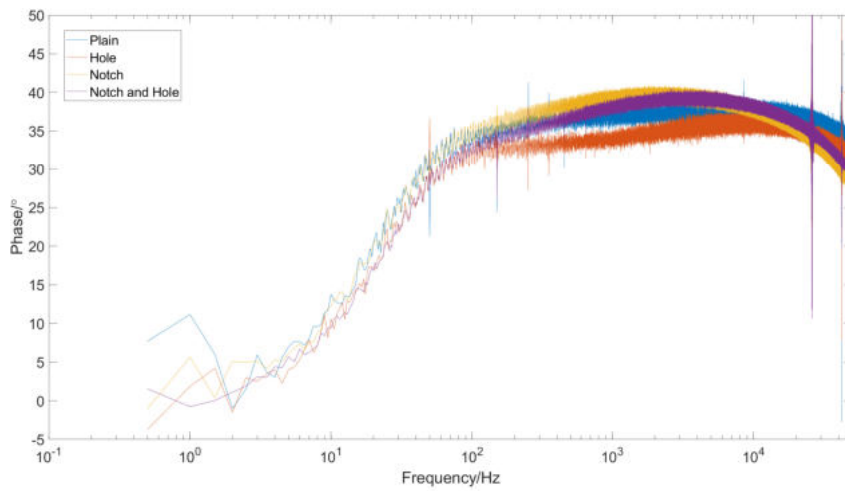


Fig. 6.8: Phase Frequency Plot - Feature Samples

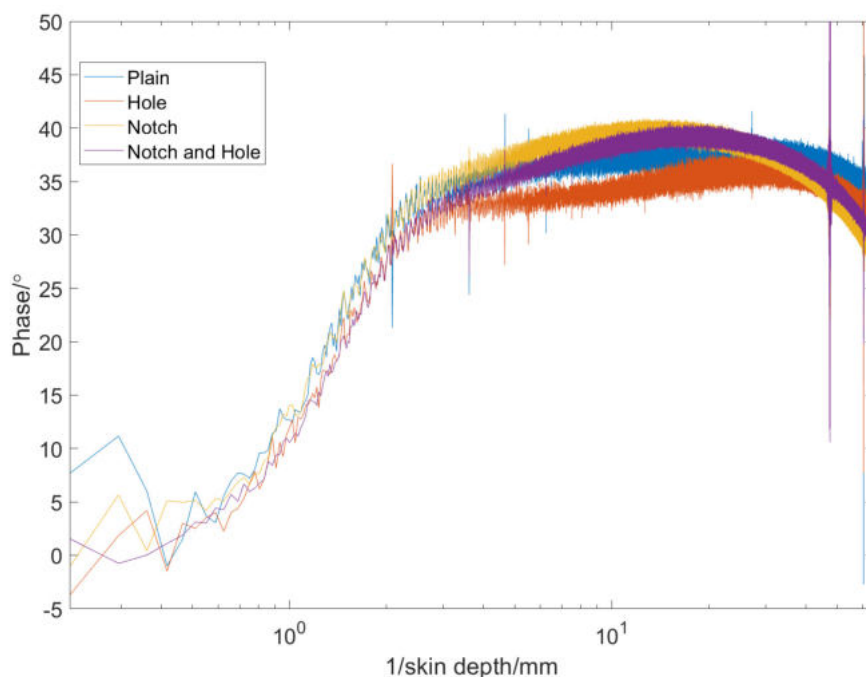


Fig. 6.9: Phase Skin Depth Plot - Feature Samples

relate to real world cracks which are very narrow. The two batches of samples were made to enable repeat experiments to be undertaken to understand the repeatability of this method, these are referred to as 'Na' and 'Nb' for the two batches and the following numbers indicate the width sizes 0.5, 1, 1.5 and 2mm.

The raw impedance data can be seen in fig. 6.10, there is some separation based on notch width for these samples. However, this is not due to the width of the notches but is related to the challenges with consistency in positioning of the measurement wires. This is made more difficult in these samples due to the differing notch widths affecting the judgement of the operator. fig. 6.11 shows the same data scaled for wire separation, which was measured using a microscope after the experiment. This shows that all the impedances follow the same trend, in gradient and magnitude with frequency. The phase fig. 6.12 also shows that the samples show the same trends of phase angle with frequency and this is not affected by the width of the notch.

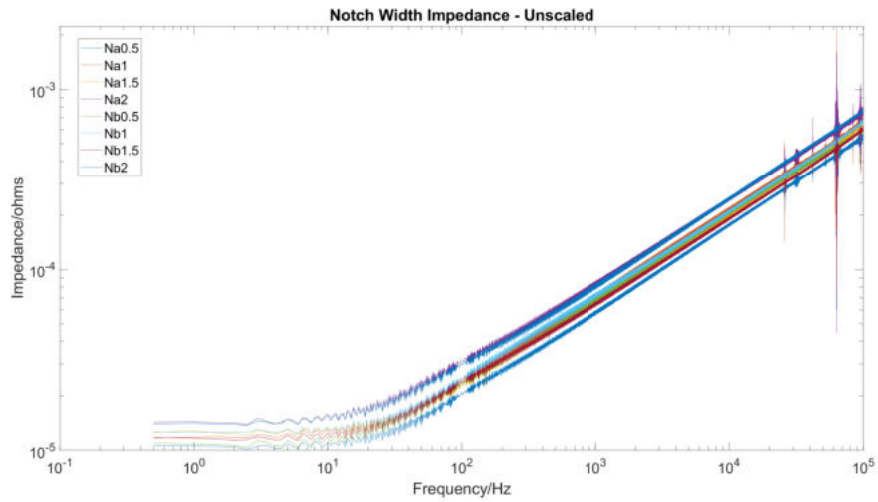


Fig. 6.10: Impedance Plot - Notch Width Samples Unscaled

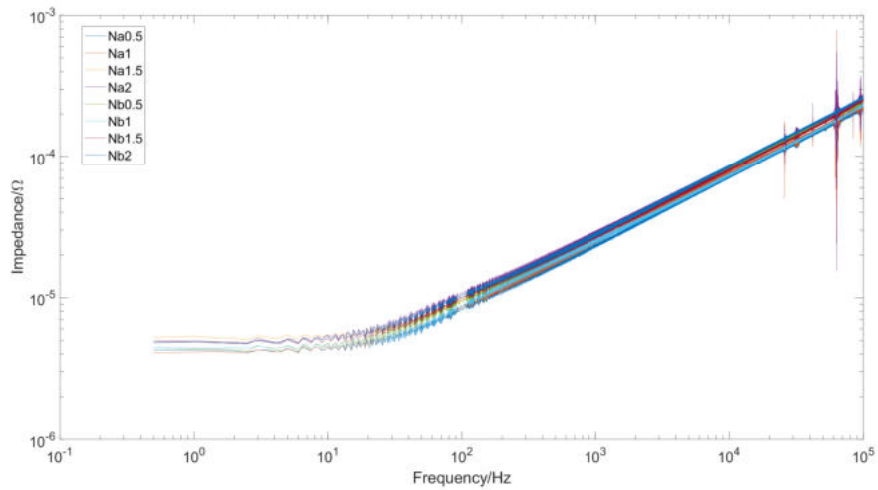


Fig. 6.11: Impedance Plot - Notch Width Samples Scaled

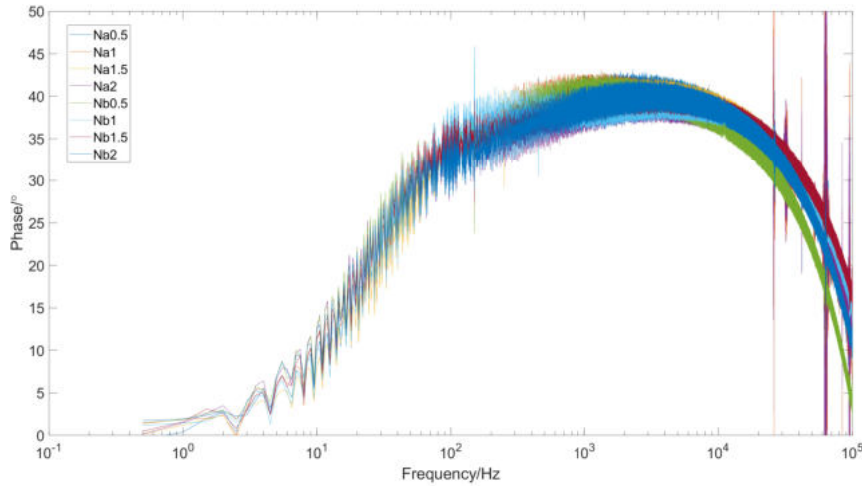


Fig. 6.12: Phase Plot - Notch Width Samples

### 6.3.2 Resistivity Calculation

With regard to the constant cross-sectional area samples it is possible to make a simple DC approximation knowing the electrical properties of the material, distance between the measurement points eq. (2.4). At low frequencies the current can be considered effectively DC so the bar has uniform current flow across the cross-section and the whole of the cross-sectional area is able to carry current. At higher frequencies where the skin depth is less than the effective diameter of the sample, the sample can be considered as a tube with a wall thickness equal to the skin depth. The skin depth can be calculated at a range of frequencies and therefore the effective wall thickness is known. By multiplying the skin depth with the circumference of the sample the effective cross sectional area can be calculated, at low frequencies this is greater than the real cross sectional area for these the cross sectional area is set to the real value ( $100\text{mm}^2$ ). When the skin becomes sufficiently small to give a theoretical area less than  $100\text{mm}^2$  the theoretical area is used. Using these areas, and considering the distance between the measurement points to be 2mm, eq. (2.4) can be used to calculate the voltage drop between two points, a plot of this can be seen in fig. 6.13. The voltage remains the same until the point at which the skin depth becomes significant, this onset is different

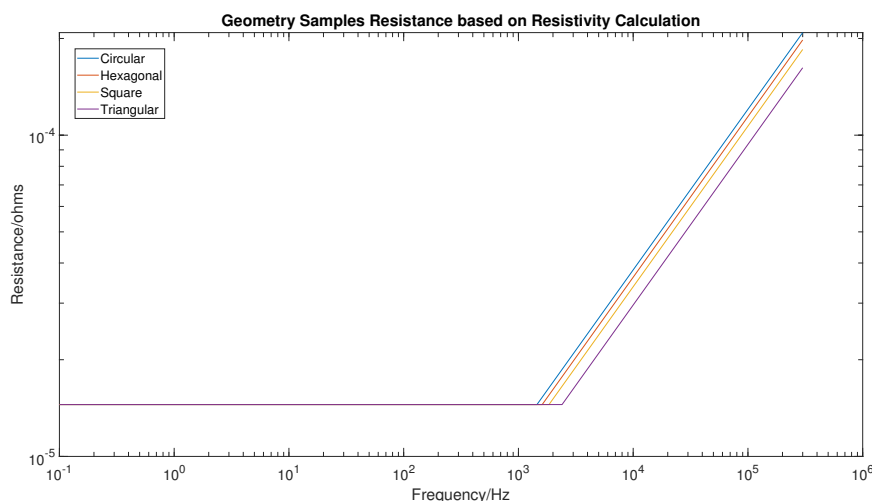


Fig. 6.13: Resistivity Calculation Plots - Geometry Samples

in line with the circumferences of the samples, once this point is reached the voltage increases as would be expected due to the reducing skin depth. This results in the voltage being controlled by the circumference of the sample.

This was also applied to the Feature Samples, in this case the effective cross sectional area and circumference was calculated based on a slice at the feature location. As the features remove different amounts of material from the effective cross section the DC response is different between the samples, whereas in the geometry samples the cross sectional areas are all  $100\text{mm}^2$ . It should also be noted that the material used for these samples is a ferritic steel so the onset of the thin skin is at a much lower frequency. Plots of these calculations can be seen in fig. 6.14

In both the experimental data and calculated resistivity plots for both the geometry and feature samples, the knee point for the switch from quasiDC to AC type behaviour is similar in the experimental and calculated response, although the calculated data shows the knee point at a slightly lower frequency than is seen experimentally. Also the magnitudes with frequency also show a good level of similarity, with increasing frequency. In the geometry experimental data it can be seen that the DC response for all samples is not the same, which is lost in the calculation. Also the DC approximation misses

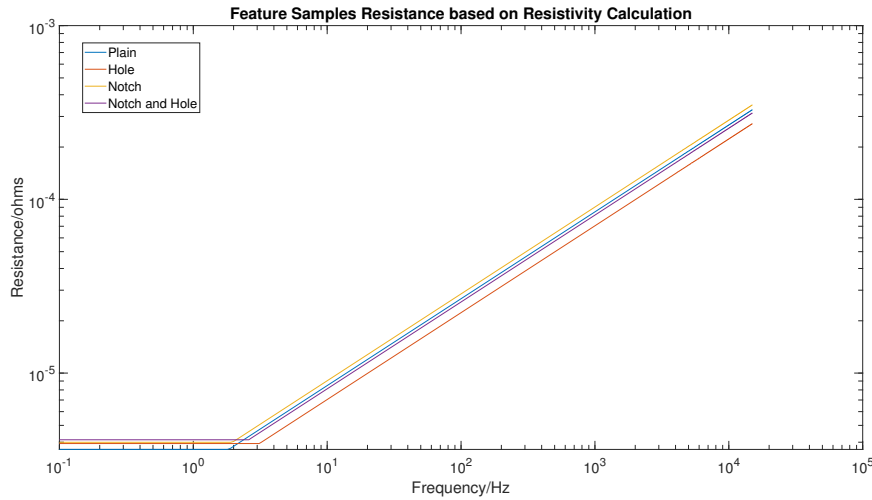


Fig. 6.14: Resistivity Calculation Plots - Featured Samples

a lot of the subtlety in the gradient changes in the geometry samples. In the case of the feature samples there are significant errors mainly due to the calculation of the circumference of the samples, for example the significant perimeter of the hole feature pushes the knee point to higher frequency.

## 6.4 Discussion

### 6.4.1 Initial Trials

Initial work with the Matelect equipment shows a variation of response related to the severity of the apex, however it is not clear that there is the theoretical DC response at low frequency. Until the input signal reaches a level where the skin depth is in the region of half the effective diameter, it is expected that all the cross section samples would perform the same. This was not seen in this work, however some relationship to the shape was seen. With this being a proprietary piece of equipment it is not clear exactly how the  $0^\circ$  and  $90^\circ$  signals are calculated or if there is any lag in any of the amplifiers, so it is not possible to diagnose the source of this unexpected result. It should be noted that this is not a failing of the equipment, just that this is extending it to a usage that was not necessarily envisaged by the

manufacturer.

#### 6.4.2 *Advanced Alternating Current Potential Drop*

In this work using the advanced ACPD equipment developed in this project care was taken to ensure that the true signals could be recorded without undue disturbance from the amplifiers. In this all the samples exhibit the DC response at low frequency and an increase in impedance is only seen at frequencies over the expected value of skin depth linked to the effective diameter. In both the Geometry and Feature samples the knee point on the impedance plots are at higher frequency than may be expected due to the effective diameter and in the Resistivity Calculations, in both cases the knee happens at a skin depth of about 1mm. It should be noted the deviation in the phase plots happens at a lower frequency than is seen in the impedance plots. Therefore it can be seen that once the skin depth is less than half of the effective diameter, a response is seen but the phase is more sensitive to this.

#### *Geometry Samples*

All the samples give a similar shaped curve in both impedance and phase angle. In the impedance data the plateau DC dominated region finishes at around 10kHz which equates to around 1mm skin depth, the phase response moves away from the in phase DC response at around 1100Hz which is approximately 3mm skin depth. There may be some response due to skin depth of 5mm as this is half the effective diameter of the sample, however this is not clearly seen. There can be seen that there is also a phase shift at very low frequency, which does not match up with the simple DC resistive effect. It is not clear why this should be and it is not seen in other the other material tested here, the ferritic steel used for the feature samples, this is a matter to be considered in further work.

It can be seen that there are differences which follow the 'severity' of the apex, this is the angle of the surfaces coming together at an apex, circular is nearly zero and the triangular is 60 degrees. The differences are not in raw

values but in the shape of the impedance and phase plots. It can be seen in the impedance plots, as the apex becomes more severe the gradient on the portion after the knee reduces. Also, in the phase plots there is a depression in the square and triangular samples from around 11 kHz to 100 kHz when compared to the hexagonal and circular samples with less severe apexes.

There is also a difference in impedance at low frequencies, this is not expected as in this range the impedance should be purely resistive. The circular and hexagonal samples are very similar and again the deviation is in line with the severity of the apex. Therefore this can be attributed to a non-uniform current flow towards the apexes.

The errors in the work of the operator was also considered, the element solely on the operator is wire placement and welding. The input wires can easily be placed in repeatable positions due to the end of the sample giving a good reference, it can be considered that the operator can place these with an accuracy of 0.5 mm which is 1 % of the total 55 mm length of the sample which is an acceptable error. For placement of the measurement wires the operator needs to mark the sample and line up the wires, to understand the variance in this the measurement wire separations for all the Geometry samples were measured. On average there was a 7 % error with reference to the 2mm separation in these with a maximum error of 15 %. Given the possible significance of the error in the measurement wire placement a correction factor was applied to the impedance data, the corrected data can be seen in fig. 6.3. This was not applied to the phase plot, fig. 6.4, as wire separation is not relevant as the gap between the measurement wires will only affect the magnitude not the time at which it occurs. This correction does make some difference to the low frequency values, however as explained above the significant differences are at higher frequencies where the real signal is significant and the key differences are in the shape of the plot not the absolute values.

*Feature Samples*

It can be seen in the impedance data, figs. 6.6 and 6.7, that there is a significant difference between the samples contacting a notch and those not. This is due to the notch significantly reducing the effective cross-sectional area giving the DC response and the increased path length resulting in a higher potential drop in the AC range. The response to presence or not of the notch feature follows the expected response of any DCPD or ACPD system. It can be seen that in the low frequency range the hole also increases the impedance as would be expected due to the further reduced effective cross-sectional area, the effect of the hole is less than that of the notch as it has a smaller area, the notch removes  $9 \text{ mm}^2$  whereas the hole only removed  $2.5 \text{ mm}^2$ . It can also be seen that the difference between the notch and the notch and hole sample is less than the comparison between the plain and hole samples, this is due to  $3/5$ th of the hole being within the notch in the notched samples.

There is a smooth transition between the DC and the AC conditions, which starts at a skin depth of approximately 1mm. If a uniform skin on a square cross section is considered this equates to about a  $40\text{mm}^2$  conductive area, 40% of the total area. It is likely that there will be a small effect from a skin depth of 5mm as this is half the effective diameter of the sample however due to the slight effect and minimal amount of data recorded at low frequency this is not clear and this effect is only seen from a skin depth of 1mm.

It can be seen that as the frequency increases the presence of the hole in both notched and un-notched samples has an effect. At high frequencies the impedance measured in the samples with the holes are below that of the samples without the holes, which is opposite to a simple crack size potential drop analogy. This demonstrates the sensitivity of this technique to the feature shape. To draw a clear comparison of the shape difference, the point of crossing of the two curves can be considered. Notch and Notch and Hole samples cross at a skin depth of 0.79mm and the Plain and Hole samples cross at a higher frequency equating to 0.01mm skin depth. It can be considered that the presence of the hole is masked at thin skin depths by the presence

of the notch so its presence is only 'seen' at the higher skin depth. This demonstrates that the shape of a feature, not just its area or length, can be detected by looking at the impedance at a wide range of frequencies from quasi-DC to a very thin skin AC conditions.

The differences in feature shape also affect the phase response, see figs. 6.8 and 6.9. In this the change from the in phase DC response is seen at a skin depth of around 6mm, in the region of half the effective diameter of the sample. This shows that there is an effect from around this point and that the phase response is more sensitive to this.

Again the two samples not containing the notch show a similar shape to each other as do the two samples without. Also the presence of a hole affects both curves giving a reduction in the phase shift from around 100 to 1000 Hz. This shows that there is sensitivity to feature shape in both the impedance and the phase relationships.

#### *Feature Width*

This work was centred on understanding the effect, if any, of the width of the feature and the sample to sample repeatability. If feature width affected the measurements then the differences seen between the Feature Samples may not be purely based on the 2D shape of the feature but also its width.

In this it can be seen in fig. 6.12 that there is no significant difference in the phase plots, there are not any changes in the phase as with the presence of the holes in the Feature Shape samples. The shape of these curves also follow the shape of the notch and notch and hole samples, however the data plotted goes to high frequency in these tests so the curve down continues down further than that shown in the Feature Shape figures.

Due to differing width of the notches it was not possible to control the separation of the measurement wires as well as in most of the other samples, this led to errors in the impedance plots. To rectify this all the wire separations were measured and a correction factor applied. With these factors applied it can be seen that there is very little variation between all the impedance plots, fig. 6.11.

In summary very little variation was seen in these samples, it should also be noted that repeats were undertaken for all the samples. This shows good repeatability sample to samples and that the variation of features up to 2mm in thickness does not affect the shape of the curve in either impedance or phase.

## 7. DISCUSSIONS

The work presented in this thesis reports the development of several tools that allow users to monitor non-uniform crack growth parameters (crack shape and depth) during cyclic testing. Methods for promoting crack growth in uniaxial specimens in both LCF and TMF conditions have been developed, a new method of designing beach marks has been developed and an advanced ACPD system has been made and tested on some samples with known crack type features.

In the mechanical testing on the two materials, SS316 and RR1000, it was seen that the newly developed testing facility at The University of Nottingham using fixed frequency ACPD for crack measurement in the induction furnace worked well in both LCF and TMF conditions. Electrical pickup, which was observed to be around two orders of magnitude larger than the ACPD signal, was overcome by filtering. This was challenging as the level of rejection on the amplifiers needed to be very high while maintaining the sensitivity for the very low voltage measured across the crack.

Much of the mechanical testing presented here was conducted at elevated temperature. These testing conditions were achieved using an induction furnace on the test frame, however it was observed that this device generated a broad band interference (related to the method employed for power modulation in the thermal control system). The nominal input frequency from the furnace is in the region of 170-190 kHz, if this was a pure frequency then a band stop filter only eliminating this frequency range could be used. Due to the use of pulse width modulation (PWM) in the furnace system however, many other lower frequency components were noted in impedance waveforms, leading to aliasing at a wide range of frequencies down as low as 5 kHz. To overcome this a low pass filter was employed, with a cut-off

---

frequency of 500 Hz. This gives good rejection of the signals from the furnace however limits the ACPD system in the low frequency (pseudo-DC) range. Implementation of the advanced ACPD system over a broad frequency range will require the adoption of a different induction furnace system that outputs AC signals over a limited frequency range (thereby allowing for the use of a band stop filter). This could be achieved by looking to a different commercially available system or by manufacturing a bespoke solution. The benefits of these would need to be assessed based on the availability of commercial systems and the desired level of control over the input frequency. The smaller frequency band used by the induction furnace would be beneficial and enable a large frequency range to be usable by the ACPD.

Typically in induction heating the induction circuit resonates giving a high efficiency system only requiring a small input of power minimising losses. The frequency of this resonance is normally automatically tuned by the furnace taking account of the inductance of the load, which is determined by the coil size and geometry and the material being heated (recall that the electromagnetic properties of materials are typically temperature dependent). For example, if a material is heated beyond its Curie Temperature (the temperature where a material may lose its permanent magnetic properties) the dynamics of the system (i.e. the relationship between input power and observed specimen temperature) changes. Autotuning to the resonance frequency gives higher efficiency at the expense of frequency control. This benefit and cost will need to be considered in the implementation of the technique in an induction field.

In the testing a range of crack shapes were observed. SS316, for example, produced nearly quarter-circular cracks in almost all cases. RR1000, on the other hand, showed a range of non-quarter-circular and out of plane cracks. Low fixed frequency ACPD system was able to measure the crack area, as the low frequency AC meant that the sample was saturated with current flow as with DCPD. However there was no sensitivity to the different crack shapes or non-planar nature.

Beach marking was used in the verification of the fixed frequency ACPD, employing the typical approach utilising experience and judgement. In this a

---

change in the loading regime results in a mark on the fracture surface. This approach is typically haphazard and is material, temperature, and loading specific leading to unreliable results. In spite of this unreliable nature of this technique, it was successfully implemented to generate marks to prove the reliability of the fixed frequency ACPD using SS316, using holds at mean load and at a temperature of 600 °C. This was effective but was only seen at 600 °C and could not be replicated at other temperatures or to the same level in RR1000.

In the search for high quality crack shape measurement, a new method was devised. In this approach different crack growth rates were induced by applying two different R-ratio waveforms, the larger amplitude waveform being the test waveform and the smaller amplitude waveform being interspersed in the main test to generate beach marks. To enable this approach, knowledge of crack growth rates for each constituent waveform is required. Once this is known incremental crack growth per cycle can be calculated and projected beach marks estimated. During the exploration of the technique it was discovered that the initial crack length was key to accurately predicting the crack growth and hence beach mark formation. A small error in the initial position is amplified as the error accumulated cycle on cycle leads to significantly inaccurate predictions at high crack lengths. The error was found to be in the slight tunnelling that was seen in the pre-crack. The initial crack length was measured on the surface of the sample with a travelling microscope, the measurement was accurate however the cracks were slightly longer in the centre compared to at the edge. By measuring multiple failed samples the degree of this tunnelling was characterised and scale factor applied. With this factor applied a fracture surface with a user defined pattern of test and beach marks was possible and able to be repeated. If ACPD or DCPD were used to measure the pre-crack this correction factor would not necessarily be needed, however if optical methods are used then it is likely that this would be needed in most materials as slight tunnelling is often seen in these tests. To best utilise the testing machines it is much more convenient to instrument the samples for ACPD after the pre-cracking on the servo-hydraulic machine. The pre-cracking on the servo-hydraulic machine

---

and testing on the servo-electric machine enabled the pre-cracking to happen quickly at a high loading frequency, there was also the added benefit that another test could be undertaken at the same time on the servo-electric. Not moving the sample with measurement in place from the servo-hydraulic to the servo-electric machine, also reduces the number of tests affected by wire breaks as the instrumented sample is handled as little as possible.

The induced beach mark method was successful and given that the crack growth rates of the test and beach mark wave forms gave good agreement, it can be concluded that the crack growth rate in one regime was not affected by the previous loading regime. If the previous regime had induced significant damage ahead of the crack tip, there could have been a higher crack growth in the next stage. In the same way as if some work hardening was induced in one regime this could then slow the growth in the next stage through the stronger material. In this work no effect was seen in the crack growth rates, however it should be noted that in the beach mark tests at 525 °C the crack remained in plane throughout the test and in the tests without the beach marks some non-planar growth was seen which suggests some effect of the changing of loading regime. However, in other materials and loading conditions this could be a limitation of this technique, with the measurement affecting crack growth rates and the overall result of the test.

With a view to making a completely independent measurement the advanced ACPD system was developed. To do this investment and development of equipment and procedures was key. Suitable digital to analogue and analogue to digital converters needed to be sourced and signal input and measurement amplifier sourced and developed. Development of suitable shielding was needed to ensure that the signals measured were accurate measurements of the voltage between the two points of interest and not affected by external effects. This was of particular importance in this multiple frequency system in comparison to a fixed frequency system. In a fixed frequency system any pickup from the input signal on the measurement wires can be considered constant, however in the variable frequency case this is not true. At higher frequencies higher drive voltages are needed, this gives rise to changing EM field which can be measured on unshielded cables, which has been shown to

be significant in the range of interest.

Data generation and recording equipment was sourced from National Instruments, suitable rate and synchronous data capture is key. The rate needs to be sufficiently higher than the Nyquist criterion (i.e. sampling frequencies need to be at least twice the highest frequency element of the signals). To satisfy this a sampling rate of 500 kHz is sufficient. However, to ensure there was some additional allowance in the system and allow for potential amplifier roll off, the National Instruments unit chosen is capable of recording at 4 MHz. Coupled with this the data output rate had to also be sufficiently high to give a smooth sine wave and therefore not introduce distortions, in this case the unit specified can output at 2.5 MHz. The large amount of data caused a data flow problem in the data acquisition system, which was overcome with the addition of more RAM.

Given that both the input current and the voltage needed to be measured and phase relationship of these signals was of interest the acquisition of the signals needed to be synchronous. Many data capture systems multiplex the acquisition, sampling each input sequentially so the data recorded on each channel is not sampled at the same time instant. At low rates or in situations where the phase of the signals is not important this works well, however this would not be suitable in this application. The National Instruments PXI system was identified as this is designed to run in this mode with samples on all channels being taken at the same time.

Wiring layout has been shown to be key in producing a robust ACPD system. Control of the input cables moving from flexible wires to steel bars ensured good connections and repeatable current injection points. On a testing machine these features would be built into gripping arrangements to ensure repeatability. Placement of the measurement wires was controlled by marking the samples at the 2mm separation, just in from the edge and welding adjacent to these marks. A range of approaches were trialled to control the level of pickup on the measurement wires. These included creating a bridge to move the flux around the wires without introducing voltages in them, blocking these fields with a conductive box, and passing any absorbed energy to ground. The latter was found to be the most effective but all yielded

positive results, reducing the electrical pickup by an order of magnitude in both the bridge and block cases and reducing still further with the full box. Further work should look into the shielding when moving to the test machine, given the location of the specimen and the compilation of heating the specimen.

The novel variable frequency ACPD system was designed, assembled and shown to address many of the challenges demonstrated in the other work undertaken in this project. Sensitivity to specimen cross sectional geometry and feature shape have been shown. When trialled on bench top samples this technique was shown to be able to detect variation in cross section geometries. Results varied systematically between circular, hexagonal, square, and triangular cross sections, with the number of vertices in a cross section being inversely related to the measured frequency dependent impedance. Classical theory of skin effect would suggest that the change in geometry would only be significant in relation to the change in perimeter of the samples, the samples with smaller perimeters would expect to exhibit higher voltages but the shape of the response would be the same. However this was not seen to be the case, as the measurements were taken at the aspect of the sample, the severity of the apex was shown to drive the response. Tests conducted on samples with known feature geometries highlighted that the shape of the feature influences ACPD readings. Changes to ACPD readings are not purely dependent on changes to current path length, as is often assumed in ACPD studies. The samples with the hole, used to simulate a tunnelled crack, showed a change in behaviour with frequency driving the impedance curves for the samples with holes to cross the impedance curves of the samples without. A sensitivity between phase response and feature geometry was also observed. This was seen in both the notched and un-notched samples. The frequency at which the two plots cross was affected by the presence of the notch. This shows that local depth of the feature in the hole case and the breadth of the feature in the notch case affect the single voltage measurement. Both the sensitivity to geometry and feature shape can be linked to the non-uniform current flow as an apex is approached or around features. This non-uniform current flow results in the non-uniform voltage field that is at the surface, this is what has

---

been measured in this study at one point as in standard PD measurement. With this technique, there is no need to interrupt a test to beach mark the sample when using this technique, the sweep can be achieved in two seconds at the peak of the loading cycle.

The fracture mechanics beach marking method has been shown to be a useful tool to measure crack shape. This may be best implemented in situations where instrumenting a sample with the advanced ACPD may not be possible or desirable, such as in extremes of temperature, in the presence of atmospheric corrosives, in conductive liquids or in other harsh environments. The method could also be applied in situations where complex specimen geometries are required, such as when crack growth monitoring is required in samples that may mimic real components. In such cases, it may be impractical to instrument the areas that experience the highest local stress and this technique could be used to measure crack growth after the test.

## 8. CONCLUSIONS

The work presented here falls into three main themes, materials testing to determine conventional crack growth rates in two materials, the development of a technique to reliably pattern a fracture surface with beach marks and the development of an advanced swept ACPD system.

The materials testing has shown that temperature and loading frequency affect the crack growth rate in SS316. Temperature effects can be linked to the temperature at the maximum tensile load, higher temperatures at this point giving higher crack growth rates. Loading rate dependency is different depending on the temperature, higher temperatures where creep and therefore time at load is significant show a higher crack growth rate at lower frequency but this is reversed at low temperature. In the RR1000 the crack growth rates are in two clear bands, tests that have maximum load at 750° and those that don't, showing the reduction in properties at this higher temperature. This is also a range of crack shapes exhibited in this material, non-quarter-circular at 750° and non planar being seen at other temperatures.

Beach marking has been shown to be a useful tool in understanding crack growth. This has been used as a calibration tool and a novel method developed to define patterns of marks. Use of creep holds has given a good insight into the performance of the fixed frequency ACPD system. The use of fracture mechanics to calculate the crack growth in both the test waveform (R-ratio = 0) and the beach mark waveform (R-ratio = 0.7) has been developed and shown to give accurate and repeatable marks at the operator's choosing with an error of 2.

The novel advanced ACPD system has been developed and shown to be able to resolve differences in cross-sectional shape of samples and in the shape

of machined features which mimic cracks. Differences can be seen in both the impedance and the phase response at varying frequencies, with further work this will enable the monitoring of crack shape in real tests without the need to interrupt these with beach marks which can affect the crack growth.

In summary, this work has shown:

- The limitations of conventional ACPD crack measurement, relating to an insensitivity to crack shape and non-planar growth.
- A technique to design and implement user controlled beach marking has also been developed and tested on a range of bench samples.
- Advanced ACPD system has been developed and shown significant sensitivity to feature and sample shape.

## 9. FURTHER WORK

Further work to continue this will centre around the further understanding of the non-uniform current flows and the resulting voltages and the implementation of this technique in LCF and TMF conditions.

Further experimental work with other feature shapes will further explore the effect of the shape on voltages exhibited on the surface of the sample. The work on feature width has shown this the feature width has little effect on the resulting voltages, so such techniques as electrical discharge machining (EDM) using a range of shaped electrode could be used to generate unusual shapes in the samples. Also non planar features could be investigated to test the sensitivity to the crack moving out of plane.

Computational modelling could be used to understand the current flow around the shapes used in this work and in the more complex shapes suggested above. This current density can then be used to generate a map of expected voltages on the surface of the sample. The experimental work could then be extended to measure voltages at various points on the surface of the samples to make point measurements to prove the model.

The implementation of the advanced ACPD technique in LCF and TMF will need to consider a number of challenges. As explained previously, the induction furnace on the current test machine at the University of Nottingham give broadband interference which swamps any signals that are generated by the ACPD system. This could either be overcome by switching the furnace off for the duration of the measurement, this may not be possible as the furnace takes a number of seconds to de-energise and re-energise and in this time the sample will cool. Also this instability would upset the control system, which could then lead to significant overshoot on restart. This lack of thermal control would therefore affect the test. The more plausible solution

---

would be to source or develop an alternative heating method. This could be a different induction furnace with a pure output frequency or it could be another technique such as radiant lamps. The disadvantage of radiant lamps for the heating and cooling rates are significantly less than with induction heating therefore limit the test envelop of the system

If induction heating is continued to be used there will need to be thought given to the filtering of the signals, this may be by way of a band pass filter. This would be a filter that blocks signals in the frequency range used by the induction furnace, so the tighter the band on the output frequency of the furnace the better, as this will maximise the frequencies that are available to the ACPD measurement.

In the advanced ACPD work it has been shown that shielding the measurement wires is key to eliminating pickup from the input current and other external sources. In the implementation of this in the high temperature environment of the testing machine this will need to be considered and the aluminium box used in the bench tests will melt. Possible solutions could be a small ceramic box coated internally with a high melting point metal, this could be achieved by means of PVD or by manufacturing a thin metallic internal skin. This approach could also be reversed, using a metal box with a thin ceramic or glass insulator on the exterior of the box to insulate it from the sample, if the metallic box touched the sample this would provide an addition conductive path thus affecting the measurement. The metallic box will probably be the better option as this will be more resilient as it is less likely to fracture when compared with ceramic. A very thin glass cover slip or the like could be used as a high temperature insulator, which would minimise the amount of wire unshielded and could be easily replaced in between tests should it break.

## BIBLIOGRAPHY

- [1] C. J. Hyde, T. H. Hyde, W. Sun, and A. A. Becker, “Damage mechanics based predictions of creep crack growth in 316 stainless steel,” *Engineering Fracture Mechanics*, vol. 77, pp. 2385–2402, aug 2010.
- [2] C. J. Hyde, W. Sun, and T. H. Hyde, “An investigation of the failure mechanisms in high temperature materials subjected to isothermal and anisothermal fatigue and creep conditions,” *Procedia Engineering*, vol. 10, pp. 1157–1162, jan 2011.
- [3] A. A. Saad, W. Sun, T. H. Hyde, and D. W. J. Tanner, “Cyclic softening behaviour of a P91 steel under low cycle fatigue at high temperature,” *Procedia Engineering*, vol. 10, pp. 1103–1108, jan 2011.
- [4] C. Hyde, W. Sun, and S. Leen, “Cyclic thermo-mechanical material modelling and testing of 316 stainless steel,” *International Journal of Pressure Vessels and Piping*, vol. 87, pp. 365–372, jun 2010.
- [5] T. M. Buss and C. J. Hyde, “Cyclic thermomechanical testing of 316 stainless steel,” *Materials at High Temperatures*, vol. 32, no. 3, pp. 276–279, 2015.
- [6] Wikipedia, “United Airlines Flight 328,” 2021.
- [7] R. Hooke, “Lectures De Potentia Restitutiva, or of Spring Ezplaining the Power of Springing Bodies,” p. 56, 1678.
- [8] T. Young, “A course of lectures on natural philosop.pdf,” 1807.
- [9] M. F. Ashby and D. R. D. R. H. Jones, *EngineeringMaterials 1: An*

- 
- Introduction to their Properties and Applications.* Butterworth Heine-  
mann, 1996.
- [10] W. Schlitz, “A History of Fatigue,” *Engineering Fracture Mechanics*,  
vol. 54, no. 2, pp. 263–300, 1996.
- [11] W. J. M. Rankine, “On the Causes of the Unexpected Breakage of  
the Journals of Railway Axles; and on the Mean of Preventing such  
Accidents by Observing the Law of Continuity in their Construction,”  
*Journal of the Franklin Institute*, vol. 36, pp. 178–180, sep 1843.
- [12] F. Braithwaite, “On the Fatigue and Consequent Fracture of Metals,”  
*Journal of the Franklin Institute*, vol. 58, pp. 200–201, sep 1854.
- [13] A. Griffith, “The phenomena of rupture and flow in solids, Grif-  
fith.pdf,” *Philosophical Transactions of the Royal Society of London*,  
vol. 221, pp. 163–198, 1921.
- [14] G. Irwin, “Analysis of stresses and strains near the end of a crack  
traversing a plate,” *Journal of Applied Mechanics*, vol. 24, pp. 361–  
364, 1957.
- [15] P. Paris, M. Gomez, and W. Anderson, “A Rational Analytic Theory  
of Fatigue,” *The Trend in Engineering*, vol. 13, pp. 9–14, 1961.
- [16] J. R. Rice, “A Path Independent Integral and the Approximate Analy-  
sis of Strain Concentration by Notches and Cracks,” *Journal of Applied  
Mechanics*, vol. 35, pp. 379–386, 1968.
- [17] Cohen, W. S. Farren, W. J. Duncan, and A. H. Wheeler, “Report of  
the Court of Inquiry into the Accidents to Comet G-ALYP on 10th  
January, 1954 and Comet G-ALYY on 8th April, 1954,” tech. rep.,  
Ministry of Transport and Civil Aviation, 1955.
- [18] R. Piques, E. Molinié, and A. Pineau, “Creep and creep-fatigue crack-  
ing behaviour of two structural steels,” *Nuclear Engineering and De-  
sign*, vol. 153, pp. 223–233, jan 1995.

- 
- [19] X. Zhang, S.-T. Tu, and F. Xuan, “Creep fatigue endurance of 304 stainless steels,” *Theoretical and Applied Fracture Mechanics*, vol. 71, pp. 51–66, may 2014.
- [20] M. W. Spindler, G. Knowles, S. Jacques, and C. Austin, “Creep-Fatigue Behaviour of type 321 Stainless Steel at 650C,” in *HTMTC Symposium on Creep-Fatigue Crack Development*, 2014.
- [21] BSI, “Methods of Fatigue testing BS 3518-1 Part 1 : Guide to general principles,” 1993.
- [22] C. J. Hyde, “Thermo-Mechanical Fatigue and Creep of High Temperature Materials,” no. August, 2010.
- [23] A. Nagesha, R. Kannan, P. Parameswaran, R. Sandhya, K. B. S. Rao, and V. Singh, “A comparative study of isothermal and thermomechanical fatigue on type 316L(N) austenitic stainless steel,” *Materials Science and Engineering: A*, vol. 527, pp. 5969–5975, aug 2010.
- [24] M. Ramesh, H. J. Leber, K. G. Janssens, M. Diener, and R. Spolenak, “Thermomechanical and isothermal fatigue behavior of 347 and 316L austenitic stainless tube and pipe steels,” *International Journal of Fatigue*, vol. 33, pp. 683–691, may 2011.
- [25] K. Rau, T. Beck, and D. Lohe, “Isothermal, thermal-mechanical and complex thermal-mechanical fatigue tests on AISI 316 L steel-a critical evaluation,” *Materials Science and Engineering A*, vol. 345, no. 1-2, pp. 309–318, 2003.
- [26] A. Portiven and F. Le Chatelies, “Sur un Phénomène Observé lors de L’essai de Traction d’Alliages en Cours de Transformation,” *Comptes Rendus de l’Academie des Sciences, Paris*, vol. 176, pp. 507–510, 1923.
- [27] P. Rodriguez, “Serrated plastic flow,” *Bulletin of Materials Science*, vol. 6, no. 4, pp. 653–663, 1984.

- 
- [28] W. Karlsen, M. Ivanchenko, U. Ehrnstén, Y. Yagodzinsky, and H. Hänninen, “Microstructural manifestation of dynamic strain aging in AISI 316 stainless steel,” *Journal of Nuclear Materials*, vol. 395, pp. 156–161, dec 2009.
- [29] M. Ivanchenko, *Dynamic Strain Aging of Austenitic Stainless Steels and Ni Base Alloys*. PhD thesis, Aalto University, 2010.
- [30] M. Ivanchenko, Y. Yagodzinsky, U. Ehrnstén, W. Karlsen, and H. Hanninen, “Manifestations of DSA in Austenitic Stainless Steels and Inconel Alloys,” in *20th International Conference on Structural Mechanics in Reactor Technology*, pp. 1–9, 2009.
- [31] P. L. Raffo, “Dynamic Strain Aging During the Creep and Tensile Testing of a Molybdenum-Titanium-Carbon Alloy,” *Lewis Research Center*, no. April, 1969.
- [32] X.-L. Yan, X.-C. Zhang, S.-T. Tu, S.-L. Mannan, F.-Z. Xuan, and Y.-C. Lin, “Review of creep-fatigue endurance and life prediction of 316 stainless steels,” *International Journal of Pressure Vessels and Piping*, vol. 126, pp. 17–28, dec 2014.
- [33] J. Jones, M. Whittaker, R. Lancaster, and S. Williams, “The influence of phase angle, strain range and peak cycle temperature on the TMF crack initiation behaviour and damage mechanisms of the nickel-based superalloy, RR1000,” *International Journal of Fatigue*, vol. 98, pp. 279–285, 2017.
- [34] A. Pineau, “High Temperature Fatigue, A Comprehensive Review,” in *HTMTC/IOM3 CREEP-FATIGUE CRACK DEVELOPMENT SYMPOSIUM*, pp. 1–29, 2014.
- [35] R. Bill, “Micromechanisms of Thermomechanical Fatigue - A comparison with Isothermal Fatigue,” in *Fatigue at High Temperatures*, 1986.
- [36] D. Socie and B. Socie, “Thermomechanical fatigue made easy,” in *Fatigue 2007*, 2007.

- 
- [37] M. Whittaker, W. Evans, P. Hurley, and D. Flynn, "Prediction of notched specimen behaviour at ambient and high temperatures in Ti6246," *International Journal of Fatigue*, vol. 29, no. 9-11, pp. 1716–1725, 2007.
- [38] M. Kamaya, "Environmental effect on fatigue strength of stainless steel in PWR primary water. Role of crack growth acceleration in fatigue life reduction," *International Journal of Fatigue*, vol. 55, pp. 102–111, oct 2013.
- [39] T. Farragher, S. Scully, N. O'Dowd, and S. Leen, "Development of life assessment procedures for power plant headers operated under flexible loading scenarios," *International Journal of Fatigue*, vol. 49, pp. 50–61, apr 2013.
- [40] J. C. Maxwell, "On Physical Lines of Force," *Philosophical Magazine and Journal of Science*, vol. 21, 1861.
- [41] J. C. Maxwell, *A Treatise on Electricity and Magnetism*. Oxford: The Clarendon Press, 1 ed., 1873.
- [42] G. S. Smith, "A simple derivation for the skin effect in a round wire," *European Journal of Physics*, vol. 35, no. 2, 2014.
- [43] M. Mathew, K. Laha, and R. Sandhya, "Creep and Low Cycle Fatigue Behaviour of Fast Reactor Structural Materials," *Procedia Engineering*, vol. 55, pp. 17–26, jan 2013.
- [44] D. W. Kim, J.-H. Chang, and W.-S. Ryu, "Evaluation of the creep fatigue damage mechanism of Type 316L and Type 316LN stainless steel," *International Journal of Pressure Vessels and Piping*, vol. 85, pp. 378–384, jun 2008.
- [45] K. Obrtlík, J. Polak, M. Hajek, and A. Vasek, "Short fatigue crack behaviour in 316L stainless steel," *International Journal of Fatigue*, vol. 19, no. 6, pp. 471–475, 1997.

- 
- [46] S. C. Roy, S. Goyal, R. Sandhya, and S. Ray, "Analysis of Hysteresis Loops of 316L(N) Stainless Steel under Low Cycle Fatigue Loading Conditions," *Procedia Engineering*, vol. 55, pp. 165–170, jan 2013.
- [47] W. J. Mills and L. A. James, "Fatigue Crack Propagation Behaviour of Type 316 Stainless Steel at Elevated Temperature in a Vacuum," *International Journal of Fatigue*, vol. 10, no. 1, pp. 33–36, 1988.
- [48] M. N. Babu, B. S. Dutt, S. Venugopal, G. Sasikala, A. K. Bhaduri, T. Jayakumar, and R. Baldev, "On the anomalous temperature dependency of fatigue crack growth of SS 316(N) weld," *Materials Science and Engineering A*, vol. 527, pp. 5122–5129, jul 2010.
- [49] A. Nagesha, M. Valsan, R. Kannan, K. Bhanu Sankara Rao, V. Bauer, H. J. Christ, and V. Singh, "Thermomechanical fatigue evaluation and life prediction of 316L(N) stainless steel," *International Journal of Fatigue*, vol. 31, pp. 636–643, apr 2009.
- [50] S. Hong, "The tensile and low-cycle fatigue behavior of cold worked 316L stainless steel: influence of dynamic strain aging," *International Journal of Fatigue*, vol. 26, pp. 899–910, aug 2004.
- [51] S. Hong, K. Lee, and S. Lee, "Dynamic strain aging effect on the fatigue resistance of type 316L stainless steel," *International Journal of Fatigue*, vol. 27, pp. 1420–1424, oct 2005.
- [52] L. J. Meng, J. Sun, H. Xing, and G. W. Pang, "Serrated flow behavior in AL6XN austenitic stainless steel," *Journal of Nuclear Materials*, vol. 394, pp. 34–38, oct 2009.
- [53] A. K. Gupta, S. K. Singh, S. Reddy, and G. Hariharan, "Prediction of flow stress in dynamic strain aging regime of austenitic stainless steel 316 using artificial neural network," *Materials & Design*, vol. 35, pp. 589–595, mar 2012.
- [54] S.-g. Hong and S.-b. Lee, "Mechanism of dynamic strain aging and characterization of its effect on the low-cycle fatigue behavior in type

- 
- 316L stainless steel,” *Journal of Nuclear Materials*, vol. 340, pp. 307–314, 2005.
- [55] A. Nagesha, R. Kannan, G. Sastry, R. Sandhya, V. Singh, K. Bhanu Sankara Rao, and M. Mathew, “Isothermal and thermomechanical fatigue studies on a modified 9Cr 1Mo ferritic martensitic steel,” *Materials Science and Engineering: A*, vol. 554, pp. 95–104, sep 2012.
- [56] B. Choudhary, K. Bhanu Sankara Rao, S. Mannan, and B. Kashyap, “Influence of prior thermal ageing on tensile deformation and fracture behaviour of forged thick section 9Cr 1Mo ferritic steel,” *Journal of Nuclear Materials*, vol. 273, pp. 315–325, aug 1999.
- [57] Y. Kumar, S. Venugopal, G. Sasikala, S. K. Albert, and A. Bhaduri, “Study of creep crack growth in a modified 9Cr 1Mo steel weld metal and heat affected zone,” *Materials Science and Engineering: A*, vol. 655, pp. 300–309, feb 2016.
- [58] S. Venugopal, G. Sasikala, and Y. Kumar, “Creep Crack Growth Behavior of a P91 Steel Weld,” *Procedia Engineering*, vol. 86, pp. 662–668, jan 2014.
- [59] J. Tong, S. Dalby, J. Byrne, M. B. Henderson, and M. C. Hardy, “Creep, fatigue and oxidation in crack growth in advanced nickel base superalloys,” *International Journal of Fatigue*, vol. 23, no. 10, pp. 897–902, 2001.
- [60] A. Pineau and S. D. Antolovich, “High temperature fatigue of nickel-base superalloys - A review with special emphasis on deformation modes and oxidation,” *Engineering Failure Analysis*, vol. 16, pp. 2668–2697, dec 2009.
- [61] M. C. Hardy, B. Zirbel, G. Shen, and R. Shankar, “Developing damage tolerance and creep resistance in a high strength nickel alloy for disc applications,” *Proceedings of the International Symposium on Superalloys*, pp. 83–90, 2004.

- 
- [62] S. Biroasca, F. Di Gioacchino, S. Stekovic, and M. Hardy, “A quantitative approach to study the effect of local texture and heterogeneous plastic strain on the deformation micromechanism in RR1000 nickel-based superalloy,” *Acta Materialia*, vol. 74, pp. 110–124, aug 2014.
- [63] L. Jacobsson, C. Persson, and S. Melin, “Thermo-mechanical fatigue crack propagation experiments in Inconel 718,” *International Journal of Fatigue*, vol. 31, pp. 1318–1326, aug 2009.
- [64] L. G. Zhao, J. Tong, and M. C. Hardy, “Prediction of crack growth in a nickel based superalloy under fatigue oxidation conditions,” *Engineering Fracture Mechanics*, vol. 77, pp. 925–938, apr 2010.
- [65] A. D. Boyd-Lee, “Fatigue crack growth resistant microstructures in polycrystalline Ni base superalloys for aeroengines,” *International Journal of Fatigue*, vol. 21, no. 4, pp. 393–405, 1999.
- [66] L. Fournier, D. Delafosse, and T. Magnin, “Oxidation induced intergranular cracking and Portevin - Le Chatelier effect in nickel base superalloy 718,” *Materials Science and Engineering: A*, vol. 316, pp. 166–173, nov 2001.
- [67] M. J. Starink and P. A. S. Reed, “Thermal activation of fatigue crack growth: Analysing the mechanisms of fatigue crack propagation in superalloys,” *Materials Science and Engineering A*, vol. 491, pp. 279–289, sep 2008.
- [68] R. Molins, G. Hochstetter, J. Chassaingne, and E. Andrieu, “Oxidation effects on the fatigue crack growth behaviour of alloy 718 at high temperature,” *Acta Materialia*, vol. 45, pp. 663–674, feb 1997.
- [69] H. Kitaguchi, M. Moody, H. Li, H. Evans, M. Hardy, and S. Lozano-Perez, “An atom probe tomography study of the oxide - metal interface of an oxide intrusion ahead of a crack in a polycrystalline Ni - based superalloy,” *Scripta Materialia*, nov 2014.

- 
- [70] C. Stocker, M. Zimmermann, H. J. Christ, Z. L. Zhan, C. Cornet, L. G. Zhao, M. C. Hardy, and J. Tong, “Microstructural characterisation and constitutive behaviour of alloy RR1000 under fatigue and creep-fatigue loading conditions,” *Materials Science and Engineering A*, vol. 518, pp. 27–34, aug 2009.
- [71] Y. Si, J. Rouse, and C. Hyde, “Potential difference methods for measuring crack growth: A review,” *International Journal of Fatigue*, vol. 136, 2020.
- [72] Y. MURAKAMI and K. MILLER, “What is fatigue damage? A view point from the observation of low cycle fatigue process,” *International Journal of Fatigue*, vol. 27, pp. 991–1005, aug 2005.
- [73] G. Sposito, *Advances in Potential Drop Techniques for Non-destructive Testing*. PhD thesis, Imperial College London, 2009.
- [74] J. Worman, “Magnetic Particle Examination,” *National Board of Boiler and Pressure Vessel Inspectors - BULLETIN*, 2011.
- [75] V. Deutsch, “History of NDT  $\hat{A}$  Instrumentation,” 2015.
- [76] Z. Chen, K. Miya, and M. Kurokawa, “Rapid prediction of eddy current testing signals using A  $\phi$  method and database,” *NDT & E International*, vol. 32, pp. 29–36, jan 1999.
- [77] Z. Chen, N. Yusa, and K. Miya, “Enhancements of eddy current testing techniques for quantitative nondestructive testing of key structural components of nuclear power plants,” *Nuclear Engineering and Design*, vol. 238, pp. 1651–1656, jul 2008.
- [78] L. Doremus, Y. Nadot, G. Henaff, C. Mary, and S. Pierret, “Calibration of the potential drop method for monitoring small crack growth from surface anomalies - Crack front marking technique and finite element simulations,” *International Journal of Fatigue*, vol. 70, pp. 178–185, sep 2014.

- 
- [79] R. Branco, F. Antunes, J. Costa, F. P. Yang, and Z. B. Kuang, “Determination of the Paris law constants in round bars from beach marks on fracture surfaces,” *Engineering Fracture Mechanics*, vol. 96, pp. 96–106, dec 2012.
- [80] J. Yue, Y. Dong, and C. Guedes Soares, “An experimental-finite element method based on beach marks to determine fatigue crack growth rate in thick plates with varying stress states,” *Engineering Fracture Mechanics*, vol. 196, pp. 123–141, 2018.
- [81] S. Raman and Y. Kitsunai, “Influence of beach mark loading and pre-crack length on fatigue crack growth rate of A533B steel in high temperature water,” *Journal of Materials Science Letters*, vol. 19, pp. 1057–1059, 2000.
- [82] J. Spachtholz, E. E. Affeldt, H. J. Maier, and J. Hammer, “Modelling of the fatigue crack growth of a coated single crystalline nickel-based superalloy under thermal mechanical loading,” *International Journal of Fatigue*, vol. 116, no. June, pp. 268–274, 2018.
- [83] Matelect, “The Potential Drop Technique & Its Use In Fatigue Testing.”
- [84] M. Akama and M. Saka, “Nondestructive sizing of a 3D surface crack generated in a railway component using closely coupled probes for direct-current potential drop technique,” *Engineering Fracture Mechanics*, vol. 72, pp. 319–334, jan 2005.
- [85] G. Sposito, P. Cawley, and P. B. Nagy, “An approximate model for three-dimensional alternating current potential drop analyses using a commercial finite element code,” *NDT and E International*, vol. 43, pp. 134–140, mar 2010.
- [86] Y. Hashimoto, Y. Urabe, S. Masamori, Y. Kamiwaki, and K. Baba, “Procedure of crack shape determination by reversing DC potential method,” *Nuclear Engineering and Design*, vol. 138, pp. 259–268, dec 1992.

- 
- [87] V. Spitas, C. Spitas, and P. Michelis, “A three-point electrical potential difference method for in situ monitoring of propagating mixed-mode cracks at high temperature,” *Measurement*, vol. 43, pp. 950–959, aug 2010.
- [88] T. Buss, J. Rouse, C. Hyde, and S. Garvey, “Development of a technique for the real-time determination of crack geometries in laboratory samples,” in *MATEC Web of Conferences*, vol. 165, 2018.
- [89] W. Dover, F. Charlesworth, K. Taylor, R. Collins, and D. Michael, “The Use of A-C Field Measurements to Determine the Shape and Size of a Crack in a Metal,” *Eddy-Current Characterization of Materials and Structures*, pp. 401–401–27, 1981.
- [90] M. K. Raja, S. Mahadevan, B. P. C. Rao, S. P. Behera, T. Jayakumar, and B. Raj, “Influence of crack length on crack depth measurement by an alternating current potential drop technique,” *Measurement Science and Technology*, vol. 21, no. 10, p. 105702, 2010.
- [91] H. Saguy and D. Rittel, “Bridging thin and thick skin solutions for alternating currents in cracked conductors,” *Applied Physics Letters*, vol. 87, no. 8, pp. 68–70, 2005.
- [92] H. Saguy and D. Rittel, “Flaw detection in metals by the ACPD technique: Theory and experiments,” *NDT & E International*, vol. 40, pp. 505–509, oct 2007.
- [93] H. Saguy and D. Rittel, “Alternating current flow in internally flawed conductors: A tomographic analysis,” *Applied Physics Letters*, vol. 89, no. 9, pp. 214–216, 2006.
- [94] ASTM, “ASTM E2368-10 Standard Practice for Strain Controlled Thermomechanical Fatigue Testing,” 2017.
- [95] BSI, “BSI Standards Publication Metallic materials - Fatigue testing - Strain-controlled thermomechanical fatigue testing method,” 2011.

- 
- [96] D. Gille, B. Ward, D. Hogan, and S. Wrobel, “Materials and Mechanical Methods TEST METHOD FOR THE DETERMINATION OF THE RATE OF FATIGUE CRACK GROWTH IN METALLIC MATERIALS - CORNER CRACK GEOMETRY,” 2010.
- [97] Z. J. Lu, P. J. Nicholas, and W. J. Evans, “Calibration of an ACPD Monitoring System for Small Crack Growth in Corner Crack Specimens,” *Engineering Fracture Mechanics*, vol. 50, no. 4, pp. 443–456, 1995.
- [98] M. S. Loveday, M. F. Day, and B. F. Dyson, *Measurement of High Temperature Mechanical Properties of Materials*. 1982.
- [99] S. Tiku, N. Marchand, and B. Unvala, “An Advanced Multiple Frequency ACPD System for Crack Detection and Calibration,” in *Non-traditional Methods of Sensing Stress, Strain, and Damage in Materials and Structures*, pp. 56–67, ASTM, 1997.
- [100] Y. Murakami, *Stress Intensity Factors Handbook*. Pergamon, 1986.
- [101] D. Roylance, “Fatigue,” 2001.
- [102] S. P. Lynch, “Progression markings, striations, and crack-arrest markings on fracture surfaces,” *Materials Science and Engineering A*, vol. 468-470, pp. 74–80, nov 2007.
- [103] R. Sharma and M. Srinivas, “Failure analysis of left barrel of an aircraft engine,” *Engineering Failure Analysis*, vol. 16, pp. 1468–1473, jul 2009.
- [104] C. J. Hyde, T. Buss, and J. P. Rouse, “Isothermal and an-isothermal fatigue crack growth in a 316 stainless steel .,”
- [105] V. K. Sikka, B. L. P. Booker, M. K. Booker, and J. W. McEnerney, “Tensile and Creep Data on Type 316 Stainless Steel,” tech. rep., OAK Ridge National Laboratory, 1980.
- [106] M. N. Babu, B. S. Dutt, S. Venugopal, G. Sasikala, S. K. Albert, A. Bhaduri, and T. Jayakumar, “Fatigue Crack Growth Behavior of

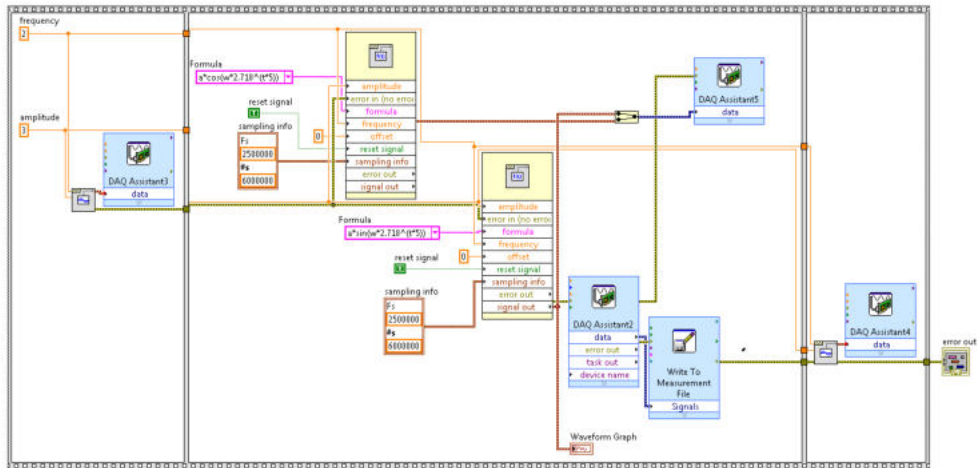
- 
- 316LN Stainless Steel with Different Nitrogen Contents,” *Procedia Engineering*, vol. 55, pp. 716–721, jan 2013.
- [107] Aalco, “Stainless Steels - Stainless 316 Properties , Fabrication and Applications , Supplier Data by Aalco,” 2005.
- [108] AKSteel, “Stainless Steel 316/316L Product Data Bulletin,” 2013.

## APPENDIX

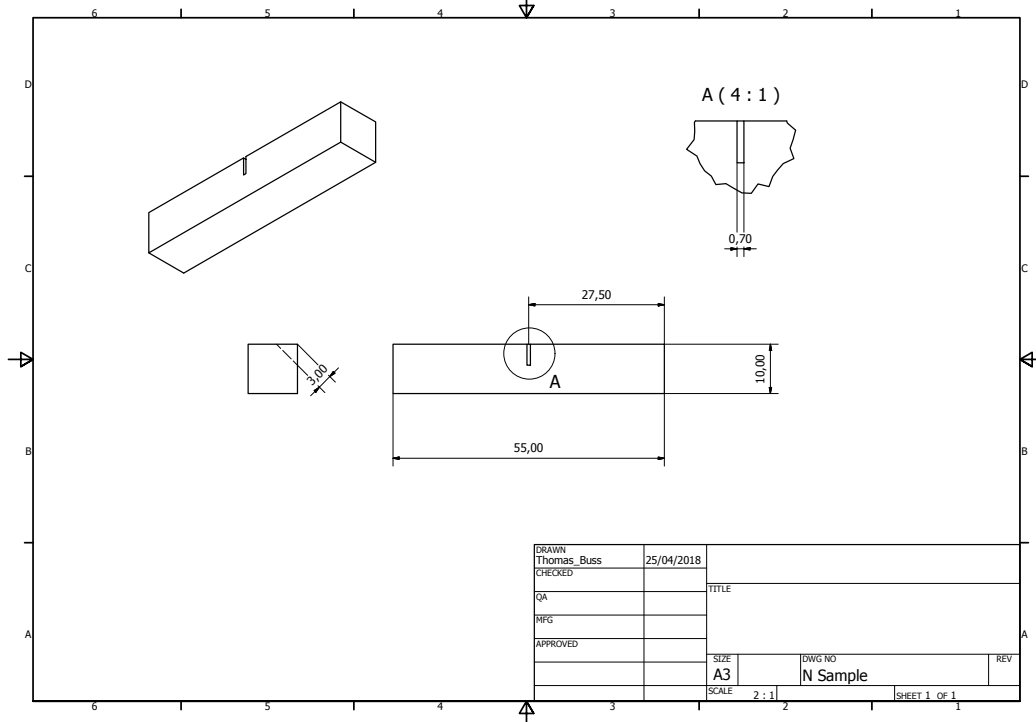
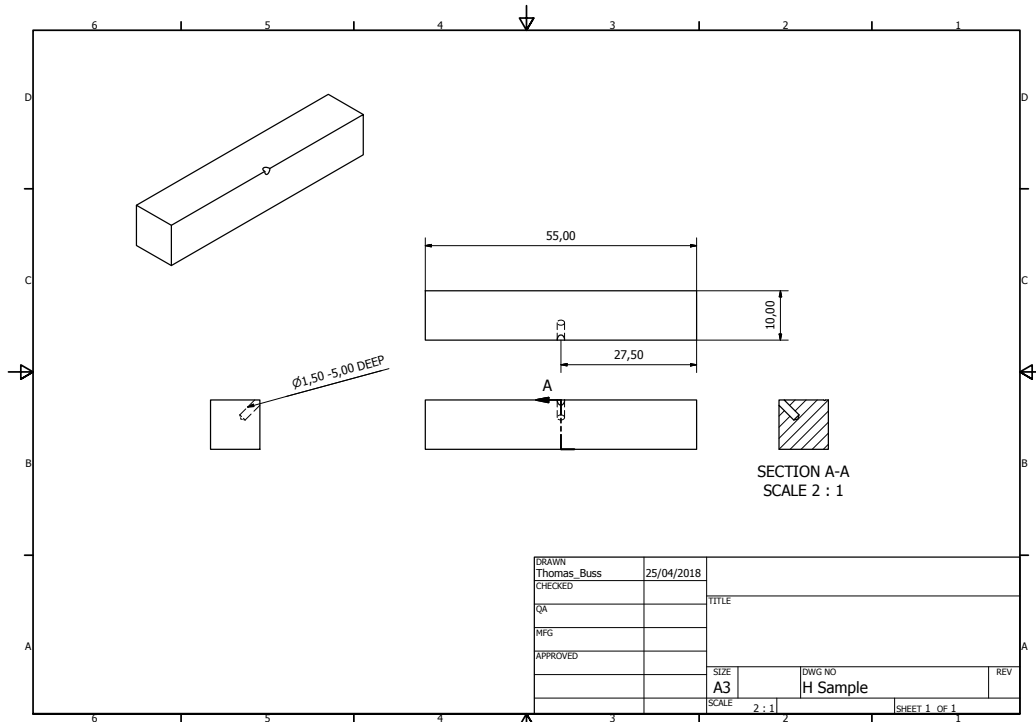


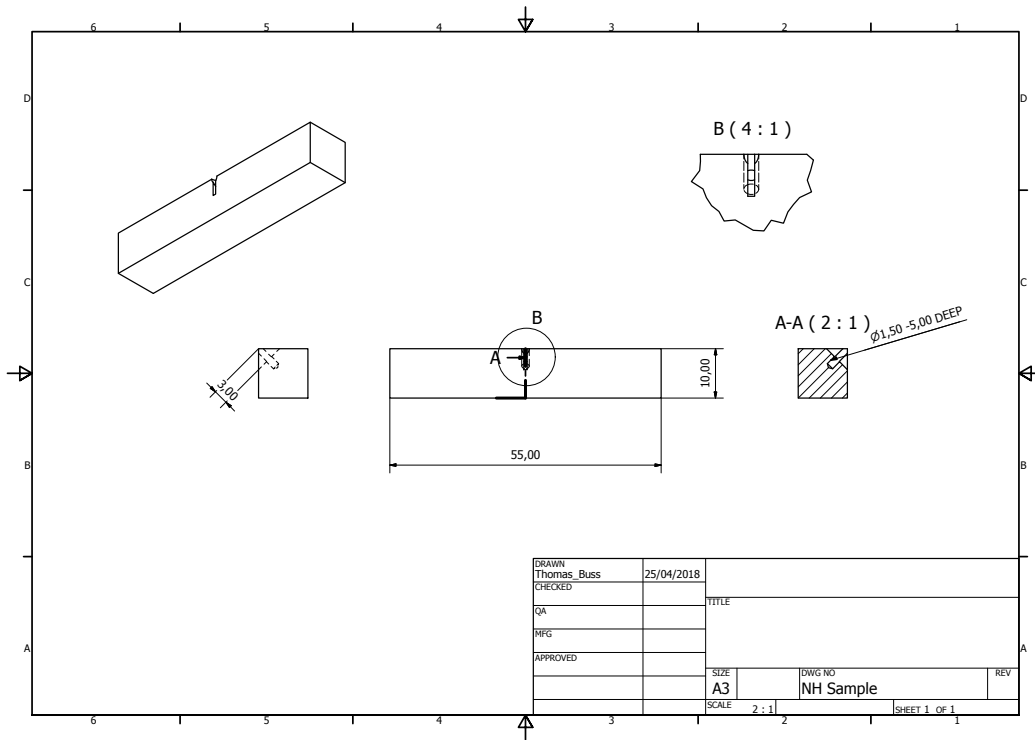
## A.2 PXI Sweep Labview Code

Labview code to generate a swept sine signal, the desired current frequency sweep. Acquisition is triggered on a rising voltage edge, 8M samples (2 seconds) of data on all channel is recorded



A.3 Bench Samples





## A.4 Crack Growth Rate Code

01/09/17 09:23 C:\Users\Thomas Buss...\CGR\_deltaK\_0\_6lim.m 1 of 3

```
function [ logdeltaK, logda_dN ] = CGR( a, F, r )
%Calculate DeltaK
%INPUT DATA SHOULD BE
%a = crack length in mm
%F = max force in N
%r = r-ratio

%OUTPUT DATA IS
%K in Pa(sqrt)m
%da/dN m/cycle

%NEEDS THESE 2 FUNCTIONS IN THE SAME FOLDER TO RUN
%optimise.m
%exp_function.m

%Set values that are constants
Ek = 1.5697;
f0 = 1;
M1 = 1.0500;
M2 = 0.3754;
M3 = -0.25;
Q = 45;
t = 0.007;
b = a./1000;

%Discard Data where a/w is greater than 0.6

B = b < 0.0042;
b = b(B);

%calc g1
g1 = 1+(0.08+0.4 .* (b ./ t).^2) .* (1-sind(Q));

%calc g2
g2 = 1 + (0.08+0.15 .* (b ./ t).^2) .* (1-cosd(Q));

%calc Fc
Fc = (M1 + M2.*(b./t).^2 + M3.*(b./t).^4) .*g1 .*g2 .*f0;

%calc Max stress
sigma_max = F./((t*t)-(pi.*b.^2)/4);

%calc Min stress
sigma_min = (F.*r)./((t*t)-(pi.*b.^2)/4);

%calc K
Kmax = (sigma_max.*(sqrt(pi.*b))./Ek).*Fc;
Kmin = (sigma_min.*(sqrt(pi.*b))./Ek).*Fc;

%calc deltaK
deltaK = Kmax - Kmin;
```

## A.5 Fracture Mechanics Beach Mark Code

```

clear

%%% INPUTS %%%
%BEACH
n = 3.7258;
C = 2.33884E-14;
R = 0.7;

%TEST
%n = 4.9107;
%C = 2.11836E-18;
%R = 0;

W = 7;
Pmax = 24.5;

startcrack = 3.26;
crackgrowth = 0.025;

%%% CALCULATION OF NUMBER OF CYCLES TO GROW CRACK TO DESIRED LENGTH %%%

crack = startcrack;

x = 1;
a(x) = crack;

Smax = (Pmax*1000)/(W^2); % Max stress in MPa

M1 = 1.08-0.03*1; % M1, M2, M3, f_phi, g1, g2, Fc & Ek are Frac mech
constants/variables
M2 = -0.44+(1.06/(0.3+1));
M3 = -0.5+0.25*1+14.8*((1-1)^15);
f_phi = ((1*((cos(pi()/4))^2))+((sin(pi()/4))^2))^0.25;
Ek = (1+1.464*(1^1.65))^0.5;
while crack <= startcrack + crackgrowth
    g1(x) = 1+((0.08+(0.4*((a(x)/W)^2)))*(1-(sin(pi()/4)))^3);
    g2(x) = 1+((0.08+(0.15*((a(x)/W)^2)))*(1-(cos(pi()/4)))^3);
    Fc(x) = (M1+(M2*((a(x)/W)^2)))+(M3*((a(x)/W)^4))*g1(x)*g2(x)*f_phi;
    Kmax(x) = (Smax*sqrt(pi()*a(x))*Fc(x))/Ek;
    Kmin(x) = Kmax(x)*R;
    dK(x) = Kmax(x)-Kmin(x);
    logdK(x) = log10(dK(x));
    logdadN(x) = n*logdK(x)+log10(C);
    dadN(x) = 10^logdadN(x); % this is da for dN = 1
    x = x + 1;
    crack = crack + dadN(x-1);
    a(x) = crack;
end

cycles = x - 1

```